Rotational excitation of methanol by helium at interstellar temperatures

Pottage, James

Rotational excitation of methanol by helium at interstellar temperatures

by

James Pottage

A Thesis submitted in partial fulfilment
of the requirements for the degree of
Doctor of Philosophy

Department of Physics

The University of Durham

2002

Abstract

Calculations have been performed to obtain accurate cross-sections and thermally averaged rate coefficients for the rotational excitation of methanol by helium, using the Coupled States quantum-mechanical approach. Transitions within the ground and first torsionally excited states of A and E- type methanol were considered. The 'propensity rules' governing the collisional transitions were examined and compared with the results of microwave double resonance experiments. Predictions are made of line intensity ratios which are sensitive to the density of the He perturber and which lend themselves to the determination of the perturber densities in astrophysically interesting regions of molecular clouds.

Contents

Chapter 1

Introduction

1.1 Astrophysical motivation

Methanol is important in answering questions concerning all stages of stellar formation, from cold, dense cores within dark clouds, to hotter HII regions ionised by embedded protostellar objects. Methanol emissions occur from diverse sources, such as 'maser spots' in hotter clouds, in bipolar outflows, and in the region of accretion shock within protostellar disks. In this way, methanol is said to 'trace' certain important structures.

An example of the use of methanol as an important 'tracer' for structures is Velusamy, Langer and Goldsmith 2002 [2]. In this study the presence of accretion shocks (previously unestablished) is confirmed from the spatially resolved methanol emission associated with the 5_0-$4_0(A)$ transition within a protostellar object. Theoretical models of the formation of protostellar disks predict that infalling material feeds the growth of the disk, infalling mass being transferred to the developing star. The spatial distribution and the inferred kinematics of the methanol emission in the protostellar object trace a heated layer in the interface between the infalling material and the accretion disk, this being consistent with the prediction of an accretion shock, which is a feature of the numerical models of this system. The warm layer associated with the accretion shock is believed to be responsible for enhanced emission by various molecular 'tracers', including CH_3OH. Figure 1.1 shows

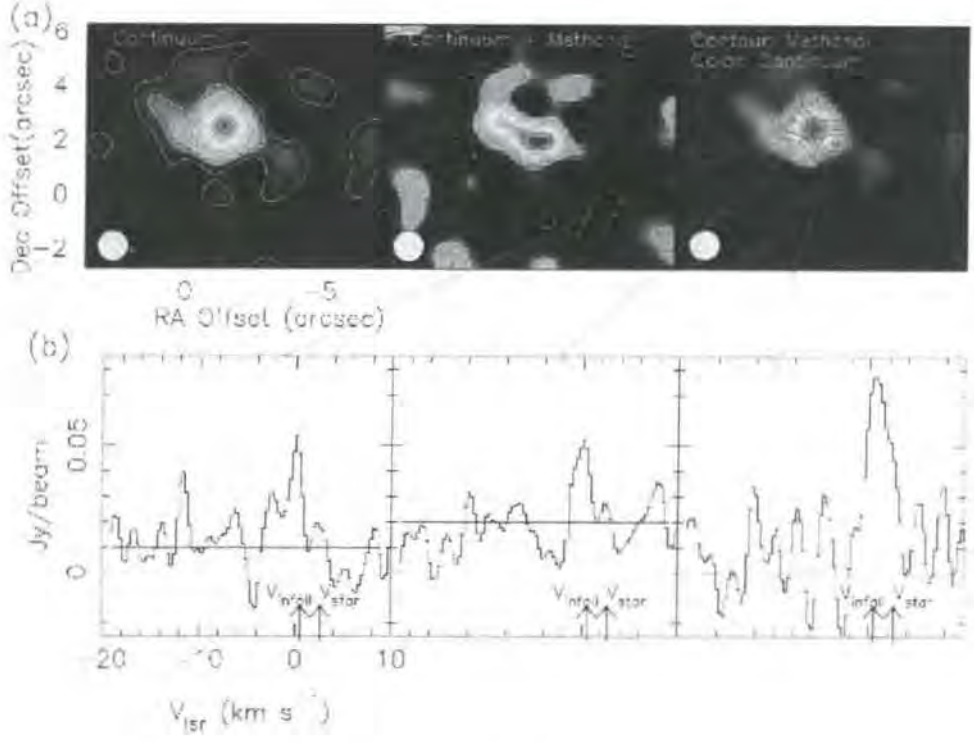

Figure 1.1: Top: maps of dust continuum and methanol spectral line emission. at 1mm wavelength, from the disk in L1157. *(a). Left*: dust continuum. *Middle*: continuum and methanol emission. *Right*: methanol contours with dust continuum overlaid. *(b).* The lower panel gives the methanol spectra of the points indicated in the top right panel. Source: [2]

the methanol emission in protostellar disk L1157, clearly delineating an extended outflow layer in the disk in a plane perpendicular to the outflow, and thus tracing a layer interfacing the disk and infall envelope.

Maser emissions from various common molecular species have been found to be immensely useful in tracing regions of star formation. A recent paper (Walmsley et al 2002 [3]) points out that, towards such regions, the most intense and widely observed maser emissions are those of the molecules OH at 1.6 and 6.0 GHz, H_2O at 22 GHz, and CH_3OH at 6.7 and 12 GHz. It is a general rule that the maser emission from these molecules originates from hundreds of distinct, compact emission centres ('maser spots'.) Very Long Baseline Interferometry (VLBI), in combination with Doppler line-of-sight velocity measurements, allows the proper motions of these

maser spots to be determined and then assembled into a complete three-dimensional map of the velocities of the maser spots, and hence the motion of the gas in the vicinity of protostellar objects. These studies are capable of mapping such gas motion in great detail, on a length scale of 1-10 AU. Figure 1.2 shows the movement of maser spots between two observations of the ultracompact HII region known as W3(OH) with a Very Large Baseline Array.

OH and CH_3OH 'maser spots', because they are spatially localized, and their emission depends on the densities and temperatures of the spot they occupy, serve as probes of the small-scale structure (1 AU-scale), dynamics and physical conditions of star-forming regions. In the paper mentioned above (Walmsley et al 2002 [3]), it is exclusively methanol maser emission which is used to trace the kinematics of an ultracompact HII region known as 'W3(OH)'. In addition to methanol 'maser spots', methanol is associated with other interesting features of star-forming regions. For instance, Rodriguez et al 2002 [4] describe the presence of methanol and SiO in bipolar outflows from Class 0 objects– that is, highly collimated outflows observed emanating from young stellar objects. Figure 1.3 gives, in the lower panel, contour maps of CH_3OH $3_0 - 2_0 A$ emission from the Class 0 object IRAS 16293-2422. Blue-shifted and red-shifted emission trace the rotation of the object. An example of an intensity vs. velocity graph from which such diagrams can be assembled is given in Figure 1.4, for a different object and transition. In this image, a methanol 'flare' is shown- i.e a sudden change in the velocity distribution of the emission.

Such features as disks and bipolar outflows are important, since the current paradigm for star formation is that stars form by an accretion process which involves a circumstellar disk of material and a bipolar outflow perpendicular to this disk, which is collimated by the inward motion of the accreting material. Consensus has, at least, been reached on this point for the case of low-mass and solar-mass stars. However, the mechanism for the formation of high-mass stars is still disputed, the two main camps advocating circumstellar disks on the one hand, giving the same mechanism of formation for stars of all masses, and, on the other hand, mergers of low-mass stars to produce massive stars. As regards the settling of

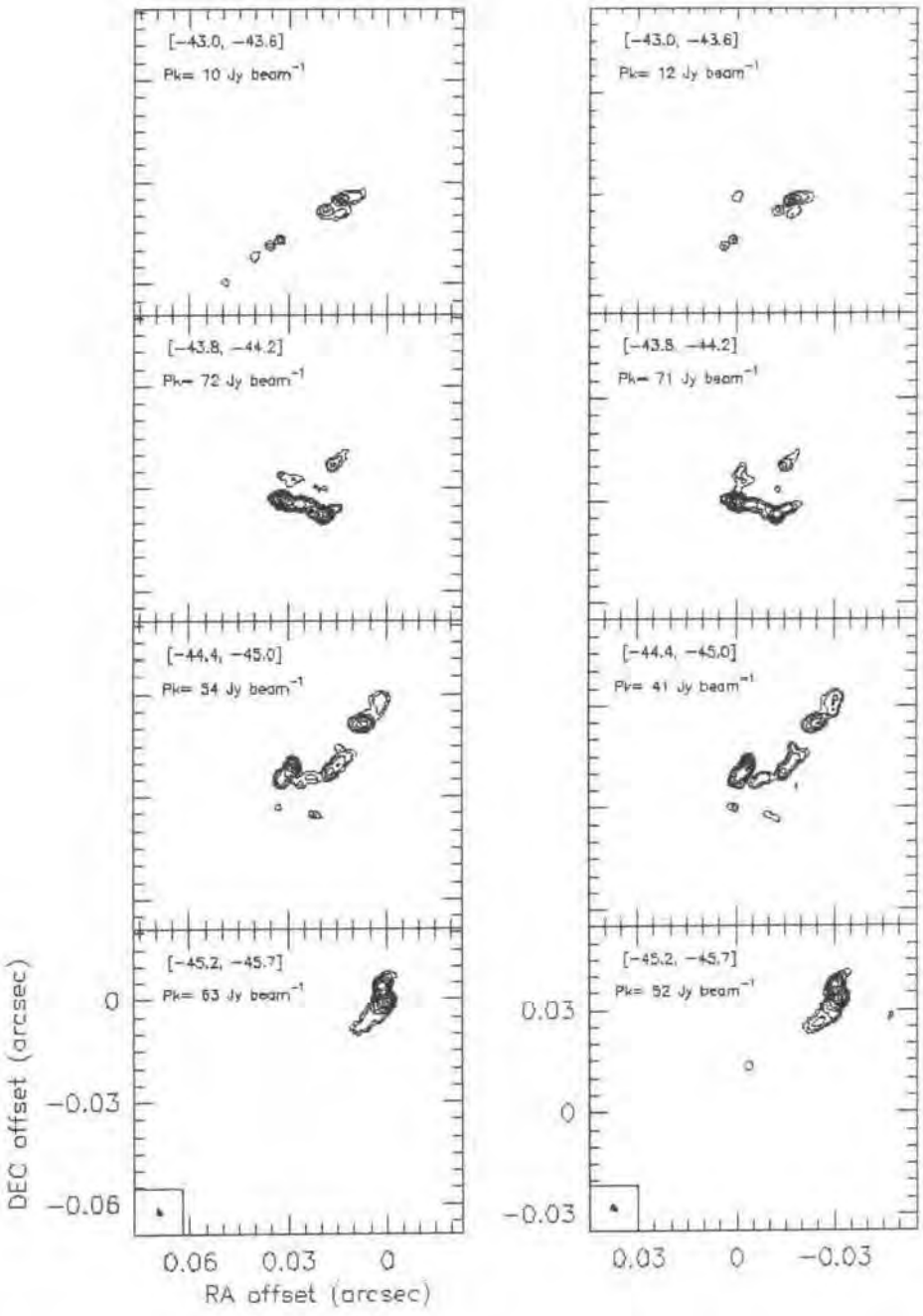

Figure 1.2: Comparison of the structure of the maser emission in the northern clump of the ultracompact HII region W3(OH) between two successive VLBA epochs, February 1994 (four panels on left) and December 1998 (four panels on right). In each panel, the emission has been averaged over the velocity interval (in units of kilometres per second) given on the upper left-hand corner, together with the peak intensity (in Janskys) of the velocity-averaged map. Source: [3]

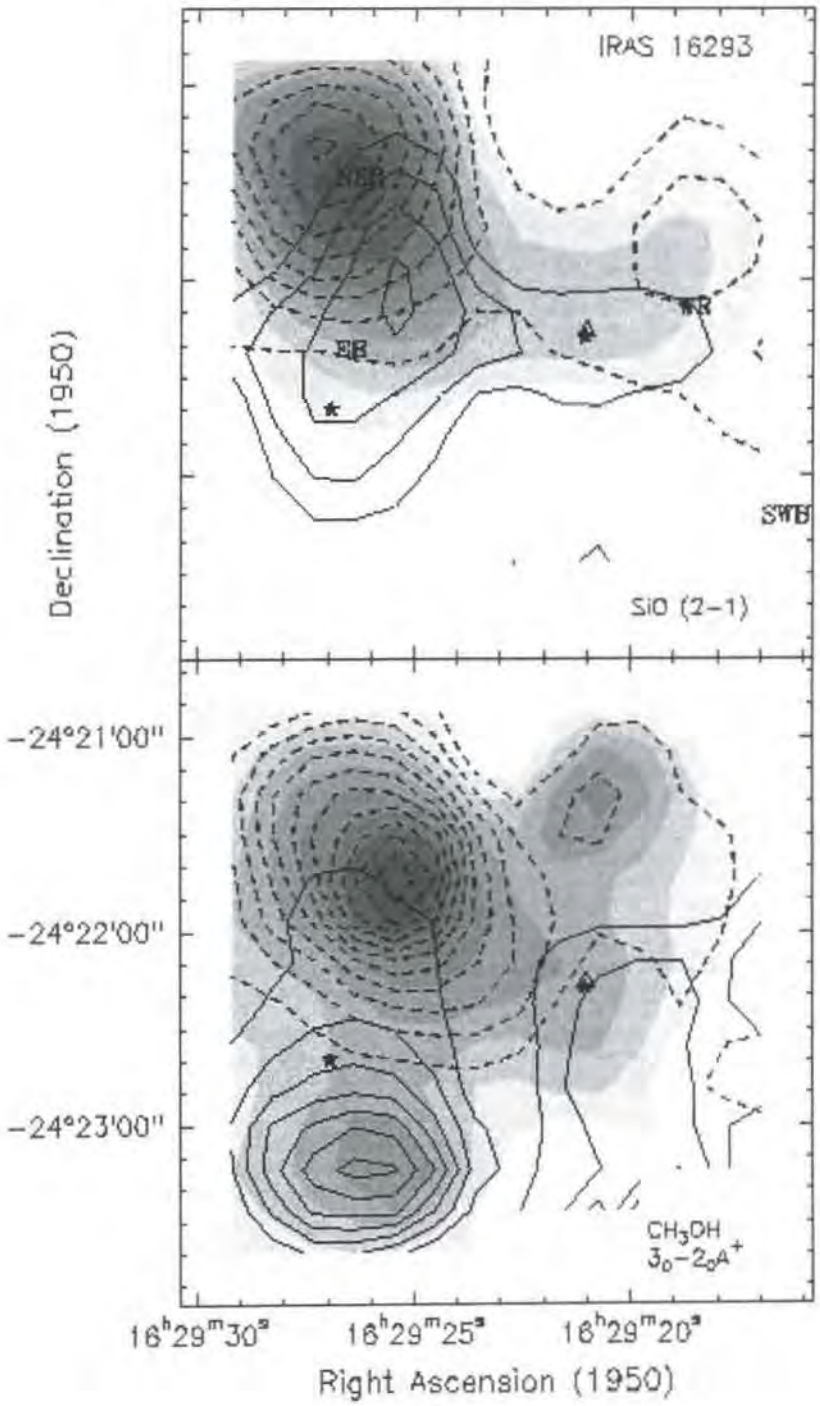

Figure 1.3: Contour map of velocity-integrated line wing emission from the IRAS 12693-2422 outflow. Continuous and dashed lines represent blueshifted and redshifted emission, respectively. Gray-scale indicates velocity-integrated methanol emission from ambient gas only. The lower panel refers to the $3_0 - 2_0A$ line of methanol. Lowest contour and contour interval are 0.2 K km s^{-1} for the blueshifted emission (v_{flow}:-5.1 to -1.3 km s^{-1}) and 0.4 K km s^{-1} for the redshifted emission (v_{flow}:1.3 to 6.3 km s^{-1}.) The top panel refers to SiO emissions. Source: [4]

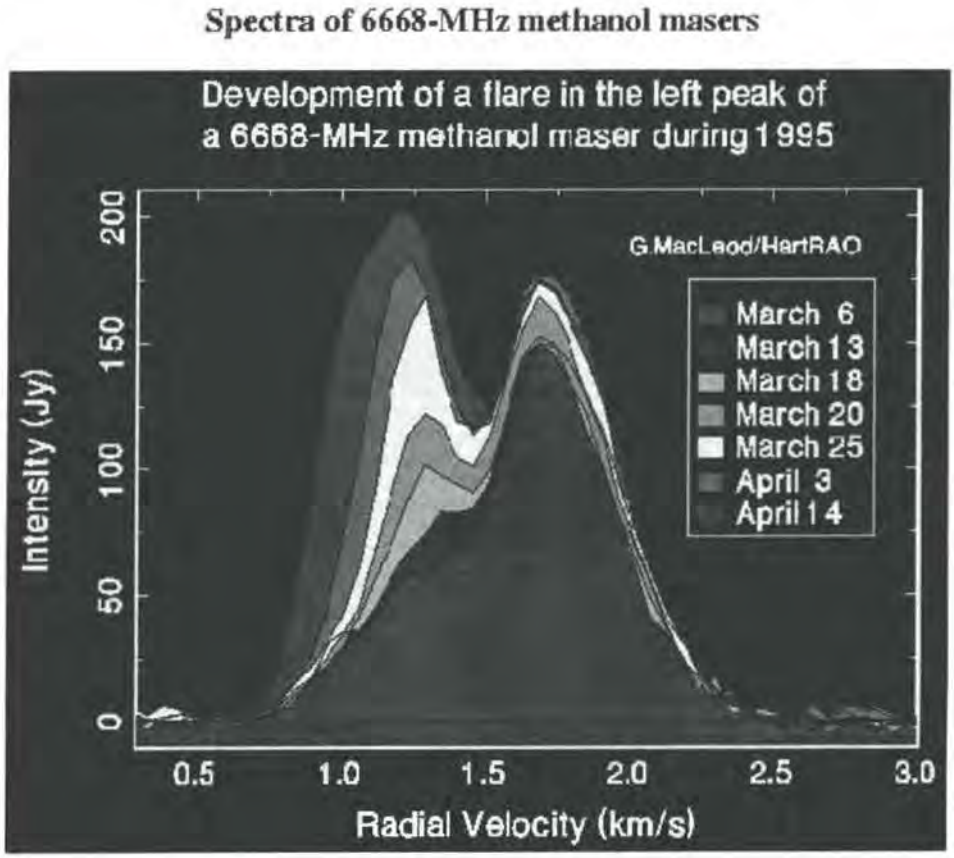

Figure 1.4: Methanol flare spectrum. Source: given in figure. The emission from the methanol masers in the molecular cloud around this star-forming region shows a double-peaked profile. The peak seen above on the left has been found to vary rapidly, undergoing flares every few months. The growth of the peak during one such flare is shown. The flares may be caused by blobs of gas ionized by the central star shooting behind the masing region, although they could also be caused by disturbances travelling through the masing region itself.

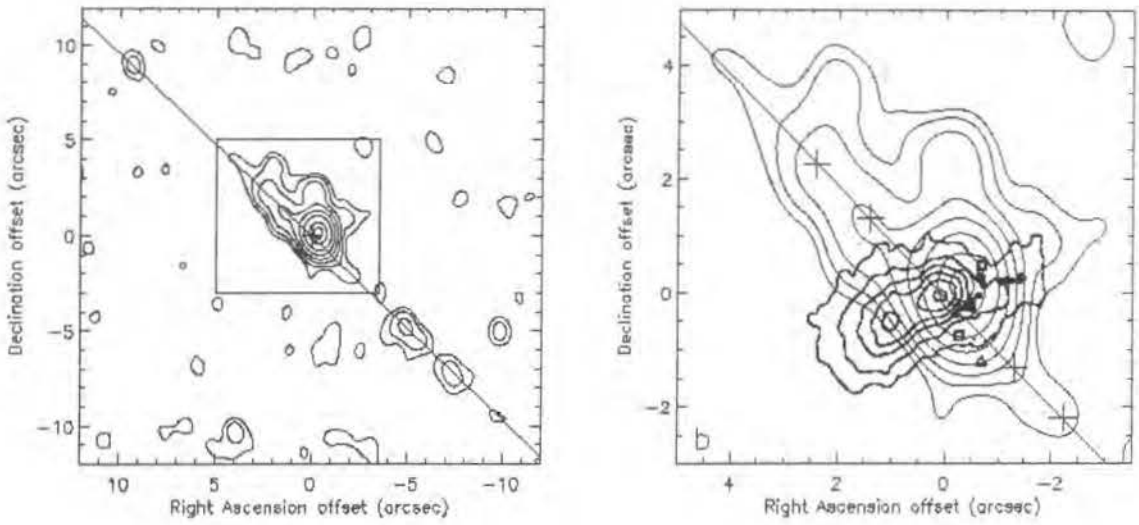

Figure 1.5: *(a)* is a wide-field contour map of the 8.59 GHz radio continuum from G339.88-1.26, the peak of which is elongated, with other knots of radio emission lying along the elongation axis (diagonal line). *(b)* Close-up of the peak radio emission area with mid-infrared contours overlaid. Filled circles indicate the positions of methanol masers. Triangles and squares mark water and OH masers. Source: [5]

this question, the only circumstantial evidence for circumstellar disks in high mass stars exists in the form of radio emission from outflows and masers. Radio observations (see the summary in Pina et al 2002 [5]) have shown that CH_3OH maser spots are frequently distributed in linear patterns, typically spanning distances of 2500 AU. Also, typically, the velocities of the individual maser spots in these lines vary linearly across the source region. This is indicative of the maser spots delineating a structure in uniform circular motion. It has thus been plausibly argued that methanol maser spots occur in, and directly delineate, circumstellar disks. However, other authors suggest that both the linear pattern of the maser spot distribution and the velocities of the spots, may be explained by shock models involving mergers of low-mass stars. Figure 1.5 shows radio continuum emission from an object known as G339.88-1.26, thought to be a good candidate for a massive star with a circumstellar disk. This is supported by the observation of linearly distributed methanol maser spots believed to delineate this disk.

The richness of the spectra of methanol observed in the interstellar medium suggests the possibility of using the relative intensities of appropriate transitions as diagnostics of the physical conditions of the gas, by considering transitions whose relative intensities are sensitive to the density and temperature of the medium. The following work concentrates mainly on collisional processes in cold, dense cores, since the required calculations become increasingly large as the kinetic temperature of the gas is increased. Such astrophysical applications of our work are discussed in Chapter 6. Theoretical intensity ratios of pairs of methanol lines at low temperatures would allow observational data from cold, dark nebulae to be used for the determination of the physical conditions in these regions.

1.2 Structure of methanol

A peculiarity of methanol is that the methyl group in methanol can rotate independently of the -OH group, giving an extra degree of freedom, and this so-called internal rotation complicates the situation. As regards the study of this general phenomenon, methanol is one of the simplest molecules exhibiting internal rotation, which is also known as torsional motion. In the case of methanol, the rotation is that of the methyl radical relative to the -OH group. The internal rotation is hindered by a potential barrier of height $V_3 = 373$ cm^{-1}. The potential may be written, to first order, as

$$V(\gamma) = \frac{V_3}{2}(1 - \cos 3\gamma), \tag{1.1}$$

where γ is the angle of internal rotation about the symmetry axis of the molecule. The interaction (1.1) has three-fold symmetry about this axis owing to the identity of the hydrogen atoms in the CH_3 radical.

Methanol occurs as A- and E-type, which correspond to nuclear spin states $I = 3/2$ and $I = 1/2$, respectively. The difference in nuclear spin states gives rise to two distinct types of torsional motion. The theory underlying the spectroscopy and structure of the two types of methanol has been given by Townes and Schawlow

(1955) [6], Lin and Swalen (1959) [7] and Lees and Baker (1968) [8]. Lin and Swalen gave explicit expressions for the matrix elements of the internal hamiltonian of A- and E-type methanol. Diagonalization of this hamiltonian yields the energy levels, and the corresponding eigenfunctions, required in the scattering calculations. The structural aspects of methanol, including torsion, are considered in detail in Chapter 2.

1.3 Collisions of CH_3OH with He and H_2

As we have seen, some transitions of methanol are observed as masers, owing to population inversion, in regions of star formation in the interstellar medium (Rodriguez-Fernandez et al 1999 [9]), whilst the 12.18 GHz transition of E-type methanol is observed in absorption against the 2.73 K cosmic background radiation in dark interstellar clouds (Matthews et al 1988 [10]), owing to an excess of population in the lower level of this transition. In order to understand these and other observations of methanol, rate coefficients are required for collisional transfer amongst the rotational levels of methanol induced in collisions with the most abundant perturbers, H_2 and He. In cold, dense clouds, collisions are the dominant process which accounts for observed emissions.

Work on the problem of CH_3OH-He collisions has been done before, but it has been primarily empirical. For instance, Lees and Haque (1974) [1] performed microwave double resonance measurements on CH_3OH (E-type torsional state) in He and in H_2 and deduced propensity rules for the corresponding collisional processes. They concluded that their experimental results were qualitatively consistent with the dipolar selection rules $\Delta J = 0, 1$ and $\Delta K = 0, 1$, where J is the rotational angular momentum and K is its projection on the symmetry axis of the CH_3OH molecule. Their results formed a basis for the subsequent study of the 12.18 GHz transition of E-type methanol (Matthews et al. 1988 [10]), which was observed in absorption towards two Galactic molecular clouds. The excitation temperature of this transition was less than that (2.73 K) of the cosmic background radiation. This behaviour, observed with certain methanol transitions, is referred to as *anti-*

inversion, and can be thought of as the opposite of masing action, in that instead of population inversion occurring, the lower level of the transition becomes more populated than the higher level. Such transitions may be observed in absorption against the cosmic microwave background radiation if the degree of anti-inversion is sufficient.

It was the empirical rate coefficients of Lees and Haque which enabled Walmsley to model this interesting anti-inversion effect, thereby going some way towards understanding it. The stage was set for the calculation of theoretical rate coefficients for this system by Davis and Entley (1992) [11], who performed calculations of the CH_3OH-He interaction potential and gave expressions for its long range form in terms of multipole moments and polarizabilities (see also Davis and Dennison 1994 [12]). Davis and Entley (1992) [11] calculated cross sections for the excitation of the overall and the internal rotation of CH_3OH in collisions with He, but at only one collision energy (500 cm^{-1}) and in the infinite order sudden (IOS) approximation.

Recently, Davis has produced a sophisticated interaction potential using second-order Many-Body Perturbation Theory. The natural development of having an interaction potential available to us is the calculation of collision cross-sections. The aim of this work is to calculate accurate cross-sections for the rotational excitation of CH_3OH by He at low interstellar temperatures, a system which is, as we have seen, both theoretically and experimentally interesting. The required collision theory is dealt with in Chapter 3, and our method and collisional results are presented in Chapters 4 and 5 respectively. The cross-sections (or, rather, the thermally averaged rate coefficients obtained from them) are used in Chapter 6 to provide a means for experimentalists to infer the physical conditions in cold clouds from observations of methanol line intensities. Without precise knowledge of the conditions within cold clouds, questions concerning many aspects of the early stages of stellar formation will remain unresolved, and this is the problem we address.

Chapter 2

Theory: Molecular Structure

2.1 Synopsis

The following sections will progress from the symmetric top to the asymmetric top, and then, finally, the internal rotation of methanol will be examined using the ideas we have intoduced. That is, our discussion will develop from rigid rotors (where the molecular structure is rigidly fixed, and is therefore not allowed to undergo torsion) to the more complicated case of a non-rigid rotor.

Symmetric tops

First, we will introduce the symmetric top, together with its Hamiltonian and rotational constants. Then the use of rotation matrices to construct symmetric top eigenfunctions will follow. The rotation of a molecule about its symmetry axis is equivalent to a sequence of exchanges of the constituent nuclei; therefore the Pauli principle imposes restrictions on the spin/rotational wavefunctions, and these restrictions are discussed in the context of a symmetric top molecule with a threefold symmetry about its rotation axis, an example of such a top being methanol, which is *nearly* symmetric. Different spin orientations are then related to distinct physical behaviours. Finally, explicit spin/rotational eigenfunctions are given for a three-fold symmetric top.

Asymmetric tops

The two limiting cases of an oblate top and a prolate top are discussed, followed by the introduction of an 'asymmetry parameter', the limiting values of which

correspond to oblate and prolate tops. Next, the general D_2 group of an asymmetric top is presented, and it is then applied in two ways:

(a) Correlating the rotational energy levels of an asymmetric top with good quantum numbers belonging to the prolate and oblate symmetric top regimes. This correlation uses the mixed symmetry types that the asymmetric top wavefunctions have under the D_2 group.

(b) Using the D_2 symmetry of the asymmetric top to construct eigenfunctions which are adapted to this symmetry, in the sense that a Hamiltonian matrix set up with these symmetry-adapted eigenfunctions as a basis will be automatically block-diagonal. Symmetry-adaption is used at the end of the next section, where a convenient basis set is sought for the treatment of a non-rigid asymmetric top. In this case, 'symmetry-adaption' refers to the choice of a basis set to represent the threefold periodicity of the torsional eigenfunctions.

Internal rotation

After presenting the equilibrium structure of the methanol molecule, the phenomenon of torsion is discussed. Torsion in methanol does not occur freely – that is, a certain potential, due to mutual interactions, is experienced by the rotating parts, and this potential varies with angular displacement around the symmetry axis. The form of the torsional potential of methanol is discussed. We then derive the full non-rigid asymmetric top Hamiltonian, and we show how torsion arises naturally from this. This, however, is very complicated. To simplify our expressions, certain transformations are carried out to remove the coupling between internal and overall rotation, and this leads to a set of 'effective rotational constants'. Using a torsionally adapted basis set, we then obtain the Hamiltonian matrix, which can be used to determine the energy levels of a non- rigid asymmetric top. The torsional basis, together with the torsional potential, is then used to form an equation for the energy eigenvalues of torsional motion. The resulting equation is known as the Mathieu equation.

The threefold symmetry of the torsional potential makes C_{3v} the natural symmetry group of the torsional eigenfunctions, this being the group of any threefold symmetric top. The symmetry species of the torsional eigenstates within this

group are then determined. We then make explicit the relation of the torsional symmetry species of methanol to nuclear spin, referring to our earlier discussion of spin-rotational wavefunctions.

2.2 Symmetric tops

A symmetric top is a rotor for which two of the rotational constants A, B and C are equal in the general rotor Hamiltonian:

$$\hat{H}_{rot} = \hbar^{-2}(Ap_a^2 + Bp_b^2 + Cp_c^2) \tag{2.1}$$

where $A = \frac{\hbar^2}{2I_a}$, $B = \frac{\hbar^2}{2I_b}$, and $C = \frac{\hbar^2}{2I_c}$. I_a and p_a are the moment of inertia and angular momentum about the a axis respectively. The axis c is chosen to be the symmetry axis here, and therefore $A = B$.

Writing the wave equation $\hat{H}\Psi = E\Psi$ in terms of the space-fixed (i.e. non-rotating) coordinate system, and solving for Ψ, one obtains solutions $|jkm>$, where j, k and m are required to be integers. These symmetric top eigenfunctions $|jkm>$ can be expressed in terms of rotation matrices:

$$|jkm>= [(2j+1)/8\pi^2]^{\frac{1}{2}} D^j_{km}(\alpha\beta\gamma), \tag{2.2}$$

where:

$$D^j_{km}(\alpha\beta\gamma) = e^{im\alpha}e^{ik\gamma}d^j_{km}(\beta), \tag{2.3}$$

in which the d^j_{km} can be expressed in terms of hypergeometric functions.

Note that several conventions exist for the definition of a rotation matrix, and, since it is necessary to adopt one, we are following the convention of Edmonds [13], which differs from that of other authors in that the rotation matrix defined above is considered as rotating the vectors rather than the coordinate frames, causing the Euler angles α, β and γ to be reversed in sign with respect to other conventions in which the Euler angles specify an active rotation of the frame. Note that the reason

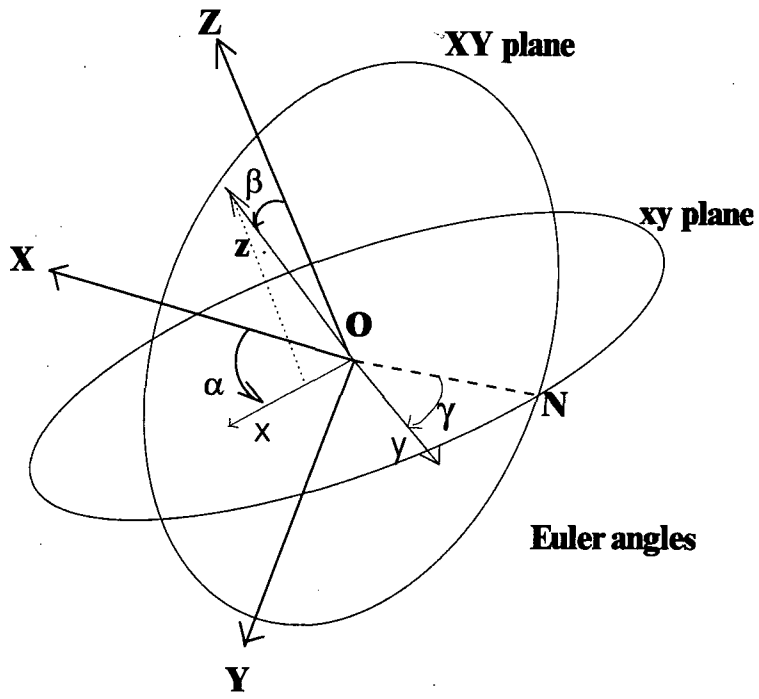

Figure 2.1: Euler angles rotating vectors in the space-fixed frame (X, Y, Z) into vectors in the body-fixed (x, y, z) frame. Angle γ lies in the xy plane, and measures the rotation of the intersection of the xy and XY planes about the z- axis. α and β are the polar coordinates of the z axis in the space-fixed frame.

why we adopt the convention of Edmonds is because of the use of this convention by Green and Hutson in the development of their MOLSCAT collision code, which is used in this work to obtain collision cross-sections.

Here, rotation matrices are denoted $D^j_{km}(\alpha\beta\gamma)$, where m is the projection of the total angular momentum **j** on the space-fixed Z-axis, and k is the projection of **j** on the body- fixed z axis (see Figure 2.1.) α and β are the polar coordinates of the z-axis in the space-fixed X, Y, Z system. γ is the angle, in the xy plane, measuring the rotation of the line of nodes ON (being the intersection of the xy and XY planes) anticlockwise about the z axis. Therefore, the lab component m is associated with angle α, since α constitutes a rotation about the Z axis. Likewise, k is associated with angle γ because the line of nodes rotates about the z axis.

Both quantum numbers, k and m, range from $-j$ to $+j$, so, for a general polyatomic molecule, each j state contains $(2j+1)$ possible states of k and $(2j+1)$ possible states of m.

Consider a threefold symmetric top molecule, with three identical nuclei symmetrically disposed about its symmetry axis (z). Let these three nuclei be labelled 1, 2 and 3 in sequence. If one rotates this threefold symmetric top molecule by $2\pi/3$ around its symmetry axis, an equivalent operation to this is exchanging 1 and 2, followed by exchange of 2 and 3 (If the nuclei are labeled 1, 2, 3 in the same sense as the rotation.) Since there are, in this operation, an even number of exchanges of fermion pairs (whose wavefunctions are antisymmetric under exchange), the total wavefunction must be symmetric under rotation by $2\pi/3$.

The only one of the Euler angles which changes with such a rotation is γ, which enters the wavefunction $|jkm>$ as $e^{ik\gamma}$. A rotation by $2\pi/3$ is equivalent to:

$$\Psi' = \Psi e^{i(2\pi/3)k} \tag{2.4}$$

Therefore, if k is a multiple of 3, the exponential equals 1, and so $\Psi' = \Psi$. The consequence of this is that Ψ is symmetric if k is a multiple of 3, and, if k is not a multiple of 3, then Ψ is neither symmetric or antisymmetric.

The Pauli principle states that no two identical fermions can have the same set of quantum numbers, and therefore the wavefunctions of all half-integer spin

particles (fermions) are antisymmetric with respect to exchange of any pair:

$$\Psi(1,2) = -\Psi(2,1). \tag{2.5}$$

Under a rotation by 2π the symmetric top wavefunctions transform in the following way:

$$\Psi_{jkm} \rightarrow (-1)^j \Psi_{j,-k,m}. \tag{2.6}$$

That is, they are neither symmetric or antisymmetric. However, the combination:

$$\Psi_{jkm} \pm \Psi_{j,-k,m} \tag{2.7}$$

transforms to:

$$(-1)^j [\Psi_{jkm} \pm \Psi_{j,-k,m}], \tag{2.8}$$

and is therefore symmetric for even values of j when the sign is + and antisymmetric when the sign is −, and *vice versa* for odd j. We require wave functions that are antisymmetric under *all* exchanges of identical nuclei. Here we considered exchange of 1 and 2, followed by exchange of 2 and 3, and sought wavefunctions symmetric under these combined exchanges. But if we consider exchange of 1 and 3, our previous forms are only antisymmetric when k is a multiple of 3. It is impossible to make these rotational wavefunctions antisymmetric under all exchanges unless we introduce the spin wavefunctions of the nuclei being exchanged (Townes and Schawlow [6]). The overall spin-rotational wavefunctions thus formed constitute the physically valid wavefunctions of the system.

The spin wavefunction of a nucleus specifies the projection of the spin on some fixed axis. For hydrogen, the spin projection can adopt only the values $\frac{1}{2}$ and $-\frac{1}{2}$. These two choices can be represented pictorially by arrows pointing up and down respectively. Table 2.1 shows the $2 \times 2 \times 2 = 8$ possible combinations of nuclear spin directions for a threefold symmetric rotor [6].

We see from Table 2.1 that, for example, II is symmetric under exchange of 2 and 3, but changes into III if 1 and 2 are exchanged. $1 \rightarrow 2$ followed by $2 \rightarrow 3$ is

Nucleus :	1	2	3
I	↑	↑	↑
II	↓	↑	↑
III	↑	↓	↑
IV	↑	↑	↓
V	↑	↓	↓
VI	↓	↑	↓
VII	↓	↓	↑
VIII	↓	↓	↓

Table 2.1: The 8 possible nuclear spin orientations for three nuclei [6]

equivalent to a $2\pi/3$ rotation, so II is not symmetric under rotation by $2\pi/3$.

If one rotates II by $2\pi/3$ by exchanging 1 and 2, followed by 2 and 3, the process can be seen pictorially as:

$\downarrow\uparrow\uparrow \rightarrow \uparrow\downarrow\uparrow \rightarrow \uparrow\uparrow\downarrow$,

the end result of which is IV. If we rotate IV by $2\pi/3$, we effect a rotation of the original spin wavefunction II by $4\pi/3$:

$\uparrow\uparrow\downarrow \rightarrow \uparrow\uparrow\downarrow \rightarrow \uparrow\downarrow\uparrow$,

which results in III. Another rotation by $2\pi/3$ brings us back to II again. Therefore the spin wavefunction:

$$(II + e^{2\pi ki/3} III + e^{4\pi ki/3} IV) \tag{2.9}$$

encompasses all the possible spin functions to which II can be converted by rotation. The result of exchanging, e.g., 1 and 3 is also present in this combination, since this exchange converts II into IV, and IV is included here.

Forming a product of this spin wavefunction with the sum and difference combination (2.7) of rotational wavefunctions seen earlier results in a wavefunction which is symmetric under all rotations [6]:

$$\Psi_{jkm}(II + e^{2\pi ki/3} III + e^{4\pi ki/3} IV) \pm \Psi_{j,-k,m}(II + e^{-2\pi ki/3} III + e^{-4\pi ki/3} IV) \tag{2.10}$$

In a similar fashion, we obtain:

$$\Psi_{jkm}(V + e^{2\pi ki/3}VI + e^{4\pi ki/3}VII) \pm \Psi_{j,-k,m}(V + e^{-2\pi ki/3}VI + e^{-4\pi ki/3}VII) \quad (2.11)$$

as another valid combination.

Notice that I and VIII in Table 2.1 are symmetric with respect to all exchanges. Therefore they are always symmetric, and an antisymmetric overall wavefunction is easily formed using these functions:

$$(\Psi_{jkm} \pm \Psi_{j,-k,m})I \quad (2.12)$$

and:

$$(\Psi_{jkm} \pm \Psi_{j,-k,m})VIII, \quad (2.13)$$

where one selects the + combination for even j values and the − combination for odd j, to ensure the terms in enclosed in brackets in (2.12) and (2.13) are antisymmetric.

The conclusion from this process of combining spin and rotational wavefunctions to form wavefunctions that are antisymmetric under *all* exchanges is that, for a symmetric rotor of the type considered, there are two distinct types of wavefunction which are allowed, and these are characterised by a symmetry under rotation by $2\pi/3$ in the case of the functions (2.12) and (2.13) involving I and VIII, and, by default, a symmetry under rotation by 2π in the case of the other two spin-rotational wavefunctions (2.10) and (2.11). Note also that for (2.12) and (2.13) the total nuclear spin is of magnitude $\frac{3}{2}$, whereas for the (2.10) and (2.11) the total spin is $\frac{1}{2}$.

2.3 Asymmetric tops

The general Hamiltonian for an asymmetric top is characterised by the rotational constants A, B and C, as in equation (2.1). This Hamiltonian does not have a

simple analytic solution because, while $p^2 = p_a^2 + p_b^2 + p_c^2$ is a constant of the motion, p_a, p_b and p_c are not. One therefore solves for the energy eigenvalues in a basis of symmetric top wavefunctions.

For an asymmetric top with rotational constants A, B and C, the so-called 'asymmetry parameter', κ, is defined as:

$$\kappa = \frac{2B - A - C}{A - C} \tag{2.14}$$

where κ varies from 1 (for a prolate symmetric top, $A = B$) to -1 (for an oblate symmetric top, $B = C$.) $\kappa = 0$ corresponds to the 'most asymmetric case', for which $B = \frac{1}{2}(A + C)$.

As the asymmetry parameter κ is varied from 1 to -1, a given prolate top energy level continuously splits, then the split levels re-connect in the oblate regime ($\kappa = -1$) with adjacent levels in the manner shown in Figure 2.2.

How the levels in the asymmetric rotor regime (intermediate κ) split and merge is governed by the direct product of the symmetry groups of the two limiting symmetric rotors (C_2 for both prolate and oblate.) The symmetry group to which the levels belong at intermediate κ is:

$$\Gamma(|J, K_a>) \otimes \Gamma(|J, K_b>) = C_2 \otimes C_2 = D_2, \tag{2.15}$$

where K_a and K_b are the z-projections of the total angular momentum J in the case of a prolate rotor and an oblate rotor respectively. Here, K denotes $\mid k \mid$, and J denotes $\mid j \mid$ (of course, j is always positive, but the capital J is useful in situations where j might be confused with an index). That is, the direct product of C_2 with another C_2 is the group D_2. Any asymmetric rotor has *at least* the symmetry D_2.

The symmetry group of the full Hamiltonian is D_2, which is the general group for an asymmetric top, not merely a top with threefold symmetry ($C_{3v}(M)$). This group is isomorphic to the Klein Four Group (the *Viergruppe*, **V**), which has four irreducible representations. Let us refer to these as A_1, A_2, B_1, and B_2.

The character table for the group D_2 is shown in Table 2.2, where E is the identity operator, and, for example, $C_2(z)$ is a two-fold rotation about the z axis.

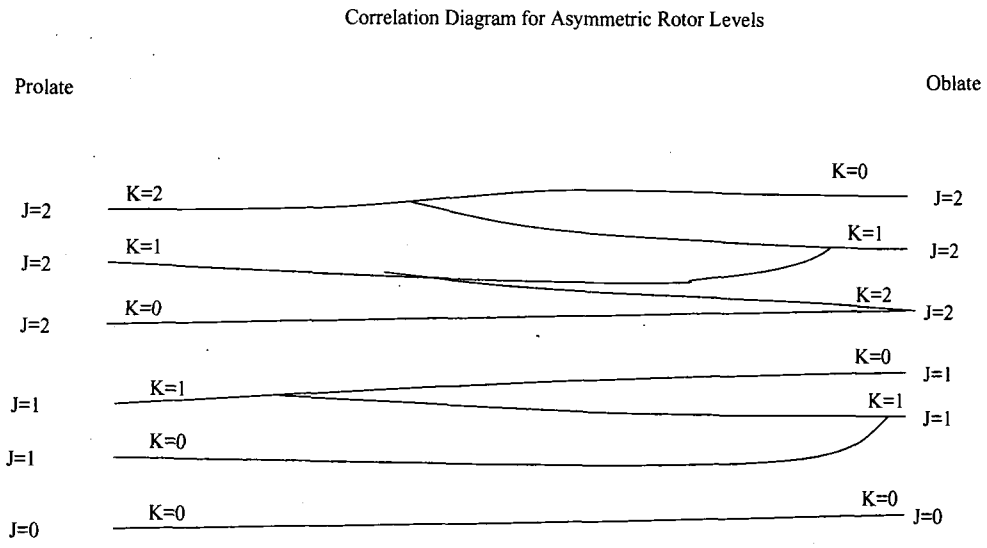

Figure 2.2: A correlation diagram, showing how different pairs of energy levels of a general asymmetric rotor become degenerate in the limiting cases of a prolate and oblate symmetric top.

$R:$	E	$C_2(z)$	$C_2(x)$	$C_2(y)$
$A_1:$	1	1	1	1
$A_2:$	1	1	-1	-1
$B_1:$	1	-1	-1	1
$B_2:$	1	-1	1	-1

Table 2.2: Character table of group D_2

J	K_a	Γ_{rot}	J	K_b	Γ_{rot}
even	0	A_1	*even*	0	A_1
odd	0	B_1	*odd*	0	B_2
	odd	$A_2 \oplus B_2$		*odd*	$A_2 \oplus B_1$
	even	$A_1 \oplus B_1$		*even*	$A_1 \oplus B_2$

Table 2.3: Symmetry types of symmetric top functions.

J, K_a			J, K_b
$2,2$	$A_1 \oplus B_1$	A_1	$2,0$
$2,1$	$A_2 \oplus B_2$	$A_2 \oplus B_1$	$2,1$
$2,0$	A_1	$A_1 \oplus B_2$	$2,2$
$1,1$	$A_2 \oplus B_2$	B_2	$1,0$
$1,0$	B_1	$A_2 \oplus B_1$	$1,1$
$0,0$	A_1	A_1	$0,0$

Table 2.4: Representations of prolate (left) and oblate top (right) levels for $J \leq 2$, using Table 2.3.

Uncombined symmetric top functions are not ideally suited to the treatment of an asymmetric rotor because, in general, they span reducible (i.e. mixed) representations of the D_2 group. One finds the representations Γ_{rot} generated by single symmetric top eigenfunctions by applying the D_2 group operations to them and noting their behaviour under these operations, with reference to the D_2 character table. $|J, K_a>$ and $|J, K_b>$ yield the representations [13] shown in Table 2.3.

Table 2.3 gives us the labels of the prolate and oblate top levels, where the labels are representations of the molecular point group. For example, all prolate top levels with even $K_a \neq 0$ are labeled $A_1 \oplus B_1$. Hence, using the information in Table 2.3, we can label the prolate and oblate top levels with the representations of D_2 shown in Table 2.4 (where only the first six levels are given.)

Wherever there are mixed – i.e. reducible – representations, one has a splitting/merging amongst adjacent levels as the asymmetry parameter is varied from the prolate case to the oblate case. Note that all the $K_a = K_b = 0$ levels remain unsplit (that is, irreducible.) By connecting (with lines) adjacent terms in mixed

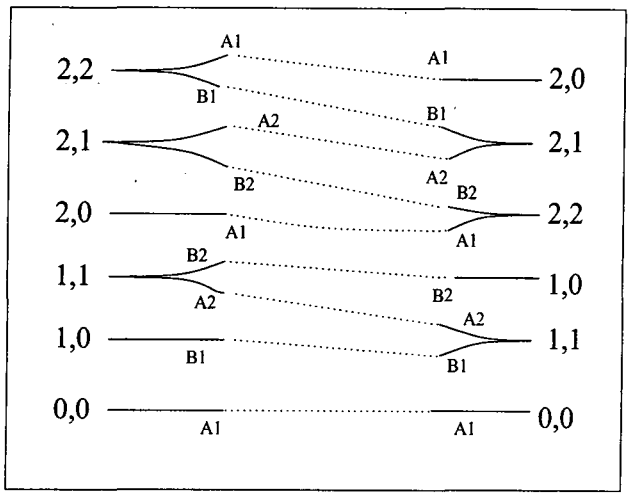

Figure 2.3: Symmetry types of prolate (left) and oblate top (right) levels (as in Table 2.4). Lines connect identical representations in the prolate and oblate regimes. Adding the level labels results in the correlation diagram (Figure 2.4.)

representations, Table 2.4 can be used to produce the diagram of prolate/oblate correlation, which is also a diagram of how the prolate top levels continuously split and merge to give oblate top levels, as the asymmetry parameter κ is increased. Also, we must use the fact that J, the total angular momentum, remains constant for a given line or split pair of lines as κ is varied. The result is shown in Figure 2.3.

Neither K_a or K_b are good quantum numbers for the asymmetric top (intermediate κ), but, because the prolate top can be changed *continuously* into an oblate top (by varying κ), and the fact that, for the limiting symmetric top cases (prolate and oblate), K_a and K_b *are* qood quantum numbers, we can quite easily specify an asymmetric top level by the K_a and K_b at its end-points. In this way, we specify each asymmetric top level, for a given J, by pairs of quantum numbers that are good quantum numbers in their respective limits.

A common notation for an asymmetric top level is $J_{K_aK_b}$. Alternatively, one

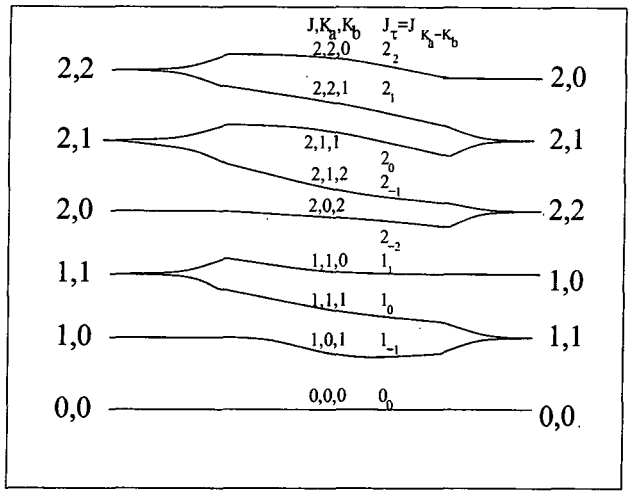

Figure 2.4: The correlation of asymmetric top levels with the corresponding good quantum numbers in the prolate (left) and oblate top (right) limiting cases.

also encounters the notation J_τ, where $\tau = K_a - K_b$. This notation is used in Figure 2.4 to label the correlated levels.

So far we have dealt with the reducible representations generated by single symmetric top eigenfunctions. As one may expect, there are certain combinations of symmetric top eigenfunctions which can generate *irreducible* representations of D_2. These turn out to be the exchange-antisymmetric rotational wavefunctions discussed in section 2.2.

Because the symmetric top functions $|jkm>$ are a complete set in the angles of orientation $\mathbf{\Omega} = (\alpha, \beta, \gamma)$, wavefunctions for the general asymmetric top can be expanded in this basis set. That is, using the index τ to label asymmetric top levels:

$$|jm\tau> = \sum_k a_{\tau k} |jkm> . \tag{2.16}$$

The character of the D_2 group operations, when applied to the symmetry-adapted wavefunctions, is found to be different for even k and odd k, and for

$\|Jk> + \|J,-k>$			
	J even	k even	A_1
	J even	k odd	B_2
	J odd	k even	A_2
	J odd	k odd	B_1
$\|Jk> - \|J,-k>$			
	J even	k even	A_2
	J even	k odd	B_1
	J odd	k even	A_1
	J odd	k odd	B_2

Table 2.5: Representations of symmetry-adapted wavefunctions

different signs + and − between the two terms, and these characters are such that the character table of the group D_2 is reproduced. The symmetry-adapted wavefunctions transform according to the irreducible representations of D_2 given in Table 2.5. Here we are employing the so-called III^r convention, in which the a, b and c axes (to which the moments of inertia A, B and C correspond) are identified with x, y and z respectively, where z is a principal axis. The III^r convention is the most convenient assignment for oblate tops (in which z corresponds to c), though there are six possible assignments (Papousek and Aliev [14]). See Section A of the Appendix for the alternative assignments.

We now illustrate the use of these functions in the block-diagonalization of the rigid asymmetric top Hamiltonian. Asymmetric top eigenfunctions with odd and even k do not mix in the Hamiltonian matrix, resulting in a considerable simplification. To verify this, one first rewrites the asymmetric top Hamiltonian in terms of total angular momentum J, its z-projection J_z, and the angular momentum ladder operators J^+ and J^-.

The angular momentum ladder operators are:

$$J^{+}_{-} = (J_x \pm i J_y), \tag{2.17}$$

yielding the Hamiltonian:

$$H = \frac{B}{2}[(J^+)^2 + (J^-)^2] + \frac{A}{2}[(J^+)^2 + (J^-)^2] + CJ_z{}^2. \tag{2.18}$$

The matrix elements of the asymmetric top Hamiltonian are known in the symmetric top basis [15]. The operators involved have non-vanishing elements:

$$< J, k, m \mid \hat{J}_z^2 \mid J, k, m >= k^2 \tag{2.19}$$

$$< J, k{-}2, m \mid (\hat{J}^+)^2 \mid J, k, m >= ([J(J+1) - (k-1)(k-2)][J(J+1) - k(k-1)])^{1/2} \tag{2.20}$$

$$< J, k{+}2, m \mid (\hat{J}^-)^2 \mid J, k, m >= ([J(J+1) - (k+1)(k+2)][J(J+1) - k(k+1)])^{1/2} \tag{2.21}$$

(all in units of $\hbar^2$). This results in the only non-vanishing elements of the Hamiltonian being those between the same J, k, m or between k-values differing by 2. It is clear that the rule established for the non-vanishing elements of the Hamiltonian implies the non-mixing of even and odd k-values. Therefore, it is apparent how the symmetry-adapted wavefunctions reflect the structure of the Hamiltonian matrix for an asymmetric top, because, if an element of the Hamiltonian matrix coupling a pair of functions is zero, this results in the functions belonging to distinct symmetry species.

Note that in the expressions (2.19)-(2.21) for the matrix elements of the angular momentum operators the quantum number m is absent, so when the total Hamiltonian is formed, it is found to be independent of m. Therefore, the asymmetric top possesses m-degeneracy, allowing us to consider only the case m=0 when evaluating expansion coefficients and energies.

2.4 Internal Rotation

2.4.1 The torsional potential

The methanol molecule is a near-symmetric top. It can be assumed that the C-atom of the methyl top lies on the molecular symmetry axis (z). This is a very good approximation, since moving the methyl group such that the C-atom lies exactly on the z-axis causes a mere 1.6 percent change in the ratio of rotational constants A/B. The implication is that the internal rotation can be described by a single coordinate, the angle γ, associated with the projection (let us say, k_{methyl}) of the angular momentum of the methyl top on the symmetry axis). For a symmetric top, the absolute value of the projection of the total angular momentum on the symmetry axis can be taken to be a good quantum number. Figure 2.5 is a diagram of the structure of methanol, the atoms being shown in their equilibrium positions, after Davis and Entley [11].

The internal rotation here is not free rotation – it is hindered. Classically, in the ground torsional state, the methyl group does not have sufficient energy for the average position of the oscillation about the potential minima to be rotated with respect to the potential governing this motion. This can only occur via quantum tunneling of the H -atoms through the 'walls' of the potential.

Clearly, the angle-dependent potential is required to be periodic in γ with period 2π, so (since trigonometric functions possess this property), we make the expansion:

$$V(\gamma) = \sum_n a_n \cos(n\gamma). \tag{2.22}$$

By a shift in the reference level of the potential energy, this may be written as [16]:

$$V(\gamma) = \frac{V_3}{2}(1 - \cos 3\gamma) + \frac{V_6}{2}(1 - \cos 6\gamma) + ... \tag{2.23}$$

in the case of a threefold barrier. We are, however, justified in retaining only the first term in the series, because experimental data suggests that the V_6 part of the

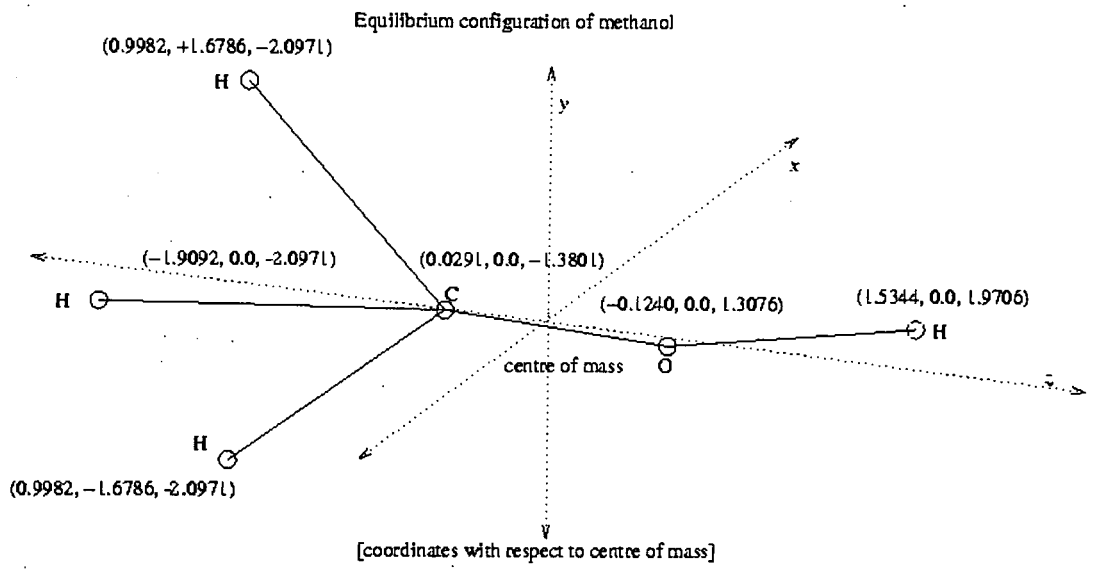

Figure 2.5: Equilibrium configuration of methanol. Distances are given in Bohr radii.

potential is much smaller than the V_3 part – in fact, approximately one hundred times smaller. The potential therefore becomes:

$$V(\gamma) = \frac{V_3}{2}(1 - \cos 3\gamma). \tag{2.24}$$

In order to proceed any further, however, it is necessary to know the manner in which torsion and overall rotation couple together, and what the form of the Hamiltonian is for an asymmetric top capable of undergoing torsion in the way described.

2.4.2 The total Hamiltonian of a non-rigid asymmetric top

Here we describe the so-called 'Internal Axis Method' (IAM), due to Lin and Swalen [7], of obtaining a Hamiltonian which is modified by the presence of internal rotation. The Hamiltonian resulting from this method is referred to as the 'IAM Hamiltonian'. The derivation given here is that of Lin and Swalen [7]. For an asymmetric molecule with a plane of symmetry, a set of coordinate axes is chosen so that the c axis passes through the centre of mass of the whole molecule and is collinear with the axis of the internal rotor (this being a good approximation in the case of methanol), and the b axis intersects the centre of mass and lies in the plane of symmetry. The c axis is therefore the axis of symmetry here. The inertia tensor assumes the form [7]:

$$\begin{pmatrix} I_{aa} & 0 & 0 \\ 0 & I_{bb} & -I_{bc} \\ 0 & -I_{bc} & I_{cc} \end{pmatrix}, \tag{2.25}$$

where I_{aa}, I_{bb}, and I_{cc} are the moments of inertia, and the off-diagonal elements I_{bc} are known as 'products of inertia'.

Let $\bar{\omega} = (\omega_a, \omega_b, \omega_c)$, where ω_a, ω_b, and ω_c are the components of the angular velocity about the a, b and c axes. Also, let $\bar{\gamma} = (0, 0, \gamma)$. In tensor notation, the kinetic energy can be written:

$$T = \frac{1}{2}\bar{\omega}^T \cdot \mathbf{I} \cdot \bar{\omega} + \frac{1}{2}\left(\frac{\partial\bar{\gamma}}{\partial t}\right)^T \cdot \mathbf{I}_\gamma \cdot \left(\frac{\partial\bar{\gamma}}{\partial t}\right) + \frac{1}{2}\left[\bar{\omega}^T \cdot \mathbf{I}_\gamma \cdot \left(\frac{\partial\bar{\gamma}}{\partial t}\right) + \left(\frac{\partial\bar{\gamma}}{\partial t}\right)^T \cdot \mathbf{I}_\gamma \cdot \bar{\omega}\right], \tag{2.26}$$

where ^{T} denotes a transpose, and $\mathbf{I}_\gamma$ is the moment of inertia of the top about its symmetry axis.

Substituting the inertia tensor into the above expression, we obtain, using $\dot{\gamma}$ to represent the angular velocity of the methyl top relative to the OH-group:

$$T = \frac{1}{2}I_{aa}\omega_a^2 + \frac{1}{2}I_{bb}\omega_b^2 + \frac{1}{2}I_{cc}\omega_c^2 - I_{bc}\omega_b\omega_c + \frac{1}{2}I_\gamma\dot{\gamma}^2 + I_\gamma\omega_c\dot{\gamma}. \tag{2.27}$$

Similarly, the momenta are defined as:

$$P_a = \partial T/\partial\omega_a = I_{aa}\omega_a, \tag{2.28}$$

$$P_b = \partial T/\partial\omega_b = I_{bb}\omega_b - I_{bc}\omega_c, \tag{2.29}$$

$$P_c = \partial T/\partial\omega_c = I_{cc}\omega_c - I_{bc}\omega_b + I_\gamma\dot{\gamma}, \tag{2.30}$$

$$p = \partial T/\partial\gamma = I_\gamma(\dot{\gamma} + \omega_c). \tag{2.31}$$

With the substitution of these components of the total angular momentum into the expression for the angular kinetic energy, we obtain the following quantum-mechanical Hamiltonian:

$$H = A_aP_a^2 + B_bP_b^2 + C_c^2P_c^2 + D_{bc}(P_bP_a + P_cP_b) - 2D_{bc}P_bp - 2C_cP_cp + Fp^2 + V(\gamma), \tag{2.32}$$

where we have introduced the effective rotational constants given by Lin and Swalen [7] to simplify the Hamiltonian given above. These effective rotational constants are:

$$A_a = \frac{\hbar^2}{2I_{aa}}, \tag{2.33}$$

$$B_b = \frac{\hbar^2(I_{cc} - I_\gamma)}{2(I_{bb}I_{cc} - I_\gamma I_{bb} - I_{bc}^2)}, \tag{2.34}$$

$$C_c = \frac{\hbar^2 I_{bb}}{2(I_{bb}I_{cc} - I_\gamma I_{bb} - I_{bc}^2)}, \tag{2.35}$$

$$D_{bc} = \frac{\hbar^2 I_{bc}}{2(I_{bb}I_{cc} - I_\gamma I_{bb} - I_{bc}^2)}, \tag{2.36}$$

$$F = \frac{\hbar^2(I_{bb}I_{cc} - I_{bc}^2)}{2I_\gamma(I_{bb}I_{cc} - I_\gamma I_{bb} - I_{bc}^2)}. \tag{2.37}$$

Having obtained the Hamiltonian (making use of the structural symmetry of the methanol molecule), one notices that there are terms involving $P_c p$ and $P_b p$. These terms imply a coupling between the overall rotation and the internal rotation, which we would ideally like to remove by an appropriate transformation. The method of Lin and Swalen [7] is to apply two transformations to the Hamiltonian (2.32) given above. First, a rotation is performed in order to eliminate the $P_b p$ coupling. Secondly, a 'Nielsen transformation' is applied to remove the $P_c p$ coupling. These transformations are given by :

$$P_a'' = P_a \tag{2.38}$$

$$P_b'' = (I_{bb}P_b - I_{bc}P_c)(I_{bb}^2 + I_{bc}^2)^{-\frac{1}{2}} \tag{2.39}$$

$$P_c'' = (I_{bc}P_b + I_{bb}P_c)(I_{bb}^2 + I_{bb}^2)^{-\frac{1}{2}} \tag{2.40}$$

and

$$p' = p - \rho P_c'', \tag{2.41}$$

where ρ is:

$$\rho = I_\gamma(I_{bb}^2 + I_{bc}^2)^{\frac{1}{2}}(I_{bb}I_{cc} - I_{bc}^2)^{-1}. \tag{2.42}$$

The transformed Hamiltonian which results from these two operations is:

$$H'' = A_a P''^2_a + B''_b P''^2_b + C''_c P''^2_c + D''_{bc}(P''_b P''_c + P''_c P''_b) + F p'^2 + V(\gamma), \quad (2.43)$$

where:

$$B''_b = \frac{\hbar^2}{2} I_{bb}(I^2_{bb} + I^2_{bc})^{-1}, \quad (2.44)$$

$$C''_c = \frac{\hbar^2}{2}\left[\frac{I_{bb} + I_{cc}}{I_{bb}I_{cc} - I^2_{bc}} - \frac{I_{bb}}{I^2_{bb} + I^2_{bc}}\right], \quad (2.45)$$

$$D''_{bc} = \frac{\hbar^2}{2} I_{bc}(I^2_{bb} + I^2_{bc})^{-1}. \quad (2.46)$$

The Hamiltonian (2.43) can be divided up into a symmetric part, analogous to the levels of a symmetric top (except for the substitution of rotational constants by effective rotational constants), an asymmetric part, and a torsional part which contains the kinetic and potential energy associated with internal rotation:

$$H = H_0 + H_1 + H_T, \quad (2.47)$$

where:

$$H_0 = \frac{1}{2}(A_a + B''_b)(P''^2_a + P''^2_b) + C''_c P''^2_c \quad (2.48)$$

$$H_1 = \frac{1}{2}(A_a - B''_b)(P''^2_a - P''^2_b) + D''_{bc}(P''_b P''_c + P''_c P''_b) \quad (2.49)$$

$$H_T = F p'^2 + V(\gamma), \quad (2.50)$$

in which $V(\gamma) = \frac{1}{2}V_3(1 - \cos 3\gamma)$.

Then we choose the eigenfunctions of H_0 – i.e. the symmetric top part – as the basis functions for constructing the energy matrix. These functions are:

$$|Jkm_t> = |Jk>|km_t>, \quad (2.51)$$

where the ordinary symmetric rotor eigenfunctions are $|Jk>$, and the torsional part is [8]:

$$|km_t>=(2\pi)^{-\frac{1}{2}}e^{i\rho k\gamma}e^{im_t\gamma}, \tag{2.52}$$

m_t being the torsional quantum number, which is defined by this equation.

Note that:

$$\rho=\frac{(I_{bb}^2+I_{bc}^2)^{\frac{1}{2}}I_\gamma}{(I_{bb}I_{cc}-I_{bc}^2)}, \tag{2.53}$$

where I_γ is the moment of inertia of the methyl group.

One now has a suitable basis, derived by separating the transformed Hamiltonian into 3 parts. If we take the original unseparated IAM Hamiltonian and form the matrix elements of it with the basis $|Jkm_t>$, then we obtain the non-zero values [7]:

$$<km_t|H|km_t'>=(\frac{1}{2}(A_a+B_b'')[J(J+1)-k^2]+C_c''k^2+E_{km_t})\delta_{m_tm_t'}, \tag{2.54}$$

and in the limit of a high barrier to internal rotation:

$$<km_t|H|k+1,m_t'>=(D_{bc}''(k+\frac{1}{2})[J(J+1)-k(k+1)]^{\frac{1}{2}})\delta_{m_tm_t'} \tag{2.55}$$

$$<km_t|H|k+2,m_t'>=(-\frac{1}{4}(A-B_b'')[J(J+1)-k(k+1)^{\frac{1}{2}}][J(J+1)-(k+1)(k+2)]^{\frac{1}{2}})\delta_{m_tm_t'}, \tag{2.56}$$

where E_{km_t} are the eigenvalues of the torsional Mathieu equation. These eigenvalues can be calculated, and the results compared with the known (spectroscopic) energy levels. E_{km_t} is a function of k, so, in general, different E_{km_t} are needed for the $+k$ and $-k$ states.

2.4.2 Torsional symmetry types of methanol

Now that the necessary total Hamiltonian has been given, let us look, in particular, at the torsional part of this Hamiltonian in isolation. One can write the torsional Hamiltonian introduced in the previous section as [8]:

$$H_T^0 = Fp'^2 + \frac{1}{2}V_3(1 - \cos 3\gamma), \tag{2.57}$$

where F is a constant for the top, as in Lin and Swalen [7], and $p' = \frac{\partial}{\partial\gamma}$. The first term is the angular kinetic energy due to this relative rotation.

The only off-diagonal elements of the torsional Hamiltonian matrix in a (k, m_t) basis are displaced from the diagonal in m_t by $\pm$ 3. Therefore, the Hamiltonian is tridiagonal, that is, its non-zero elements are the diagonal terms, the lower 'displaced diagonal', and the upper 'displaced diagonal'. These separate, non-coupled parts of the torsional Hamiltonian can be characterised by an index $\sigma = 0, \pm 1$. We form the Hamiltonian in the (k, m_t) basis:

$$< km_t|H_T^0|k'm_t' >= F < km_t|p'^2|k'm_t' > + \frac{1}{2}V_3 < km_t|k'm_t' > - \frac{1}{2}V_3 < km_t|\cos 3\gamma|k'm_t' > . \tag{2.58}$$

This equation for the torsional energy involving the Hamiltonian in the (k, m_t) basis is referred to as the Mathieu Equation. The Mathieu Equation rearranges as [8]:

$$\frac{1}{\alpha}\frac{d^2M}{d\gamma^2} + (R + 2\cos 3\gamma)M = 0, \tag{2.59}$$

where

$$\alpha = V_3/4F, \qquad R = (4/V_3)(W - \frac{1}{2}V_3), \tag{2.60}$$

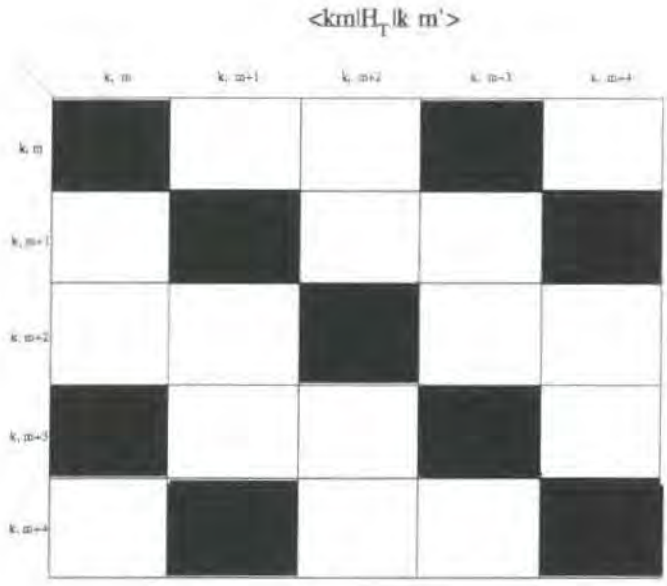

Figure 2.6: Matrix elements of torsional Hamiltonian

W is the torsional energy, and M are the eigenfunctions of the Mathieu Equation, given by:

$$M = (2\pi)^{-\frac{1}{2}} e^{i\rho k\gamma} \sum_{m_t} a_{m_t} e^{im_t\gamma}. \tag{2.61}$$

Multiplying by M* and integrating over γ from 0 to 2π, one obtains

$$R = \alpha^{-1}(m_t + \rho k)^2 + (1/D_{m_t+3}) + (1/D_{m_t-3}). \tag{2.62}$$

where $D_{m_t\pm 3} = -a_{m_t}/a_{m_t\pm 3}$.

It is now apparent that the Hamiltonian, when expressed in this basis, will naturally separate into three parts (diagonal, upper diagonal and lower diagonal), as in Figure 2.6. Note that R is basically the torsional energy minus the barrier height V_3.

This natural separation, for any given k, m_t, into m_t, m_t-3, and m_t+3 parts is the motivation for introducing the torsional 'species' label σ, because factorable blocks of the Hamiltonian matrix reflect the symmetries of the Hamiltonian, and hence the symmetries of the molecule itself. We define σ as:

m_t=$3s+\sigma$, where s is any integer.

Because the index σ is present in the torsional eigenfunctions (via m_t), each of these distinct torsional symmetry species has its own set of torsional energy levels. These distinct stacks of torsional energy levels are included in the calculation of the resulting energy levels of the entire rotor via the addition of the eigenvalues of the Mathieu Equation to the diagonal terms of the IAM Hamiltonian for the non-rigid rotor.

The torsional barrier height V_3 is present as a factor in the Mathieu equation, and this equation supplies the torsional energy eigenvalues, which are incorporated into the total Hamiltonian. The barrier height thus determines the rotational energy levels of a particular torsional species of methanol. Hence we can infer the barrier height from the observed levels.

As the index s is varied, the level of torsional excitation is altered for a given σ. These torsional levels can be ordered in terms of increasing energy, each level being labelled by an index v_t which indicates the order in this stack of torsional levels.

Also note that the energy eigenvalues are unchanged when one alters the signs of k and σ simultaneously:

$$E_{kv_t\sigma} = E_{-kv_t,-\sigma} \tag{2.63}$$

This causes the energy submatrices for $\sigma = 1$ and $\sigma = -1$ to be doubly degenerate. Since v_t is a nearly good quantum number (because the off-diagonal elements in v_t are small), a torsional level is labeled v_t and σ, and, associated with each torsional σ, v_t 'species' one has a set of rotational energy levels with the quantum numbers j, k. Also, there is a selection rule $\Delta\sigma = 0$, hence different torsional symmetry species do not inter-convert.

The torsional eigenstates, which are solutions of the Mathieu Equation, were given earlier (equation (2.61)). Writing m_t explicitly in terms of σ and expressing these eigenfunctions in terms of the quantum numbers which specify each torsional state, we have:

C_{3v} :	E	$2C_3$	$3\sigma_v$
E :	2	-1	0
A_1 :	1	1	1
A_2 :	1	1	-1

Table 2.6: Character table of C_{3v}

$$|k, v_t, \sigma >= (2\pi)^{-\frac{1}{2}} e^{i\rho k\gamma} \sum_s a_{3s+\sigma}^{kv_t} e^{i(3s+\sigma)\gamma} \tag{2.64}$$

These eigenstates satisfy an obvious boundary condition on the wavefunctions of internal rotation, i.e. single-valuedness under the operation $\gamma \rightarrow \gamma + 2\pi$. In fact, these eigenstates satisfy this condition in two ways. One type of eigenstate has period 2π in γ, and the other has period $2\pi/3$. These correspond to the two different types of spin-rotational wavefunction for a three-fold symmetric top, the eigenstate with period $2\pi/3$ being the case in which the three atoms symmetrically disposed about the symmetry axis have all their nuclear spins aligned in the same direction, and the period 2π solutions being the mixed spin states. When $\sigma = 0$ one has torsional eigenstates with period $2\pi/3$, and when $\sigma = -1$ or 1, the eigenstate merely has the default periodicity of 2π. Any discussion of torsion in methanol therefore involves the symmetry group of a three-fold symmetric top, which is referred to as C_{3v}. The character table for C_{3v} is given in Table 2.6.

In Table 2.6 we are using the conventional notation given in most character tables, in which C_3 are the two (+ and $-$) threefold rotations about the symmetry axis, and σ_v are the three reflection operations in the three vertical symmetry planes of the methyl top. Note that the number of classes, or irreducible representations, of the group is always equal to the number of group operations.

Let us determine the symmetry species of the three-fold symmetric top eigenfunctions. In order to do this, one looks at the symmetry of the molecule in question and chooses a group symmetric under the appropriate number of n-fold rotations. This condition is clearly satisfied by C_{3v}. One then applies the operations listed in the character table, which constitute the elements of this group, to each of the eigenfunctions in turn. The trace of the matrix (or, for groups with one- dimen-

function		
	J_{even}	J_{odd}
$\|J,0,m>$	A_1	A_2
$\|J,+1,m>$, $\|J,-1,m>$	E	E
$\|J,+2,m>$, $\|J,-2,m>$	E	E
$\|J,+3,m> + \|J,-3,m>$	A_2	A_1
$\|J,+3,m> - \|J,-3,m>$	A_1	A_2

Table 2.7: Representations of symmetric top eigenfunctions in C_{3v}

sional representations, the number) which effectively multiplies the eigenfunction on the application of this operation is the character of the operation, which is then compared with the characters of the symmetry species under each operation. When this is done for the C_{3v} molecular point group, the operations in C_{3v} turn out to have the following effect on symmetric rotor eigenfunctions (Papousek and Aliev, [14]):

$$C_3|J,k,m>= e^{2\pi ik/3}|J,k,m> \tag{2.65}$$

$$\sigma_v|J,k,m>= (-1)^{J-k}|J,k,m> \tag{2.66}$$

Hence, e.g., for $k = 0$ and $J =$ even, one has $e^{2\pi ik/3} = 1$ and $(-1)^{J-k} = 1$, and so this particular $|Jkm>$ belongs to the species A_1. Note that m, the space-fixed projection of the total angular momentum J, is not to be confused with the torsional quantum number m_t defined in equation (2.61).

From these behaviours, we find that the symmetric top eigenfunctions under the condition of a C_{3v} molecular point group belong to the symmetry species given in Table 2.7 (where the quantum number k should be considered as being k modulo 3.)

The symmetry group of the torsional eigenfunctions is isomorphic to the group C_{3v}. Note that $m_t = 3s + \sigma$ is the torsional quantum number, equivalent to k in the case of the symmetric top. Therefore we also know that the symmetry types of the torsional eigenfunctions are as given in Table 2.7, where, again, the quantum

torsional function	species
$e^{i\gamma}, e^{-i\gamma}$	E
$e^{i2\gamma}, e^{-i2\gamma}$	E
$e^{i3\gamma} + e^{-i3\gamma}$	A_1
$e^{i3\gamma} - e^{-i3\gamma}$	A_2

Table 2.8: Symmetry types of torsional eigenfunctions

number m_t involved is implicitly modulo 3. The resulting symmetry types of the torsional eigenfunctions are given in Table 2.8. Note that these torsional symmetry types are independent of k and J. Therefore, for every torsional symmetry type of methanol, there exists a complete stack of J, k levels. The torsional species σ relating to the m_t torsional quantum number appearing in the eigenstates can now be seen to reflect the fact that different symmetry species are possible. The three symmetry species highlighted by this structure of the torsional Hamiltonian are referred to as A, E_1 and E_2:

$\sigma = 0 \rightarrow A_1, A_2$

$\sigma = 1 \rightarrow E$

$\sigma = -1 \rightarrow E$.

This is because $m_t = 3$ mod 3 for $\sigma = 0$, $m_t = (3\text{-}1)$ mod 3 for $\sigma = -1$, and $m_t = (3+1)$ mod 3 for $\sigma = 1$.

There is a possible source of confusion here regarding the notation used in many papers on the subject of methanol's internal rotation. E_1 and E_2 are commonly used to denote the E-type levels which have $\sigma = 1$ and $\sigma = -1$. In fact, E_1 and E_2 are *not* different symmetry species; they are both classified under the E species, and they refer to the two possible directions of rotation of the methyl group. This is to be contrasted with A_1 and A_2, which *do* represent distinct symmetry types, despite the fact that, for both A_1 and A_2, the index σ is 0. The A_1 and A_2 levels, however, are degenerate, hence their association with a single σ value in the Hamiltonian matrix. For this reason, methanol is referred to as either A-type or E-type, dropping the distinction between A_1 and A_2.

To summarise: when one analytically determines the eigenfunctions of the

Hamiltonian (kinetic energy plus threefold potential barrier) associated with this torsional motion, one finds that two types of energy eigenfunctions are capable of satisfying the boundary condition of single-valuedness under $\gamma \rightarrow \gamma + 2\pi$. The first type has period 2π in γ, and the second type has period $2\pi/3$ in γ. Both types of eigenfunction are allowed, and they are not capable of interconversion. They constitute distinct symmetry species of methanol, the types being referred to as E-type methanol and A-type methanol respectively.

Physically, the presence of two distinct symmetry species can be understood from a semi-classical point of view– that is, in terms of the methyl group rotating or oscillating in a classical manner, while recognising the purely quantum mechanical effects which give rise to this behaviour (specifically, tunneling of Hydrogen atoms through the maxima of the threefold torsional potential to adjacent positions). A back-and-forth oscillation about the equilibrium configuration of the molecule gives rise to the set of E-levels, corresponding to the onefold periodic eigenfunctions of the torsional Hamiltonian. In the case of E-type methanol, 'internal rotation' is a misnomer, since it is really linear 'internal vibration' which characterises this mode [7].

The A-levels can be associated with a different mode of internal motion in which the Hydrogen atoms of the methyl group pass from one equivalent equilibrium configuration to another in a circulatory manner through the tunneling effect. This mode reflects the threefold periodicity of the corresponding eigenfunctions.

Both the torsional and spin wavefunctions involve the same exchanges of identical nuclei, so they have the same symmetry properties. Therefore, referring back to the discussion of spin-rotational wavefunctions of a threefold symmetric top given in section 2.2, the torsional eigenfunctions can take the place of the spin wavefunctions. Using the periodicity of the A and E type functions, we have $I = \frac{3}{2}$ for A and $I = \frac{1}{2}$ for E. Therefore, since spin functions I and $VIII$ are associated with $I = \frac{3}{2}$, and the rest with $I = \frac{1}{2}$, we have:

E-type, $I = \frac{1}{2}$:

$$\Psi_{jkm}[e^{i\gamma}e^{i\rho k\gamma}] \pm \Psi_{j,-k,m}[e^{-i\gamma}e^{-i\rho k\gamma}] \tag{2.67}$$

$$\Psi_{jkm}[e^{i2\gamma}e^{i\rho k\gamma}]^{+}_{-}\Psi_{j,-k,m}[e^{-i2\gamma}e^{-i\rho k\gamma}] \tag{2.68}$$

A-type, $I = \frac{3}{2}$:

$$(\Psi_{jkm}{}^{+}_{-}\Psi_{j,-k,m})[e^{i3\gamma}e^{i\rho k\gamma} - e^{-i3\gamma}e^{i\rho k\gamma}] \tag{2.69}$$

$$(\Psi_{jkm}{}^{+}_{-}\Psi_{j,-k,m})[e^{i3\gamma}e^{i\rho k\gamma} + e^{-i3\gamma}e^{i\rho k\gamma}], \tag{2.70}$$

where the torsional quantum number m_t is again understood to be modulo 3.

If all three nuclear spins of the Hydrogen atoms in the methyl group are parallel one has a total nuclear spin of $I = 3/2$. In this case, for the overall wavefunction to be antisymmetric in terms of exchange of identical nuclei, only states with A- symmetry are allowed. This is simply a consequence of the transformation properties of the combined nuclear spin and rotation wavefunctions. Conversely, if $I = 1/2$ (i.e. the nuclear spins of one pair of Hydrogen atoms is antiparallel) then the result is that, for $\Psi_{rot}\Psi_{nspin}$ to be antisymmetric with respect to exchange, only E-states are allowed.

Chapter 3

Collision Theory

3.1 The scattering formalism

In this section, we summarise the primary formulation, due to Arthurs and Dalgarno [17], of the exact (Close Coupling or 'CC') approach to atom-molecule collisions. Note that Arthurs and Dalgarno applied their general approach to atom-diatom collisions, whereas here we are concerned with atom-symmetric top collisions, which are easily extended to atom-asymmetric top collisions via expansion of the asymmetric top wavefunction in a basis of symmetric top eigenfunctions. Later, in sections 3.2 and 3.3, we introduce the most common approximations to the CC equations, these being less computationally intensive than the full CC approach.

The total Hamiltonian for the collision of an atom with a rigid asymmetric rotor can be written, in space-fixed coordinates (i.e. coordinates which do not rotate with the molecule, but only translate to follow the centre of mass of the system [18]):

$$H = H_{st}(\mathbf{\Omega}) + T(\mathbf{R}) + V(\mathbf{\Omega}, \mathbf{R}), \tag{3.1}$$

where $\mathbf{\Omega} = (\alpha, \beta, \gamma)$, in which α, β and γ are the Euler angles defined in Chapter 2 (Figure 2.1), which rotate the space-fixed (SF) axes into the body-fixed (BF) axes. These angles therefore specify the orientation of the rotor relative to the lab

frame in which the collision is observed. The BF axes are aligned with the principal moment of inertia axes of the molecule.

The coordinate of the atom with respect to the rotor's centre of mass is $\mathbf{R} = (R, \Theta, \Phi)$, and the angular part of this will, from now on, be referred to as $\hat{\mathbf{R}} = (\Theta, \Phi)$.

Note that, in the Hamiltonian above, H_{at} is the asymmetric top Hamiltonian (a function of angle $\mathbf{\Omega}$ only), and T is the kinetic energy of the atom relative to the centre of mass. V, the atom-molecule interaction potential, is a function of both $\mathbf{\Omega}$ and $\mathbf{R}$. The kinetic energy operator is:

$$T(\mathbf{R}) = -\frac{\hbar^2}{2\mu}\nabla_R^2 = -\frac{\hbar^2}{2\mu}(\frac{1}{R}\frac{d^2}{dR^2}R - \frac{\mathbf{l}^2}{R^2}), \tag{3.2}$$

where μ is the reduced mass of the atom and the rotor, and $\mathbf{l}$ is the orbital angular momentum operator.

For the full close-coupling (CC) treatment, we form the coupled total angular momentum functions:

$$|JMjkl> = \sum_{m,m_l} < jmlm_l|JM > |jkm > |lm_l >, \tag{3.3}$$

where $|jkm >$ are the symmetric top functions (see equation (2.2)):

$$|jkm > = [(2j+1)/8\pi^2]^{\frac{1}{2}} D^j_{km}(\alpha\beta\gamma), \tag{3.4}$$

and $M = m + m_l$. The rotation matrices $D^j_{km}(\alpha\beta\gamma)$ are as defined in Chapter 2.

The $|lm_l >$ are the 'partial wave functions':

$$|lm_l > = Y_{lm_l}(\Theta, \Phi), \tag{3.5}$$

and $< j_1 m_1 j_2 m_2 | j_3 m_3 >$ is a Clebsch-Gordan vector-coupling coefficient, which, from now on, we will denote by the alternative notation:

$$C^{j_1 j_2 j_3}_{m_1 m_2 m_3} = < j_1 m_1 j_2 m_2 | j_3 m_3 > . \tag{3.6}$$

The scattering wavefunction with total angular momentum J (and its z-projection M) associated with the entrance channel jkl satisfies the Schrödinger equation:

$$[H_{st} - (\hbar^2/2\mu)\nabla_R^2 + V - E - E_{jk}]\Psi^{JM}_{jkl} = 0, \tag{3.7}$$

where E is the relative collision energy, E_{jk} is the 'internal' energy of the rotor, and H_{st} is the symmetric top Hamiltonian.

One then expands Ψ_{jkl}^{JM} in the basis of coupled total angular momentum functions, with radially dependent expansion coefficients:

$$\Psi_{jkl}^{JM} = \sum_{j'k'l'} u_{j'k'l'}^{JMjkl}(R)\frac{1}{R}|JMj'k'l' > . \tag{3.8}$$

Substituting equation (3.8) into equation (3.7) yields the usual coupled equations for the radial wavefunctions [18]:

$$[\frac{d^2}{dR^2} - \frac{l(l+1)}{R^2} + \kappa_{j'k'}^2]u_{j'k'l'}^{JMjkl}(R) = (\frac{2\mu}{\hbar^2}) \sum_{j''k''l''} < JMj''k''l''|V|JMj'k'l' > u_{j''k''l''}^{JMjkl}(R), \tag{3.9}$$

where the variable $\kappa_{j'k'}^2$ is the wavenumber:

$$\kappa_{j'k'}^2 = (\frac{2\mu}{\hbar^2})(E + E_{j'k'}). \tag{3.10}$$

One can expand the body-fixed angular dependence of the potential V in spherical harmonics, with the expansion coefficients being a function of R:

$$V(\mathbf{R}) = \sum_{\lambda,\mu} v_{\lambda\mu}(R)Y_{\lambda\mu}(\Theta,\Phi). \tag{3.11}$$

The body-fixed frame (as defined in Figure 2.1) is the natural frame in which to express the atom-molecule interaction potential. However, the symmetric top eigenfunctions are in the SF frame, which is also the frame in which the collision cross-sections are required. Therefore we express all BF functions of Θ and Φ in terms of their corresponding SF forms, in which our coordinates become $\mathbf{R} = (R', \Theta', \Phi')$, instead of $\mathbf{R} = (R, \Theta, \Phi)$, after rotation of the frame through the Euler angles $\mathbf{\Omega}$. Note that $R' = R$, since rotation does not affect the radial cooordinate.

$$V(\mathbf{\Omega}, \mathbf{R}) = V(R', \Theta', \Phi') = \sum_{\lambda\mu\mu'} v_{\lambda\mu}(R)D_{\mu\mu'}^{\lambda *}(\alpha\beta\gamma)Y_{\lambda\mu'}(\Theta,\Phi). \tag{3.12}$$

Forming the matrix elements of this potential in our basis of spherical harmonics and symmetric rotor eigenfunctions, we have:

$$< JMjkl|V|JMj'k'l' > = < JMjkl| \sum_{\lambda\mu\mu'} v_{\lambda\mu'}(R)D_{\mu\mu'}^{\lambda *}Y_{\lambda\mu'}(\Theta,\Phi)|JMj'k'l' > \tag{3.13}$$

$$= [(2j+1)/8\pi^2]^{\frac{1}{2}}[(2j'+1)/8\pi^2]^{\frac{1}{2}} \int d\mathbf{\Omega} \int d\hat{\mathbf{R}} \sum_{mm'\lambda\mu\mu'} C_{mm_lM}^{jlJ}$$

$$\times D_{km}^{j*}(\alpha\beta\gamma)Y_{lm_l}^*(\Theta,\Phi)v_{\lambda\mu}(R)D_{\mu\mu'}^{\lambda *}Y_{\lambda\mu}(\Theta,\Phi)C_{m'm_l'M}^{j'l'J}D_{k'm'}^{j'}Y_{l'm_l'}(\Theta,\Phi).$$

The next step is to relate the spherical harmonics appearing in equation (3.13) to their equivalent rotation matrices, using the formula [18]:

$$Y_{\lambda\mu}(\beta\gamma) = (-1)^{\mu}(\frac{2\lambda+1}{4\pi})^{\frac{1}{2}} D^{\lambda}_{\mu 0}(\alpha\beta\gamma). \tag{3.14}$$

This converts (3.13) into:

$$\begin{aligned} < JMjkl|V|JMj'k'l' >= [(2j+1)/8\pi^2]^{\frac{1}{2}}[(2j'+1)/8\pi^2]^{\frac{1}{2}}(\frac{2l+1}{4\pi})^{\frac{1}{2}} \\ \times(\frac{2\lambda+1}{4\pi})^{\frac{1}{2}}(\frac{2l'+1}{4\pi})^{\frac{1}{2}} \int d\mathbf{\Omega} \int d\hat{\mathbf{R}} \sum_{mm'\lambda\mu\mu'} C^{jlJ}_{mm_lM} \\ \times D^{j*}_{km}(\alpha\beta\gamma) D^{l*}_{m_l 0}(0,\Theta,\Phi) \\ \times v_{\lambda\mu}(R) D^{\lambda *}_{\mu\mu'} D^{\lambda}_{\mu 0}(0,\Theta,\Phi) C^{j'l'J}_{m'm'_lM} D^{j'}_{k'm'} D^{l'}_{m'_l 0}(0,\Theta,\Phi). \end{aligned} \tag{3.15}$$

Then, making use of the relation for the integral of a product of three rotation matrices:

$$\int d\mathbf{\Omega} D^{j*}_{m'm} D^{j_1}_{m'_1 m_1} D^{j_2}_{m'_2 m_2} = \frac{8\pi^2}{2j+1} C^{j_1 j_2 j}_{m'_1 m'_2 m'} C^{j_1 j_2 j}_{m_1 m_2 m}, \tag{3.16}$$

the integrand (omitting all the pre-multiplicative factors in (3.15)) becomes:

$$v_{\lambda\mu}(R) C^{jlJ}_{mm_lM} C^{\lambda j' j}_{\mu k' k} C^{\lambda j' j}_{\mu' m' m} C^{j'l'J}_{m'm'_lM} C^{\lambda l' l}_{\mu m'_l m_l} C^{\lambda l' l}_{000}. \tag{3.17}$$

Retaining the terms:

$$v_{\lambda\mu}(R) C^{\lambda j' j}_{\mu k' k} C^{\lambda l' l}_{000}, \tag{3.18}$$

and re-expressing the summation over four Clebsch-Gordan coefficients:

$$\sum_{mm'} C^{jlJ}_{mm_lM} C^{\lambda j' j}_{\mu' m' m} C^{j'l'J}_{m'm'_lM} C^{\lambda l' l}_{\mu m'_l m_l} \tag{3.19}$$

as a Racah coefficient W using the identity:

$$\sum_{\beta\delta} C^{bdf}_{\beta,\delta,\beta+\delta} C^{edc}_{\gamma-\delta,\delta,\gamma} C^{abe}_{\gamma-\beta-\delta,\beta,\gamma-\delta} C^{afc'}_{\gamma-\beta-\delta,\beta+\delta,\gamma} = \delta_{cc'}[(2e+1)(2f+1)]^{\frac{1}{2}} W(abcd;ef), \tag{3.20}$$

together with the fact that $M = m'_l + m' = m_l + m$, one obtains an expression involving a product of two Clebsch-Gordan coefficients and a Racah coefficient.

Note that the Racah coefficient W is a form of the $6j-$ coefficient, given by :

$$\left\{ \begin{array}{ccc} j' & k_1 & j'' \\ k_2 & j & k \end{array} \right\} = (-1)^{j+k_1+j+k_2} W(j'k_1jk_2; j''k). \tag{3.21}$$

The $3-j$ symbols, which are related to the usual Clebsch-Gordan coefficients by:

$$\left(\begin{array}{ccc} j_1 & j_2 & j_3 \\ m_1 & m_2 & m_3 \end{array} \right) = (-1)^{j_1-j_2-m_3}(2j_3+1)^{-\frac{1}{2}} C^{j_1j_2j_3}_{m_1m_2m_3} \tag{3.22}$$

possess neater symmetry properties.

The potential matrix element in equation (3.9) can then be written, in the basis of coupled total angular momentum eigenfunctions (3.3), as a combination of two $3-j$ symbols and one $6-j$ symbol [18]:

$$\begin{aligned} < JMjkl|V|JMj'k'l' > \; = \; & \sum_{\lambda\mu} v_{\lambda\mu}(R)(-1)^{j+j'+k-J}\left[\frac{(2j+1)(2j'+1)(2l'+1)(2\lambda+1)}{4\pi}\right]^{\frac{1}{2}} \\ & \times \left(\begin{array}{ccc} l & l' & \lambda \\ 0 & 0 & 0 \end{array} \right) \left(\begin{array}{ccc} j & j' & \lambda \\ k & -k' & \mu \end{array} \right) \left\{ \begin{array}{ccc} j' & l' & J \\ l & j & \lambda \end{array} \right\}, \end{aligned} \tag{3.23}$$

where round brackets denote $3-j$ symbols, and curly brackets denote $6-j$ symbols.

For large values of the radial coordinate R, the radial wavefunctions $u^{Jjkl}_{j'k'l'}(R)$ tend asymptotically to the following form:

$$\begin{aligned} u^{Jjkl}_{j'k'l'}(R) \; \rightarrow \; & \delta_{jj'}\delta_{kk'}\delta_{ll'} exp[-i(\kappa_{jk}R - l\pi/2)] - (\kappa_{jk}/\kappa_{j'k'})^{\frac{1}{2}} < jkl|S^J|j'k'l' > \\ & \times exp[i\kappa_{j'k'}R - l'\pi/2)], \end{aligned} \tag{3.24}$$

where $< jkl|S^J|j'k'l' >$ is an element of the S-matrix. This boundary condition amounts to stipulating that, in the region of large R, the wavefunction consists of only two terms: the incoming plane wave (expanded in spherical waves), and the outgoing spherical wave. The S-matrix is related to the amplitudes of the outgoing waves. The phase-change of the incoming wave is $l\pi/2$, and, since phase is directly related to momentum, the outgoing wave experiences a phase-change of $-l\pi/2$ in order to conserve momentum.

The collision cross-section $\sigma_{jk \leftarrow j'k'}$ itself is proportional to the square modulus of $\mathbf{1} - \mathbf{S}$, averaged over the initial projections m_j and summed over final projections

M:

$$\sigma_{jk\leftarrow j'k'} = \frac{\pi}{(2j+1)\kappa_{j'k'}^2} \sum_{Jll'} (2J+1) |\delta_{jj'}\delta_{kk'}\delta_{ll'} - < jkl|S^J|j'k'l' > |^2. \quad (3.25)$$

In order to obtain cross-sections, we must, in theory, carry out a sum over partial waves of all possible orbital angular momentum, extending to infinite l. In practice, the cross-sections converge after a summation over a finite number of partial waves, owing to the fact that the interaction potential decreases with R, and becomes negligible at some finite R. For the methanol/helium system at collision energies of, say, 500 cm^{-1}, not more than 100 partial waves are necessary to obtain convergence to a tolerance of 1×10^{-4} in the off-diagonal S-matrix elements.

3.2 CS approximation

The full close-coupling (CC) scheme makes use of the space-fixed coordinate system, which does not rotate with the molecule, whereas one decoupling scheme, the so-called CS approximation (Coupled States), is best derived using a special type of body-fixed coordinates known as 'R-helicity' coordinates (see Jacob and Wick [19]).

In the helicity coordinate system (see Figure 3.1), the z-axis lies along the collision coordinate $\mathbf{R}$, the advantage of this being that the projection m_l of the orbital angular momentum on the z-axis is automatically zero. As a result, the equations describing the collision in the helicity frame are independent of l. Also, $l_z = 0$ in the helicity frame. However, since the helicity frame is attached to the rotating molecule, we encounter Coriolis forces, which depend on l^2, so the coupling matrix is no longer diagonal in l^2 as it was in the space-fixed coordinate system.

In order to transform the problem from a space-fixed frame to the helicity frame, it is necessary to rotate the SF wavefunctions into the helicity frame and express the Hamiltonian in helicity coordinates. We start with the SF Hamiltonian written in a generalized operator form:

$$H = H_{st} + \frac{-\hbar^2}{2\mu} {\nabla_R}^2 + V(\mathbf{\Omega}, \mathbf{R}), \quad (3.26)$$

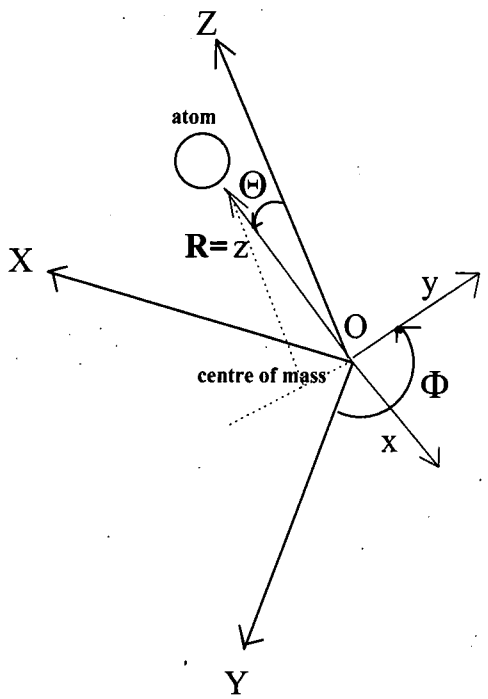

Figure 3.1: Helicity coordinates: The space-fixed frame is (X, Y, Z), and the body-fixed frame is (x, y, z). The z-axis rotates so as to remain parallel with the collision vector $\mathbf{R}$ from the rotor's centre of mass to the colliding atom.

We define a momentum $\mathbf{p_R}$ such that $\frac{-\hbar^2}{2\mu}(\frac{1}{R}\frac{d^2}{dR^2}R - \frac{\mathbf{l}^2}{R^2}) = \frac{-\hbar^2}{2\mu}((-\hbar)^{-2}\mathbf{p_R}^2 - \frac{\mathbf{l}^2}{R^2}) = \frac{-\hbar^2}{2\mu}\nabla_R{}^2$.

We then carry out a transformation from SF frame to helicity coordinates, where the helicity axes are chosen so as to coincide with the spherical polar unit vectors of the position $\mathbf{R}$, i.e [20]:

$$\hat{\mathbf{e}}_x = \hat{\mathbf{e}}_\Theta, \quad \hat{\mathbf{e}}_y = \hat{\mathbf{e}}_\Phi, \quad \hat{\mathbf{e}}_z = \hat{\mathbf{e}}_R.$$

Now, the orbital angular momentum is related to $\mathbf{p}$ by the relation:

$$\begin{aligned} \mathbf{l} &= \mathbf{R} \times \mathbf{p} = (R\hat{\mathbf{e}}_z) \times \mathbf{p}_R \\ &= R\hat{\mathbf{e}}_z \times [(p_R)_x\hat{\mathbf{e}}_x + (p_R)_y\hat{\mathbf{e}}_y + (p_R)_z\hat{\mathbf{e}}_z]. \end{aligned} \tag{3.27}$$

Hence:

$$(p_R)_x = l_y/R, \quad (p_R)_y = -l_x/R, \quad l_z = 0. \tag{3.28}$$

Also,

$$(p_R)_z = p_R. \tag{3.29}$$

Substitution of (3.27), (3.28) and (3.29) into the SF Hamiltonian (3.26) gives, using $\mathbf{l} = \mathbf{J} - \mathbf{j}$:

$$H = (2\mu)^{-1}[-\hbar^2\frac{1}{R}\frac{d^2}{dR^2}R + (J_x - j_x)^2R^{-2} + (J_y - j_y)^2R^{-2}] + H_{st} + V(\mathbf{R}), \tag{3.30}$$

which is entirely equivalent to the SF Hamiltonian, yet it is expressed in terms of operators in the helicity frame.

Recalling that $l_z = 0$ from (3.28), and $J_z = j_z + l_z$, hence $J_z = j_z$, the Hamiltonian (3.30) can be written as [20]:

$$\begin{aligned} H = (2\mu)^{-1}[-\hbar^2\frac{1}{R}\frac{d^2}{dR^2}R + R^{-2}(J^2 + j^2 - 2J_z^2 - (J_x + iJ_y)(j_x - ij_y) \\ -(J_x - iJ_y)(j_x + ij_y))] + H_{st} + V(\mathbf{R}). \end{aligned} \tag{3.31}$$

The combinations $j_x + ij_y$, $j_x - ij_y$, $J_x + iJ_y$ and $J_x - iJ_y$ in (3.31) are the familiar raising and lowering operators:

$$j_\pm = j_x \pm ij_y, \tag{3.32}$$

$$J_\pm = J_x \pm iJ_y, \tag{3.33}$$

so the Hamiltonian, aside from its components which are diagonal in the projection Ω of $\mathbf{J}$ on the helicity frame z- axis aligned along the collision vector $\mathbf{R}$, will also have off-diagonal elements differing from the diagonal by $\Omega^{\pm}1$. The advantage of the helicity frame, however, is that the complicated potential coupling matrix in the SF frame is simplified (the $6-j$ term is removed). Note that Ω, the projection of $\mathbf{J}$ on the helicity frame z-axis, is referred to as the 'helicity', and it can take values from $-J$ to $+J$.

Expressing the SF eigenfunctions as rotations of the helicity frame eigenfunctions in an analogous way to the re-expression of the SF potential, Pack and Hirschfelder [21] obtain:

$$\Psi_{jk}^{JM}(\mathbf{\Omega}, \mathbf{R}) = \sum_{\Omega'=-J}^{J} D_{\Omega' M}^{J}(\mathbf{\Omega}) \psi_{\Omega'}^{Jjk}(\mathbf{R}),$$

where ψ_{Ω}^{Jjk} are the eigenfunctions in the helicity frame, and Ψ_{jk}^{JM} are the corresponding SF eigenfunctions.

If we form the Schrödinger equation using the helicity Hamiltonian and our new rotated eigenfunctions, we obtain the close-coupled equations [20]:

$$H_{\Omega,\Omega-1}\psi_{\Omega-1}^{Jjk} + (H_{\Omega\Omega} - E)\psi_{\Omega}^{Jjk} + H_{\Omega,\Omega+1}\psi_{\Omega+1}^{Jjk} = 0, \tag{3.34}$$

where

$$H_{\Omega\Omega} = (2\mu)^{-1}[-\hbar^2 \frac{1}{R}\frac{d^2}{dR^2}R + \hbar^2[J(J+1) - 2\Omega^2]R^{-2} + j(j+1)R^{-2}] + H_{st} + V(\mathbf{R}) \tag{3.35}$$

and

$$H_{\Omega,\Omega\pm1} = -\hbar\lambda_\pm(J,\Omega)j_\pm/2\mu R^2. \tag{3.36}$$

In order to derive this Hamiltonian, the following relations are needed:

$$J^2 D^J_{\Omega M} = J(J+1)\hbar^2 D^J_{\Omega M} \tag{3.37}$$
$$J_z D^J_{\Omega M} = \Omega\hbar D^J_{\Omega M}$$
$$J_\pm D^J_{\Omega M} = \hbar\lambda_\pm(J,\Omega) D^J_{\Omega\pm 1,M},$$

where

$$\lambda_\pm = [(J(J+1) - \Omega(\Omega^+_-1)]^{1/2}. \tag{3.38}$$

Expanding $\psi^{Jjk}_{\Omega'}(\mathbf{R})$ in the basis:

$$\psi^{Jjk}_{\Omega'}(\mathbf{R}) = \sum_{j''k''} R^{-1} u^{Jjk}_{j''k''\Omega'}(R)|j''k''\Omega' >, \tag{3.39}$$

and multiplying the CC equations in the helicity frame by $(2\mu/\hbar^2)|j'k'\Omega' >$, then integrating over Ω, we obtain the CC equations [20]:

$$h^{j'k'}_{\Omega,'\Omega'-1} u^{Jjk}_{j'k'\Omega'-1} + h^{j'k'}_{\Omega'\Omega'} u^{Jjk}_{j'k'\Omega'} + h^{j'k'}_{\Omega',\Omega'+1} u^{Jjk}_{j'k'\Omega'+1} = \sum_{j''k''} < j'k'\Omega'|V|j''k''\Omega' > u^{Jjk}_{j''k''\Omega'}, \tag{3.40}$$

where:

$$h^{j'k'}_{\Omega'\Omega'} = \frac{d^2}{dR^2} + \kappa^2_{j'k'} - [J(J+1) + j'(j'+1) - 2\Omega'^2]/R^2. \tag{3.41}$$

The procedure of the CS approximation is to neglect the off-diagonal matrix elements in Ω (the so-called 'intermultiplet terms', which arise from the Coriolis forces experienced in the body-fixed frame), and to then further approximate the elements diagonal in Ω^2 by:

$$h^{j'k'}_{\Omega'\Omega'} = \frac{d^2}{dR^2} + \kappa^2_{j'k'} - (l'(l'+1))/R^2. \tag{3.42}$$

Note that the approximation $l' = J$ is made here (though not always), since this value of l' represents an average of all the possible values of l' satisfying the 'triangle inequality':

$$|J - j'| \leq l' \leq J + j'.$$

We then use the fact that $\mathbf{J}^2 = \mathbf{j}'^2 + \mathbf{l}'^2$. That is,

$$J_x{}^2 + J_y{}^2 + J_z{}^2 = j'_x{}^2 + j'_y{}^2 + j'_z{}^2 + l'_x{}^2 + l'_y{}^2 + l'_z{}^2. \tag{3.43}$$

Letting $\mathbf{l}' = \mathbf{J}$ gives:

$$J_x{}^2 + J_y{}^2 + J_z{}^2 = j'_x{}^2 + j'_y{}^2 + j'_z{}^2 + J_x{}^2 + J_y{}^2, \tag{3.44}$$

since $l'_z = 0$. Hence $J_z{}^2 = \mathbf{j}'^2$. Now, the eigenvalue of J_z is Ω', so $\Omega^2 = j'(j'+1)$ if $J = l'$. Therefore,

$$J(J+1) + j'(j'+1) - 2\Omega'^2 = J(J+1) - j'(j'+1). \tag{3.45}$$

However, $\mathbf{j}'^2 = 0$ if $J = l'$, so:

$$J(J+1) + j'(j'+1) - 2\Omega'^2 = l'(l'+1). \tag{3.46}$$

This approximation reduces the CC equations in the body-fixed frame to [20]:

$$\begin{aligned}&[\frac{d^2}{dR^2} - \frac{l'(l'+1)}{R^2} + \kappa^2_{j'k'}]u^{Jjk}_{j'k'\Omega'}(R) \\ &= \sum_{j''k''} < Jj'k'\Omega'|V|Jj''k''\Omega' > u^{Jjk}_{j''k''\Omega'}(R).\end{aligned} \tag{3.47}$$

Forming the matrix elements of this potential in our basis of spherical harmonics and symmetric rotor eigenfunctions, and using the fact that $m_l = 0$ in helicity coordinates, we have:

$$\begin{aligned}< JMjk\Omega|V|JMj'k'\Omega' > &=< JMjk\Omega|\sum_{\lambda\mu} v_{\lambda\mu}(R)Y_{\lambda\mu}(\Theta,\Phi)|JMj'k'\Omega' > \\ &= [(2j+1)/8\pi^2]^{\frac{1}{2}}[(2j'+1)/8\pi^2]^{\frac{1}{2}} \int d\mathbf{\Omega} d\hat{\mathbf{R}} \sum_{\Omega\Omega'\lambda\mu} C^{jlJ}_{\Omega 0 M} \\ \times D^{j*}_{k\Omega}(\alpha\beta\gamma)Y^*_{l0}(\Theta,\Phi)v_{\lambda\mu}(R)Y_{\lambda\mu}(\Theta,\Phi)C^{j'l'J}_{\Omega' 0 M}D^{j'}_{k'\Omega'}(\alpha\beta\gamma)Y_{l'0}(\Theta,\Phi).\end{aligned} \tag{3.48}$$

Using the identity:

$$Y_{\lambda\mu}(\beta\gamma) = (-1)^{\mu}[(2\lambda+1)/(4\pi)]^{\frac{1}{2}}D^{\lambda}_{\mu 0}(\alpha\beta\gamma), \tag{3.49}$$

we have:

$$< JMjk\Omega|V|JMj'k'\Omega' >=< JMjk\Omega|\sum_{\lambda\mu} v_{\lambda\mu}(R)Y_{\lambda\mu}(\Theta,\Phi)|JMj'k'\Omega' > \tag{3.50}$$

$$= [(2l+1)/(4\pi)]^{\frac{1}{2}}(-1)^{\mu}[(2\lambda+1)/(4\pi)]^{\frac{1}{2}}$$
$$\times[(2l'+1)/(4\pi)]^{\frac{1}{2}}[(2j+1)/8\pi^2]^{\frac{1}{2}}[(2j'+1)/8\pi^2]^{\frac{1}{2}}$$
$$\times \int d\mathbf{\Omega} \int d\hat{\mathbf{R}} \sum_{\Omega\Omega'\lambda\mu} C^{jlJ}_{\Omega 0 M}$$
$$\times D^{j*}_{k\Omega}(\alpha\beta\gamma) D^{l*}_{00}(0,\Theta,\Phi) v_{\mu\lambda}(R) D^{\lambda}_{\mu 0}(0,\Theta,\Phi)$$
$$\times C^{j'l'J}_{\Omega' 0 M} D^{j'}_{k'\Omega'}(\alpha\dot{\beta}\gamma) D^{l'}_{00}(0,\Theta,\Phi).$$

From the orthogonality of rotation matrices,

$$\int d\hat{\mathbf{R}} D^{l*}_{00} D^{l'}_{00} = \frac{8\pi^2}{2l+1}\delta_{ll'}. \tag{3.51}$$

Therefore, as we expect in helicity coordinates, the coupling matrix is diagonal in the orbital angular momentum l (i.e. $l = l'$ for non-zero elements). Equation (3.16) yields:

$$\int d\mathbf{\Omega} D^{j*}_{k\Omega} D^{\lambda}_{\mu 0} D^{j'}_{k'\Omega'} = \frac{4\pi}{2j+1} C^{\lambda j' j}_{\mu k' k} C^{\lambda j' j}_{0\Omega\Omega'}. \tag{3.52}$$

Using the identity:

$$\sum_{m_1 m_2} C^{j_1 j_2 j}_{m_1 m_2 m} C^{j_1 j_2 j'}_{m_1 m_2 m'} = \delta_{jj'}\delta_{mm'}, \tag{3.53}$$

the pair of Clebsch-Gordan coefficients in (3.50) can, after rearranging, be eliminated. Using equations (3.51), (3.52) and (3.53), the potential coupling matrix (3.50) reduces to:

$$< JMjk\Omega|V(\mathbf{R})|JMj'k'\Omega' > = \sum_{\lambda\mu} v_{\lambda\mu}(R)(-1)^{-k'-\Omega}\left[\frac{(2j+1)(2j'+1)(2\lambda+1)}{4\pi}\right]^{\frac{1}{2}}$$
$$\times \begin{pmatrix} j & \lambda & j' \\ -k & \mu & k' \end{pmatrix} \begin{pmatrix} j & \lambda & j' \\ -\Omega & 0 & \Omega' \end{pmatrix}, \tag{3.54}$$

after using the symmetry properties of the Clebsch-Gordan coefficients to rearrange the indices in the $3-j$ symbols (see p82-83, Biedenharn and Louck [22]):

$$C^{j_1 j_2 j}_{m_1 m_2 m} = (-1)^{j_1 j_2 - j} C^{j_1 j_2 j}_{-m_1,-m_2,-m'} \tag{3.55}$$

$$C^{j_1 j_2 j}_{m_1 m_2 m} = (-1)^{j_1 j_2 - j} C^{j_2 j_1 j}_{m_2,m_1,m'} \tag{3.56}$$

$$C^{j_1 j_2 j}_{m_1 m_2 m} = (-1)^{j_1 - m_1}[(2j+1)/(2j_2+1)]^{\frac{1}{2}} C^{j_1 j j_2}_{m_1,-m,-m_2} \tag{3.57}$$

$$C^{j_1 j_2 j}_{m_1 m_2 m} = (-1)^{j_2 + m_2}[(2j+1)/(2j_1+1)]^{\frac{1}{2}} C^{j_2 j j_1}_{m_2,m,-m_1}. \tag{3.58}$$

The potential matrix (3.53) vanishes when $\Omega \neq \Omega'$, and so the coupling between different Ω has been removed by the Coupled States approximation. Note also that, from the properties of $3-j$ coefficients, the index μ in the $v_{\lambda\mu}$ expansion of the potential, is:

$$\mu = k - k'. \tag{3.59}$$

Therefore, the index μ in the potential coupling matrix is responsible for coupling different values of k (where asymmetric top functions $|J\tau m>$ are expanded in a basis of symmetric top functions $|Jkm>$, making use of the fact that the symmetric top functions form a complete set in the Euler angles.) Since there is no coupling between different values of Ω, the set of CS coupled equations for the radial wavefunctions may be solved separately for each integral value of Ω between $-J$ and J, thus reducing the computation time.

As with the CC case, the asymptotic form of the radial wavefunctions defines the scattering matrix $< jk\Omega|S^J|j'k'\Omega' >$, and, from this S-matrix, we obtain the CS degeneracy-averaged cross-sections after rotating the S-matrix into the SF frame:

$$\begin{aligned}\sigma(jk \leftarrow j'k') &= \pi\kappa_{jk}^{-2}\sum_{J\Omega}(2J+1) \\ &\quad \times|\delta_{jj'}\delta_{kk'} - < j'k'\Omega'|S^J|jk\Omega > |^2.\end{aligned} \tag{3.60}$$

3.3 IOS approximation

The Infinite-Order Sudden approximation [23] can be viewed as an extension of the idea behind the Coupled States approach (as regards its treatment of matrix elements). In the Coupled States approach, the l^2 matrix element was approximated by an effective eigenvalue form. The assumption behind this is that the relative kinetic energy is sufficiently large for the precise value of l, and hence of the centrifugal potential, to be unimportant. In the IOS approximation, the same procedure is followed for the rotational energy, causing the wavenumber κ_{jk} to be

replaced by the wavenumber κ corresponding to the collision energy E. That is:

$$\kappa_{jk}^2 = E + E_{jk} \tag{3.61}$$

in the CC equations is replaced by

$$\kappa_{jk}^2 = \kappa^2 = E, \tag{3.62}$$

and l is set equal to l':

$$l = l' = L. \tag{3.63}$$

These approximations therefore treat the rotational energy levels as a single degenerate level. Therefore, in the IOS approximation to the CC equations, the quantum numbers j and k disappear, and the distinction between SF and BF frames disappears. The coupled equations become:

$$[\frac{d^2}{dR^2} - \frac{L(L+1)}{R^2} + \kappa^2]u^{JML}(R,\Theta,\Phi) \tag{3.64}$$
$$= \frac{2\mu}{\hbar^2} < JML|V(R,\Theta,\Phi)|JML > u^{JML}(R,\Theta,\Phi),$$

and, in the potential matrix, the position vector $\mathbf{R}$ now enters solely as a parameter. The new radial wavefunctions, too, now depend parametrically on Θ and Φ. The IOS equations are therefore 1-dimensional (in R) for a given (Θ, Φ). One propagates the radial wavefunctions into the region of large R for a given Θ and Φ, then, using the boundary condition:

$$u^{JML}(R,\Theta,\Phi) \rightarrow \kappa^{\frac{1}{2}}[e^{-i(\kappa R - L\pi/2)} - S^{LJ}(\Theta,\Phi)e^{i(\kappa R - L\pi/2)}], \tag{3.65}$$

one determines the angle-dependent S-matrix. If one wishes to obtain approximate state-to-state cross-sections, one encloses the resulting angle-dependent S-matrix between rotational eigenfunctions (bra and ket), and integrates over Θ and Φ by, for instance, Gaussian quadrature on a grid of angular values. A phase factor is included to preserve the same phases as required by the radial asymptotes of the full coupled channel (CC) wavefunctions (see equation (3.24).)

$$S^J_{jklj'k'l'}(E) = i^{l+l'-2L} < JMjkl|S^{LJ}(\Theta,\Phi)|JMj'k'l' > . \tag{3.66}$$

Cross-sections need to be obtained in the lab frame (the SF frame), since this is the frame in which they are observed. The integrations, however, are easier in the BF frame. Fortunately, in the IOS approximation, there is no distinction between the SF and BF frames. Equation (3.25) allows us to obtain approximate state-to-state cross-sections from the S-matrix above.

Chapter 4

Method

Synopsis

First, we describe the details of the method used to generate the energy levels of A-type and E-type methanol in their ground torsional states, for total angular momentum $J \leq 7$. This is followed by the more accurate method used to produce the energy levels of the higher torsional states and an extended basis, with $J \leq 9$, for the ground state.

We then introduce the CH_3OH-He interaction potential used to generate rate coefficients. This consists of two parts: a short-range potential, obtained by Stephen L. Davis, resulting from Many-Body Perturbation Theory calculations to second order, and a long-range potential arising from Van der Waals forces. Finally, we give a description of the MOLSCAT scattering code, which was used to generate cross-sections using the energy levels and interaction potential supplied to it. We describe the propagators used in the approximate solution of the Coupled Channel equations, and details of the various MOLSCAT parameters used to control the collision calculations.

4.1 Calculation of Energy Levels

4.1.1 Initial Method

We recall (see Chapter 2) that methanol is a near symmetric top molecule which possesses an internal degree of freedom associated with torsional motion – that of the methyl radical CH_3 – relative to the rest of the molecule. In the equilibrium geometry, the hydrogen atoms of the methyl radical form the base of a trihedron whose apex is the centre of mass of the molecule, taken to be the origin of the internal ('body fixed') coordinate system. The symmetry (z-) axis is positive in the direction from the base to the apex, and the OH radical is located beyond the centre of mass. The molecule has a symmetry plane, taken to be the xz plane. In the symmetry plane lie the OH radical and the carbon atom, together with one of the three hydrogens of the methyl radical. The equilibrium coordinates of the atoms of which the molecule is comprised are given by Davis and Entley (1992) [24] (see Figure 2.5.)

The characteristics and spectra of symmetric and asymmetric top molecules, with hindered internal rotational (torsional) motion, have been discussed in detail by Townes and Schawlow (1955) [6], Lin and Swalen (1959) [7] and Lees and Baker (1968) [8]. These authors derived explicit expressions for the matrix elements of the Hamiltonian of such molecules; these are given later in this section.

In the limit of a high barrier to torsional motion, the Hamiltonian matrix elements tend to those of a rigid symmetric or asymmetric rotor. However, the case of CH_3OH is one of a barrier of intermediate height, and the asymmetric top energy levels split further into $A-$ and $E-$type stacks, of which the latter is doubly degenerate. Although in A-type methanol the methyl radical has twice the nuclear spin degeneracy as in E-type, the torsional double degeneracy of E-type ensures that both modifications have equal statistical weights (Lees 1973).

We adapted the ASROT (asymmetric rotor) subroutine of the MOLSCAT computer code of Hutson and Green (1995) [25] in order to calculate rotational energy

levels and wave functions for A- and E-type methanol, following the approach which is described in this section. To the diagonal elements of the rotational Hamiltonian we added the terms which arise from the torsional motion, calculated using the internal axis method (Lin and Swalen 1959 [7]). In Tables C.1 and C.2 in Appendix C, we compare the energies which we have computed by this means, of the states which formed the bases of the collision calculations, with the values measured for A- and E-type methanol, respectively. It may be seen that the observed energy level structure is reproduced satisfactorily. Although spectroscopic accuracy is desirable, such high accuracy is not essential in the collision calculations reported below, which involve greater uncertainties – notably in the CH_3OH-He interaction potential.

Lin and Swalen (1959) [7] gave expressions for the matrix elements of the Hamiltonian of an asymmetric top molecule with hindered internal motion, using the Internal Axis Method (IAM). The diagonal elements take the form given in Chapter 2:

$$< kv_t\sigma|H|kv_t\sigma >= \frac{1}{2}(A_a + B_b)[J(J+1) - k^2] + C_cK^2 + E_{Kv_t\sigma}, \qquad (4.1)$$

and, in the limit of a high barrier to internal rotation, the non-zero off-diagonal elements are

$$< kv_t\sigma|H|k+1, v'_t\sigma >= D_{bc}(k + \frac{1}{2})[J(J+1) - k(k+1)]^{\frac{1}{2}}, \qquad (4.2)$$

$$\begin{aligned} < kv_t\sigma|H|k+2, v'_t\sigma > \; &= \; -\frac{1}{4}(A_a - B_b)[J(J+1) - k(k+1)]^{\frac{1}{2}} \\ &\quad \times [J(J+1) - (k+1)(k+2)]^{\frac{1}{2}}. \end{aligned} \qquad (4.3)$$

In these equations, J is the rotational angular momentum, k its projection on the symmetry axis, v_t the quantum number labelling the torsional eigenstate, and σ is defined such that $\sigma = 0$ corresponds to A-type methanol, $\sigma = 1$ to E_1 and σ = -1 to E_2 (E_1 and E_2 are degenerate and are simply referred to as E-type.) D_{bc} is as defined in equation (2.36.)

Pei et al (1988) [26] provide the following values (in cm^{-1}) for the rotational

constants (here the assignment of A, B and C by Pei et al is adapted to our own convention of axes):

$A = 0.793$, $B = 0.823$, $C = 4.257$.

The above expressions for the matrix elements and the values of the rotational constants are mutually consistent, with the yz plane being taken to be the plane of symmetry of the molecule and z to be the symmetry axis. Choosing the xz plane as the plane of symmetry interchanges the numerical values of A and B but also reverses the sign on the right hand side of the equation for $< kv_t|H|k+1, v_t >$, leaving the modulus of the matrix elements unchanged.

Assuming, as in Chapter 2, that the potential to internal rotational motion may be written in the form

$$V(\gamma) = \frac{V_3}{2}(1 - \cos 3\gamma), \tag{4.4}$$

where γ is the internal rotation angle and V_3 is the barrier height, the equation describing the torsional motion ('Mathieu equation') may be written (Lees and Baker 1968 [8])

$$\frac{1}{\alpha}\frac{dM^2}{d\gamma^2} + (R + 2\cos 3\gamma)M = 0, \tag{4.5}$$

where

$$\alpha = V_3/4F, \tag{4.6}$$

$$R = \frac{4}{V_3}(W - \frac{1}{2}V_3), \tag{4.7}$$

and F is the torsional constant, W is the eigenenergy and M denotes the eigenfunction. Pei *et al* (1988) [26] give $F = 27.633$ cm^{-1} and $V_3 = 373.1$ cm^{-1}. The torsional eigenfunction may be written in the form

$$M = (2\pi)^{-\frac{1}{2}}\sum\nolimits_m a_m e^{im\gamma}, \tag{4.8}$$

where $m = 3s + \sigma$, $s =$ any integer. Multiplying the Mathieu equation by $M*$ and integrating over $0 \leq \gamma \leq 2\pi$ yields

$$R = \alpha^{-1}(3s + \sigma)^2 + (1/D_{m+3}) + (1/D_{m-3}), \tag{4.9}$$

where

$$D_{m\pm3} = -a_m/a_{m\pm3}. \tag{4.10}$$

Adding ± 3 to m in the last expression, we obtain a recursion relation of the form

$$D_{m\pm3} = R - \alpha^{-1}(3k + \sigma \pm 3)^2 - D^{-1}_{m\pm6}, \tag{4.11}$$

and R may be written as a continued fraction

$$R = \alpha^{-1}m^2 + 1/(R - \alpha^{-1}(m+3)^2 - D^{-1}_{m+6}) + 1/(R - \alpha^{-1}(m-3)^2 + D^{-1}_{m-6}), \tag{4.12}$$

in which

$$D_{m\pm6} = R - \alpha^{-1}(m \pm 6)^2 - D^{-1}_{m\pm9}. \tag{4.13}$$

A converged value of R is obtained when terms typically up to $D_{m\pm30}$ are included in the continued fraction. Once R has been determined, the eigenvalue (W) may be deduced. This initial approximation considered only states with $v_t = 0$. In the revised method, described in **4.1.2**, torsional states above $v_t = 0$ are introduced.

4.1.2 Revised Method

In the methanol molecule the methyl radical is able to rotate with respect to the OH group, though not freely. The resulting internal 'torsional' motion may be characterized by the relative rotation angle, γ, and the associated quantum number, v_t. We shall be concerned with the ground and the first excited torsional states.

Eigenfunctions $|kv_t\sigma>$ of the torsional Hamiltonian may be written as linear combinations of free rotor basis functions, $|km_t>$, where m_t denotes the torsional angular momentum,

$$|kv_t\sigma> = \sum_{m_t=3s+\sigma} a_{kv_t\sigma m_t}|km_t>, \tag{4.14}$$

and where s is any integer.

The basis functions which are used to construct the eigenfunctions of the torsional Hamiltonian are

$$|km_t> = (2\pi)^{-\frac{1}{2}} e^{(i\rho k\gamma)} e^{(im_t\gamma)}, \tag{4.15}$$

where ρ is defined below in equation (4.20).

There are various equivalent forms of the total Hamiltonian of an asymmetric top with torsion. The particular form adopted here derives from the so-called 'Internal Axis Method' (IAM) introduced by Lin and Swalen (1959) [7]. In this formulation, rotational constants are defined in such a way as to take account of the lack of rigidity of the molecule (i.e. of the torsional motion) and to remove certain couplings between overall and the internal rotation:

$$A_a = \frac{\hbar^2}{2I_{aa}}, \tag{4.16}$$

$$B_b = \frac{\hbar^2}{2} I_{bb}(I_{bb}^2 + I_{bc}^2)^{-1}, \tag{4.17}$$

$$C_c = \frac{\hbar^2}{2}[\frac{I_{bb} + I_{cc}}{I_{bb}I_{cc} - I_{bc}^2} - \frac{I_{bb}}{I_{bb}^2 + I_{bc}^2}], \tag{4.18}$$

$$D_{bc} = \frac{\hbar^2}{2} I_{bc}(I_{bb}^2 + I_{bc}^2)^{-1}, \tag{4.19}$$

where I_{aa}, I_{bb} and I_{cc} are principal moments of inertia, and I_{bc} is a product of inertia; a is the symmetry axis of the molecule.

The dimensionless molecule-specific parameter, ρ , which appears in the torsional eigenfunctions and determines the periodicity of their variation with γ, transforms to:

$$\rho = I_\gamma(I_{bb}^2 + I_{bc}^2)^{\frac{1}{2}}(I_{bb}I_{cc} - I_{bc}^2)^{-1}. \tag{4.20}$$

Defining elements of the overlap matrix as

$$I_{kv_t\sigma}^{k'v_t'\sigma} = < kv_t\sigma | k'v_t'\sigma >, \tag{4.21}$$

where the integrals extend over $0 \leq \gamma \leq 2\pi$, we obtain, for the non-vanishing, off-diagonal matrix elements of the IAM hamiltonian:

$$< kv_t\sigma | H | k+1, v_t'\sigma > \; = \; \frac{1}{2} D_{bc}(2k+1)[J(J+1) - k(k+1)]^{\frac{1}{2}} I_{kv_t\sigma}^{k+1,v'\sigma}$$

$$< kv_t\sigma|H|k+2, v_t'\sigma > = -\frac{1}{4}(A_a - B_b)[J(J+1) - k(k+1)]^{\frac{1}{2}} \times[J(J+1) - (k+1)(k+2)]^{\frac{1}{2}} I_{kv_t\sigma}^{k+2,v_t'\sigma}. \quad (4.22)$$

In our earlier approach [27], the overlap integrals in these equations were set equal to 1, which is their value in the limit of a high barrier to internal rotation. This approximation has now been relaxed, and the overlap integrals are evaluated numerically. For this purpose, we generalized the continued fraction method to $k \neq 0$ by replacing, in the continued fraction, σ by $\sigma - \rho k$. By including the overlap integrals in the off-diagonal elements of the internal hamiltonian, better agreement with the experimental energy levels is obtained for A-type methanol. In particular, the 'drift' of the calculated energies away from their observed values (see Tables in Appendix C), apparent at large values of J and k, is corrected. For E-type methanol, the agreement between the theoretical and observed energy levels was already satisfactory and is not significantly improved. The continued fraction method (see description on page 36, Chapter 2) also yields the contribution $E_{kv_t\sigma}$ of the torsional motion to the diagonal elements of the internal hamiltonian matrix,

$$< kv_t\sigma|H|k, v_t\sigma >= \frac{1}{2}(A_a + B_b)[J(J+1) - k^2] + Ck^2 + E_{kv_t\sigma}. \quad (4.23)$$

The $E_{kv_t\sigma}$ thus obtained have properties which are useful for verifying that the continued fraction algorithm has been applied correctly. The torsional eigenvalues have a sinusoidal variation with k, with a periodicity of $3/\rho$; the minimum of the first cycle occurs at $k = \sigma/\rho$. On the other hand, when the energy exceeds the barrier height, its variation with k becomes parabolic, as expected for free rotation.

Once the torsional eigenvalues and the torsional integrals have been evaluated, the IAM hamiltonian matrix may be diagonalized to yield the rotational eigenfunctions and eigenenergies. The ASROT subroutine in the MOLSCAT program of Hutson and Green (1995) [25] was modified in order to carry out this calculation.

4.2 CH_3OH-He Interaction Potential

4.2.1 MP2 Potential

The potential used in our work was supplied to us by Stephen L. Davis, and is the result of 2^{nd} order Many-Body Perturbation Theory calculations. This theory can be viewed as an extension of the basic Hartree-Fock approach to calculating interaction potentials.

The Hartree-Fock method (Hartree, 1928; Fock, 1930) is based upon consideration of each electron and its interactions with all other electrons and nuclei. The 'exact' quantum mechanical Hamiltonian operator is used to describe explicitly the motion of each electron and its Coulomb interactions with all other charged particles in the system under consideration. While the 'exact' many-electron Hamiltonian operator can be written down, the corresponding exact many-electron wave function is not known. Hartree-Fock theory builds on the simplest possible approximation to such a many-body wave function, namely a product of one-electron wave functions, where each one-electron wave function corresponds to an individual electron (Hartree approach.)

In Hartree-Fock theory, one additional aspect is included in the many-body wave function, namely the Pauli principle (electrons with the same spin cannot occupy the same orbital.) To this end, the product of one-electron wave functions is generalized to a sum of such products with alternating sign (conveniently written in the form of a determinant.) This accounts for the Pauli exclusion principle: electrons with the same spin avoid each other. One could say that each electron is surrounded by a region in space (called the 'exchange hole') which is depleted of electrons with the same spin. Energetically, the exchange hole leads to a reduction in the Coulomb repulsion among electrons with the same spin and thus acts on the electrons as an effectively attractive potential.

Ab initio quantum chemistry methods based on Hartree-Fock theory thus use an exact Hamiltonian and approximate many-electron wave functions, the simplest

of which is a single Slater determinant. More accurate many-electron wave functions such as a series of Slater determinants lead to so-called correlated methods. Quantum chemists often refer to computations using a single Slater determinant as 'calculations at the SCF (Self-Consistent Field) level'. In these calculations, the essential task consists in an iterative self consistency procedure required to solve the Hartree-Fock equations. The Hartree-Fock picture is best suited to small organic molecules and compounds of main group elements which do not contain large numbers of electrons and where the electrons are fairly localized. In other words, the Hartree-Fock picture seems to be adequate as long as the 'individual character' of electrons is reasonably maintained.

Many-Body Perturbation Theory (MBPT) is a method of accounting for electron correlation by treating this effect as a perturbation on the Hartree-Fock wave function. It is a rather straightforward application of simple perturbation theory. Usually, one computes corrections to the energy using second-order perturbation theory, which is abbreviated MBPT(2). This is usually also called second-order Møller-Plesset perturbation theory, or MP2. The results are usually better than those obtained using the Hartree-Fock approach.

In principle, one could proceed to higher orders of perturbation theory (MP3, MP4, etc), but the computer programs become difficult to write, and the results (perhaps surprisingly) do not necessarily improve at these higher orders.

When MP2 calculations are carried out for the methanol/helium system, the energy of interaction between a (ground state) helium atom and a methanol molecule, with its constituent atoms assumed fixed at their equilibrium positions, may be expanded in the following form:

$$V(R,\theta,\phi,\gamma) = (2\pi)^{-\frac{1}{2}} \sum_{lmn} v_{lmn}(R) Y_{lm}(\theta,\phi) e^{in\gamma}, \tag{4.24}$$

where (R,θ,ϕ) are the spherical polar coordinates of the helium atom relative to a molecule-fixed coordinate system in which z points along the symmetry axis, from the methyl radical to the centre of mass of the molecule; the xz plane is the symmetry plane of the molecule. The coordinate origin is located at the centre of mass, with all the atoms assumed to occupy their equilibrium positions (see

Davis and Entley 1992 [24]). $0 \leq \gamma \leq 2\pi$ is the internal rotation angle of the CH_3 radical. The Y_{lm} are normalised spherical harmonics. The potential possesses threefold symmetry about the $z-$ axis, and n is a multiple of 3.

The coefficients v_{lmn} in this, the short-range part of the potential, were calculated on a grid of 11 values of R between 4 and 12 bohr (see *Appendix E*). Their radial variation was fitted with cubic splines, and the γ dependence was removed by averaging over the ground and first excited state torsional eigenfunctions [27].

The long-range part of the interaction potential, comprising induction and dispersion terms, must also be specified. This potential has the form:

$$V(R,\theta,\phi) = \sum_{Nlm} R^{-N} D_{Nlm} Y_{lm}(\theta,\phi). \tag{4.25}$$

The coefficients D_{Nlm} were obtained from the values of the multipole moments and polarizabilities for the staggered conformation, $\gamma = 0$, of methanol (Davis and Dennison 1994 [12]).

The barrier to internal rotation of the methyl group is 373 cm^{-1} (1 cm^{-1} = 1.4388 K). This barrier is large compared with the kinetic temperatures ($T \leq 20$ K) considered in the bulk of this work. Accordingly, we have considered initially the following two cases:

i. MP2 'Staggered Conformation': The methyl radical is fixed internally, i.e. the internal rotation angle γ = constant ('staggered conformation'). In practice, we take $\gamma = 0$, corresponding to the minimum internal energy configuration; this potential being denoted:

$$V^{stg}(R,\theta,\phi) = \sum_{lm} v_{lm}^{stg}(R) Y_{lm}(\theta,\phi), \tag{4.26}$$

where

$$v_{lm}^{stg}(R) = (2\pi)^{-\frac{1}{2}} \sum_{n} v_{lmn}(R). \tag{4.27}$$

ii. MP2 Torsionally Averaged Potential: The interaction potential is 'torsionally averaged' over the internal rotational eigenfunction,

$$\psi_{Kv_t}(\gamma) = (2\pi)^{-\frac{1}{2}} \sum_{n} a_{Kv_tn} e^{in\gamma}, \tag{4.28}$$

yielding

$$V^{tor} = \sum_{lm} v_{lm}^{tor}(R) Y_{lm}(\theta, \phi), \tag{4.29}$$

where

$$v_{lm}^{tor}(R) = (2\pi)^{-\frac{1}{2}} \sum_n v_{lmn}(R) S_{Kv_t n}, \tag{4.30}$$

and

$$S_{Kv_t n} = \sum_{n'} a_{Kv_t n'} a_{Kv_t, n'+n}. \tag{4.31}$$

4.2.2 Long-Range Potential

The total interaction potential of the CH_3OH/He system has a repulsive part and, in addition, an attractive part arising from Van der Waals forces. The attractive part dominates at long range, and *vice versa*. The long-range behaviour can in turn be separated into a sum of induction and dispersion effects due to small induced dipole (and higher) moments in the electron cloud distributions caused by the proximity of the two colliding species. The repulsive part of the potential, supplied by Davis, was therefore supplemented by an attractive part generated from tensor components of the dipole moment. Whereas it is necessary to interpolate and extrapolate the repulsive part, the attractive part is essentially exact (for our purposes), and can be extended out to any distance.

Both the induction and dispersion contributions to the attractive potential are obtained using perturbation theory. The attractive part, as with the repulsive part, is expanded in spherical harmonics, and this is done separately for the induction and dispersion terms. The inverse power dependence (on radial distance) of these terms is brought out as an explicit radial dependence:

$$V(R, \theta, \phi) = \sum_{nlm} D_{nlm} Y_{lm}(\theta, \phi) R^{-n} \tag{4.32}$$

where the D_{nlm} coefficients are different for induction and dispersion. These coefficients are obtained [24] using expressions in terms of multipole moments and polarisability tensors, as listed in [24]. See Appendix D.

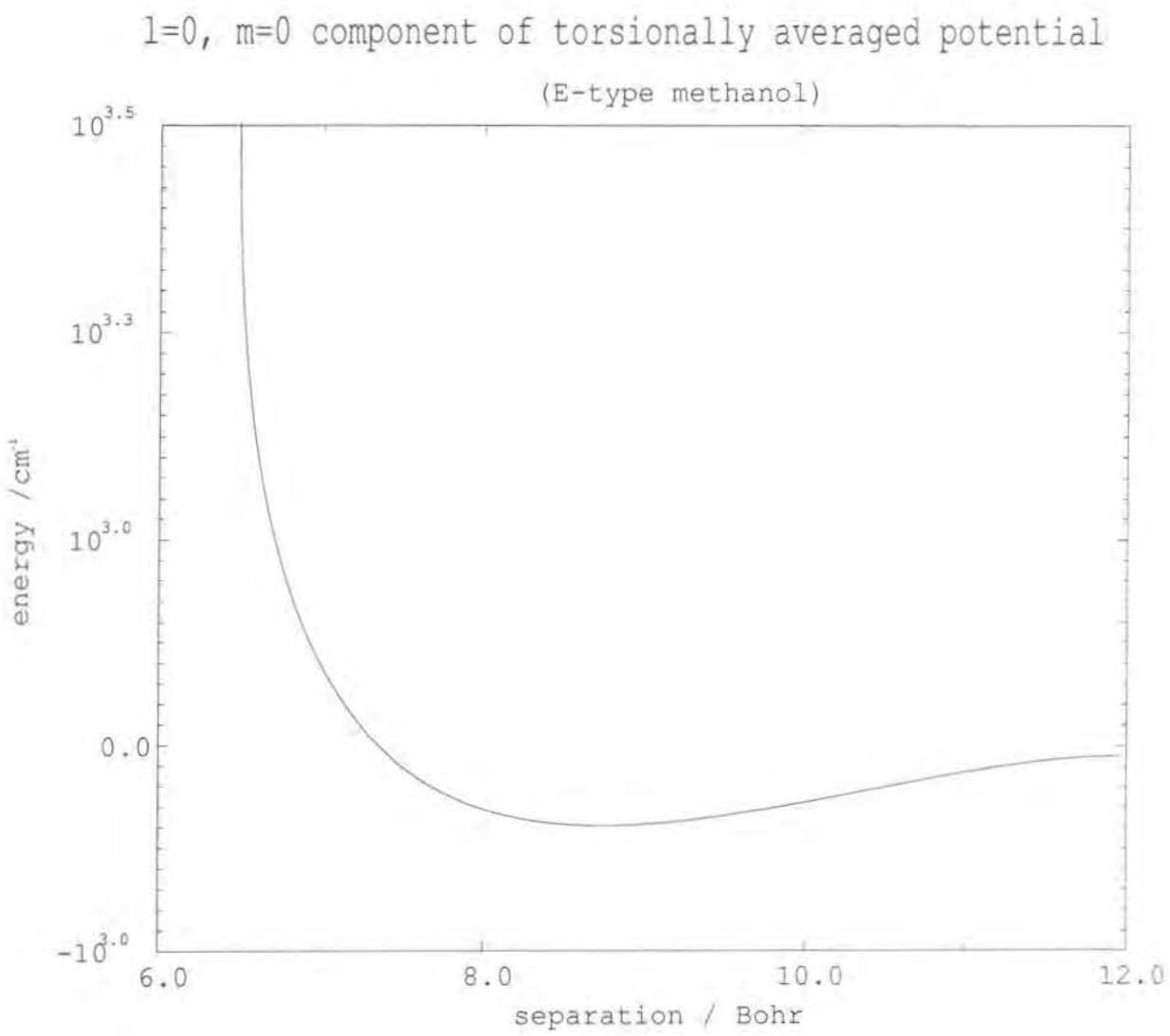

Figure 4.1: Isotropic l=0, m=0 component of total potential

Figure 4.1 gives an example of the complete potential (in this case, the $l = 0$, $m = 0$ isotropic component) obtained by adding the long- and short-range potentials. Note the presence of a potential well.

4.3 MOLSCAT Collision Code

4.3.1 General description of MOLSCAT

The collision calculations were performed using MOLSCAT, a multi-purpose code for integrating the coupled channel (CC), coupled states (CS) and infinite order sudden (IOS) equations, to yield state-to-state collision cross-sections. MOLSCAT was written by Hutson and Green [25], the version used here being Version 14. The code has various modes for handling, for example, symmetric tops, asymmetric tops, diatomic molecules and surface-scattering. I used it exclusively in 'asymmetric top/structureless atom' mode.

MOLSCAT calculates the outcome of nonreactive collisions of a molecule with an atom or with another molecule. A typical application is the calculation of state-to-state cross sections or rate constants for rotational (and possibly vibrational) excitation of the colliding species. MOLSCAT solves the time-independent Schrödinger equation to obtain a wavefunction for the whole system. The wavefunction is expanded as a sum of products of the (asymptotic) rotational and/or vibrational wavefunctions of the two colliding species, a partial wave (spherical harmonic) expansion of the angle dependence of the collision coordinate (relative position of the two species), and functions of the radial collision distance. The latter are determined by solving coupled second-order differential equations (see equation 3.9). The coupling between these equations arises from the angle (and vibrational) dependence of the forces between the two species, i.e., the forces which cause rotational and vibrational excitation. Information concerning the outcome of the collisions is contained in the behaviour of the wavefunction in the region of large radial coordinate, and this is conveniently summarized in terms of collisional S-matrices.

One problem with this method is that the colliding species have an infinite set of rotational states, and it is necessary to truncate the expansion of the total wavefunction to some finite number of states. In general, the wavefunction can be

made to converge by including sufficiently high-energy basis functions. Convergence (to some given tolerance) is usually attained when one has included all the levels which are energetically accessible at the collision energy of interest (open channels) plus some energetically inaccessible levels (closed channels). Convergence is slower for more anisotropic interaction forces and for strongly attractive interactions. Note that S-matrix elements are only defined between open channels.

This approach, which is exact in every respect, except for the truncation of the basis set, is computationally feasible only for systems which have a rather small number of rotational and vibrational levels accessible at the collision energies of interest. By introducing certain approximations to the coupling terms (as described in Chapter 3) it is possible to decouple the problem into smaller blocks and MOLSCAT is equipped to do this for several decoupling schemes. Of these, the coupled states approximation has been found to be reasonably accurate, especially for systems dominated by short-range forces and at higher collision energies. The infinite order sudden (IOS) approximation has been found to be useful in cases where the rotational energy spacings are small compared with the collision energy.

4.3.2 MOLSCAT input data

For each calculation it is necessary to provide the program with information about the rotational and/or vibrational wavefunctions which should be included and to specify the intermolecular forces as a function of collision distance and relative orientations. The type of basis functions and the coordinate system needed to describe the interaction potential depend on the kinds of colliding species. Several possible combinations are supported by MOLSCAT. The collision types are described by an internal variable ITYPE. The parameter of ITYPE used was ITYPE = 6 (collision of an asymmetric top rigid rotor with a structureless atom.)

Besides expansion basis functions and an interaction potential, it is also necessary to provide input data which specify the collision energies, the method to use for integrating the coupled equations, approximate coupling scheme (CS and IOS

approximations), optional processing, etc.

In MOLSCAT, the input data are divided into three sets of NAMELIST input. NAMELIST input is not standard FORTRAN, but it is implemented on most platforms. In general it consists of data cards of the form, &<name> data1=value1, data2=value2, ... &END where <name> is the name associated with the input set; data1, data2, etc. are names of allowed variables in that set; and &END specifies the end of data for this set. The three sets of required data are &INPUT, &BASIS, and &POTL. The section &INPUT contains variables for control of the calculations, and &BASIS and &POTL describe the expansion basis set and interaction potential respectively.

4.3.3 Integrator Methods for Solving the Coupled Channel Equations

Let $\mathbf{F}(R)$ be the expansion coefficients in the eigenvectors. These are our solutions. One obtains numerically the matrix of solutions $\mathbf{F}(R)$ by outward propagation. This propagation is begun at a value of the interparticle distance $R = R_{start}$ which lies well inside the innermost classical turning point. When $\mathbf{F}(R)$ has been propagated out to a large value of R such that the potential $\mathbf{V}(R)$ is negligible, compared to the wavevector term κ^2, the solutions $\mathbf{F}(R)$ can then be matched to the known asymptotic form to obtain the S matrix. This procedure is repeated at all values of the total angular momentum J_{tot} considered. In a semiclassical description, the total angular momentum corresponds to the impact parameter b. From the S matrix at all these values of J_{tot}, one can calculate differential and integral cross sections [28] [29].

Many algorithms have been developed to solve these equations. These algorithms can be grouped into two categories [30]:

1. Solution-following methods.

In these methods, one approximates the matrix of solutions $\mathbf{F}(R)$ by a power series and then solves the coupled channel equations exactly. This is similar in spirit

to the usual numerical techniques for solution of ordinary differential equations (Runge-Kutta, Euler, etc...)

2. Potential-following methods. In these methods, the matrix $\mathbf{V}(R)$ is approximated by a sequence of constant or linear segments. In these local regions the approximated CC equations can be solved exactly.

In solution-following methods the solution is approximated while the potential is retained exactly. On the other hand, in potential-following methods the potential is approximated but the solution (to this approximate potential) is exact.

No single method is ideal at all values of the internuclear separation. It is advisable to combine a solution-following method at short-range (R small), where most intermolecular potentials vary rapidly, with a potential-following method at longer range, where the potential varies more slowly but where for many problems the solution can be highly oscillatory. This combination of two methods is called a hybrid integrator.

The particular hybrid integrator selected from the options available was the log-derivative/Airy propagator, being the recommended propagator for the generation of cross-sections by MOLSCAT. In this case, the solution-following method used at short range is based on the log-derivative propagator of Johnson [31] [32], as modified by Manolopoulos [33]. This propagator is designated LOGD. The potential-following method used at long-range is based on the linear-reference potential of Gordon [30] [34] , as modified by Alexander and Manolopoulos [35] [36]. This propagator is designated AIRY. The log-derivative/Airy propagator combines these two fast algorithms (LOGD and AIRY). Both are fast and exceptionally stable. To a large degree the numerical stability is obtained by propagation of the logarithmic derivative of the solution matrix $\mathbf{F}(R)$, namely

$$\mathbf{Y}(\mathbf{R}) = \frac{d\mathbf{F}(R)}{dR}\mathbf{F}(R)^{-1}, \tag{4.33}$$

rather than the solution matrix itself.

4.3.4 Control of propagators in MOLSCAT

Convergence of coupled channel calculations with respect to integration range and step size is very important; lack of convergence can give very poor results, whereas unnecessarily conservative tolerances can waste large amounts of computer time.

Parameters common to all propagators

1. Range of integration

The mechanisms used to choose the starting and finishing points for integrating the coupled equations are the same for all propagators available within MOLSCAT. In the simplest case, the input variables RMIN (default 0.8) and RMAX (default 10.0) are supplied and used exactly as input. (Note that the default values are appropriate when RM is approximately the distance of the potential minimum.) However, in certain circumstances RMIN and RMAX are modified from their input values:

- If IRMSET > 0 on input (default 9), the program will estimate a suitable distance to start propagating, using the criterion that the wavefunction amplitude in all channels should be less than $10^{-IRMSET}$ at the starting point. A crude semiclassical estimate of the wavefunction is used to make this estimate, which is calculated separately for each total angular momentum JTOT and its projection M (at the first energy only.)

- If there is a centrifugal barrier present, the program checks that all open channels are classically accessible at the RMAX requested, for all energies in the ENERGY list. If necessary, RMAX is increased to the value of R at the furthest classical turning point found in the centrifugal potential for any energy. However, RMAX is never decreased from the input value. For RMAX we chose 15.0 Bohr radii, and 2.0 for RMIN.

Thus, the input value of RMAX is the smallest distance at which the propagator may terminate.

Propagating out to the centrifugal turning point is not necessarily adequate, particularly when calculating elastic integral cross sections. It is also important to

note that a value of RMAX which is adequate for low JTOT may not be adequate for high JTOT, and that calculations using too small a value of RMAX may appear to be converged with respect to the partial wave sum when they are not actually converged.

2. Step size

The basic log-derivative propagator is a wavefunction-following method, and uses a constant step size controlled by the parameter STEPS (default 10.0.) This is interpreted as the number of steps per half-wavelength for the open channel of highest kinetic energy in the asymptotic region. A value between 10 and 20 is usually adequate, unless the depth of the potential well is large compared to the scattering energy. The two modified log-derivative propagators are actually potential-following methods, but they nevertheless use the same mechanism (STEPS) to determine step size, for compatibility with the basic log-derivative code. For these propagators, values of STEPS around 5.0 are usually adequate.

For potential-following methods, the de Broglie wavelength is less important. Instead, the required initial step size is input explicitly in the variable DR (default 0.02.) However, in both propagators the step size may subsequently be modified, as described below for the Airy propagator.

4.3.5 Log-derivative propagators

These propagators are selected in the &INPUT list by setting the variable INTFLG to INTFLG = 5, 6 or 7. INTFLG=6 specifies the 'diabatic modified log-derivative method' of Manolopoulos. This is a very efficient and stable method, especially at short range. INTFLG = 6 automatically detects single- channel cases (including IOS cases) and uses a more efficient implementation of the propagator.

The only relevant input variables for these propagators are RMIN, RMAX and STEPS as described above.

4.3.6 Hybrid log-derivative/Airy propagator

This propagator is selected by setting the INTFLG to INTFLG = 8. The hybrid modified log-derivative Airy propagator of Manolopoulos and Alexander uses the same method as INTFLG = 6 at short range, but changes to the Airy propagator at long range. This is the recommended general-purpose propagator for cross section calculations.

The modified log-derivative (INTFLG = 6) propagator is used from RMIN to RMID. In general, values of RMID somewhat beyond the distance of the minimum are recommended. We took RMID=12.0 Bohr. The step size for this propagator is controlled by STEPS, which was set to 20.

The Airy propagator is used to propagate from RMID to RMAX. If RMID is greater than RMAX this propagator is not called. By default the initial step size is taken as the value calculated for the modified log-derivative part, but it can be further controlled by the following variables (DRAIRY, TOLHI and POWRX):

DRAIRY

This is the DR variable for the AIRY propagator. The default value is -1.0. This variable can be used to specify an absolute step size. If DRAIRY is less than zero, the initial step size is taken from the log-derivative propagator. The default value was used.

TOLHI

If less than 1, the propagator uses this as a tolerance to adjust the step size (by a perturbation method) to try to maintain this accuracy. If greater than 1, the step size is increased by this factor in each interval. Values around 1.03 to 1.07 are generally useful. The Airy propagator accumulates perturbation corrections to the wavefunction as it propagates, and uses these to obtain a suitable length for the next interval. The input parameter DR described above is used as the size of the first interval, and subsequent interval lengths are obtained using the input tolerance TOLHI (default 0.001); the criterion is that some function of the perturbation corrections should be not greater than TOLHI over any interval. Within an interval, this function is checked against TOLHI at each step, and a new interval is started

(with a new diagonalising transformation) if it appears likely to exceed TOLHI over the next step. For TOLHI we adopted the default value. Therefore, the step size is automatically adjusted.

POWRX

If TOLHI is less than 1, this is the inverse power used in estimating the step size from perturbation calculations. The default value of 3 was found to be adequate.

4.3.7 Example of NAMELIST input file

The following input is an example of a calculation which converged satisfactorily to an off-diagonal tolerance of 1×10^{-5} and a diagonal tolerance of 0.3 in the S-matrix elements.

&INPUT
LABEL=' ITYPE=6, CH3OH/HE INTERACTION',
URED=3.558,
NNRG=1,ENERGY=750,
RMIN=2.000, RMAX=15.00, ISCRU=0,
INTFLG=8, STEPS=20,
RMID=12.000,
PRNTLV=1, LMAX=6, ISIGU=0, ISIGPR=1,
MMAX=6, IRMSET=8,
LASTIN=0,
&END
&BASIS
ITYPE=26,
A=0.815, B=0.785, C=4.257323,
JMIN=0, JMAX=9, JSTEP=1,
&END
&POTL
EPSIL=1.000, RM=0.529177, MXLAM=28, NPOTL=28, CFLAG=0,

LAMMAX=6,

IPRINT=3,

&END

Chapter 5

Results: cross-sections and rate coefficients

Synopsis

In this chapter we present the results of the cross-section calculations described in Chapter 4, and the rate coefficients obtained from them, these being discussed in an experimental/astrophysical context.

Empirical rate-coefficients for methanol/H_2 and methanol/He have already been obtained by Lees and Haque (1974) [1], on the basis of microwave double resonance experiments under laboratory conditions. Though performed at room temperature, these experiments are thought to be at least a guide to the collisional behaviour of the methanol/He system at low interstellar temperatures. It is therefore useful to compare our results with those of Lees and Haque [1].

First we summarise the experiments performed by Lees and Haque [1], together with their conclusions. Next, we describe the collision calculations in general, and present the rate coefficients calculated at a temperature comparable to that of the Lees and Haque experiments. Then we summarise the different rate coefficient results obtained from cross-sections calculated under the assumption of a high barrier to internal rotation (for $A0$ and $E0$, that is, the ground torsional states of A- and E-type methanol), and the corresponding results for the 'intermediate barrier'

treatment of the rotational energy levels (for $A0$, $E0$, $A1$ and $E1$.) The effect of the different types of MP2 potential used ('torsionally averaged' and 'staggered' (see Equations (26) and (29), Chapter 4)) on the rate coefficients is also investigated.

Finally, we present an investigation of the cross-section vs. energy curves, carried out with the intention of making sure that incomplete sampling of the resonance structures at low energies, owing to the coarseness of the collision energy grid, does not significantly affect the determination of rate coefficients.

5.1 Description of microwave double resonance experiments of Lees and Haque [1]

Double resonance is a phenomenon that can be exploited to preferentially select, from a spectrum, only the transitions one is interested in. The experimental arrangement is usually some variant of the pump-probe, where one beam (optical, infra-red, or microwave) is used to perturb the sample away from equilibrium, and another, possibly very weak beam is used to probe the spectrum of the perturbed sample. Typically, the probe is locked on a known transition and the frequency of the pump beam is scanned, but other variations are possible. At low pressure, only if the pump starts at either of the known lower or upper states of the probe transition will one detect a double resonance signal. Transitions from the many other levels which may lie in the same spectroscopic region will not produce a double resonance signal and thus one obtains tremendous simplification. By moving the probe to a different assigned transition, one can map out the complete spectrum.

In a paper by Lees and Haque (1974) [1], the technique of double resonance spectroscopy was used to characterize room-temperature collisionally-induced energy transfer processes in E-type methanol, with He and H_2 as the perturbing species. In these experiments, a klystron was used to generate the required microwave pump field, which excites methanol molecules that have a narrow distribution of velocities in the direction of the beam from the lower to the high pump level. A second tunable 'probe' klystron was used to record a double resonance

Figure 5.1: Typical four level systems in CH_3OH. The pumped microwave transitions are indicated by bold arrows, and the signal transitions by thin arrows. The dotted and dashed arrows indicate various collision induced transitions. α denotes $\Delta K = 0$ transitions, β denotes $|\Delta K| = 1$, and ζ denotes $|\Delta J| = 1$, $|\Delta K| = 1$. The transitions which feed into these four-level systems from outside are lumped together as η. (Figure adapted from Lees and Haque [10.])

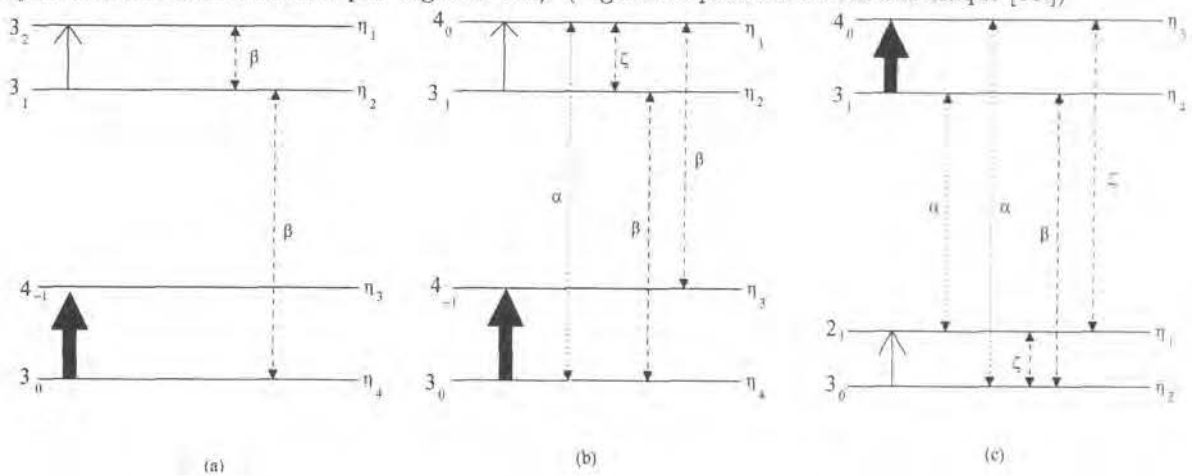

signal from the desired probe levels. The lineshape of the signal transition consists of a narrow component ('transferred spike') that results from collisionally-induced rotational transitions, and a broad component (with a larger distribution of frequencies) due to molecules with velocities such that their lines are Doppler-shifted, and are therefore off-resonance with respect to the pump.

When double resonance occurs, the intensity of the probe beam is enhanced (giving the signal beam) when the double resonance specific to the tuning of the pump beam is encountered. All other transitions are 'ignored' by the setup.

Three four-level double resonance systems (see Figure 5.1) were studied by Lees and Haque, the resulting ratios (on- and off-resonance) of the signal intensity for the three systems being used to deduce the amount of collisional transfer between the probe levels and the signal levels. In all three cases, the probe and signal levels were not linked directly (i.e. neither the upper or lower probe levels were identical to one of the signal levels), but instead linked indirectly via certain collisional processes involving a change $|\Delta K|$ in the magnitude of the body-fixed projection of the total angular momentum. Any double resonance effects observed were thus due only to collisional transfer between the pump and probe/signal levels.

For example, pumping the pump levels shown in Figure 5.1 (thick arrows) results in depopulation of the lower pump level. This depopulation is transferred to the lower probe/signal level, in case (a), via the collisional process β, which involves a change of rotational state $|\Delta K = 1|$. This causes a fractional change in intensity $\Delta I/I$ of the probe beam, which is tuned to the frequency of the probe/signal transition.

The relative probe/signal intensities for these double resonance systems provide information about the rate of collisional transfer to and from the pump and probe/signal levels, and it is possible to deduce the relative rate coefficients for transitions with given $|\Delta K|$.

The conclusions of Lees and Haque are that, for collisions of CH_3OH with either He or H_2, the collisional transition rates decrease as $1/\Delta J$. In the collisions with He, parallel $\Delta K = 0$ collisional transitions occur about four times more frequently than perpendicular $\Delta K = 1$ transitions, whereas in collisions with normal H_2, $\Delta K = 0$ transitions are approximately twice as frequent as $\Delta K = 1$ transitions. These patterns are referred to as 'propensities', and are related to dipole selection rules.

5.2 Cross-section calculations

For the collision cross-section calculations (see Chapter 4 for method), we used the MP2 potential with both the smaller rotational basis obtained under the 'high barrier' approximation (extending from $J = 0$ to $J = 7$) and with the larger basis obtained under the 'intermediate barrier' treatment (extending from $J = 0$ to $J = 9$.) The latter allows us to calculate cross-sections for within a given torsionally excited state, whereas the 'high barrier' calculations are only sufficiently accurate for the ground torsional states $A0$ and $E0$. The torsionally excited states are not modelled well by a high barrier, because these states occur at high collision energies, where the 'high barrier' approximation is less valid. Unless it is stated otherwise,

final level	initial level	CS σ / $\mathring{A}^2$	CC σ / $\mathring{A}^2$
1	1	1.155393×10^{2}	1.232686×10^{2}
2	1	9.120967×10^{0}	9.252671×10^{0}
3	1	1.908441×10^{0}	2.090640×10^{0}
5	1	1.185616×10^{1}	1.214758×10^{1}
6	1	2.288126×10^{-1}	2.519281×10^{-1}
9	1	1.143730×10^{0}	1.429466×10^{0}
10	1	4.570009×10^{0}	3.868918×10^{0}
11	1	6.525939×10^{-1}	7.627295×10^{-1}

Table 5.1: Comparison of selected cross-sections obtained using CC and CS approaches at collision energy of 100 cm^{-1}. Level numbers are in MOLSCAT order.

the results we discuss are, implicitly, those obtained using the full 'intermediate barrier' treatment.

The results presented here were obtained with the CS (Coupled States) approximation. We ran, for a high barrier, the same calculation, at high and low energies, using the CC (Coupled Channels) equations and the less time-consuming CS approximation to these. The results were found to differ by no more than 20 percent, and their qualitative behaviour was the same. Therefore, we exclusively used the CS approximation in the subsequent calculations. See Table 5.1 for a short section of the results of this comparison. A similar comparison between the CS and CC approximations was carried out with our very early calculations with an SCF (Self-Consistent Field) potential. The method and results of these calculations are given in Appendix B. These results compare favourably with the IOS results (at 500 cm^{-1}) of Davis and Entley [11].

The calculations were used to map the variation of the cross-sections with collision energy.

The final grid upon which the energy-variation of the cross-sections was obtained extended from 1 cm^{-1} to 1300 cm^{-1}, with a fine spacing of 0.5 cm^{-1} below 20 cm^{-1}, and a steadily increasing spacing above 20 cm^{-1}. This grid therefore has a good coverage of low-energy and high-energy structure.

Figure 5.2: Number of partial waves l necessary for convergence of S-matrix elements to maximum error in diagonal elements of 7.6×10^{-2} and maximum error in off-diagonal elements of 1.6×10^{-4}.

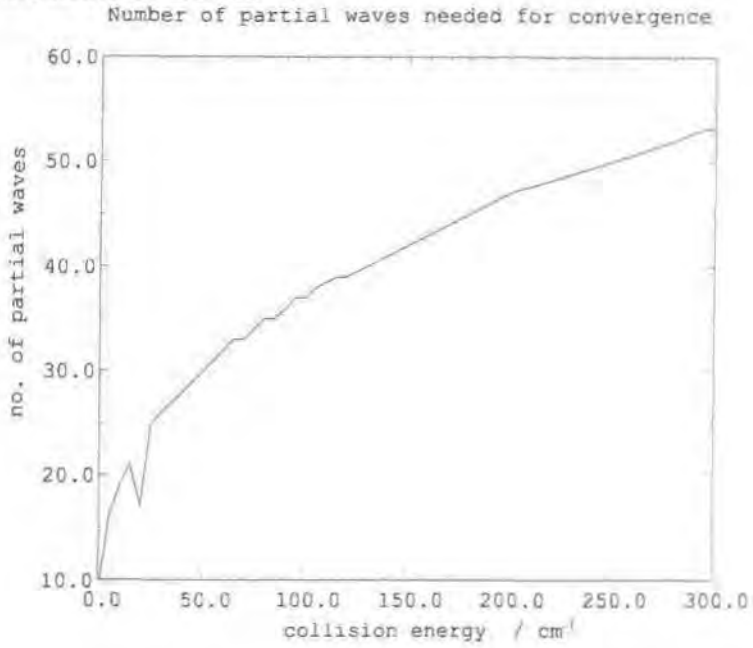

However, before this grid was used, the collision energy grid for the ground torsional states $A0$ and $E0$ extended from E_{CM}=5 cm^{-1} to E_{CM}=300 cm^{-1}, in steps of 5 cm^{-1}, expressed relative to the lowest rotational levels of A-type methanol, with an additional point at E_{CM}=1 cm^{-1} (so that, for the lowest transitions in A-type methanol, at least one data point is close to the lowest thresholds, which are close to 1 cm^{-1}.) For the 'high barrier' results, this same grid extended to E_{CM}=200 cm^{-1}. The smaller basis gives rise to a maximum of 344 coupled states for both A-type and E-type methanol (since the basis set for both extends from $J = 0$ to $J = 7$.) Similarly, the larger basis gives rise to a maximum of 670 coupled states.

At each collision energy, the partial wave calculations were carried to sufficiently high values of the total angular momentum to ensure convergence of the elastic and inelastic cross-sections. Figure 5.2 shows the number of partial waves it is necessary to include in order to obtain convergence of the S-matrix elements to within 7.6×10^{-2} for the diagonal elements and 1.6×10^{-4} for the off-diagonal elements. From this plot, it is apparent that, as the collision energy is increased,

the number of partial waves required for the specified convergence increases.

In figure 5.12, we plot, as an example, the energy dependence of the cross-section for the transition J, K=1, $0A \rightarrow J$, K=0, $0A$. This is the basic shape of all the cross-section versus energy curves one obtains with the methanol/He system: a threshold, followed by a low-energy portion exhibiting some resonance structures, with the cross-section decreasing towards to a high-energy region in which little structure is found to be present. The bulk of the resonances occur below 50 cm^{-1}, and, since these resonances can require a fine energy grid for their resolution, and our grid is coarse compared with the required grid at these low energies, the effect of resonances on our determination of rate coefficients is assessed in section 5.4.

5.3 Rate coefficient calculations

5.3.1 Calculation procedure

Rate coefficients are a measure of the average rate at which a given transition is collisionally induced to occur when the system is under the conditions of a Maxwellian distribution of collision energies at a given temperature T. Thermal rate coefficients were calculated at both high and low temperatures, using the cross-section data. The low-temperature (20 K) rate coefficients enabled the prediction of possible line intensity ratios which are sensitive to the density of the perturber and which lend themselves to the determination of the perturber densities in the dark molecular clouds of the interstellar medium (see Chapter 6.)

The following subsections discuss the rate coefficients we obtained using the 'high barrier' approximation and the 'intermediate barrier' treatment. The calculations of rate coefficients were carried out with the intention of answering such questions as: How do our theoretical rate coefficients compare with the experimental results of Lees and Haque (discussed in section 5.1)? What effect does the method of calculating the energy levels of methanol have upon the rate coefficients? How does the introduction of torsion modify the behaviour of the rate coefficients

for $A0$ and $E0$? How do the results for the 'staggered' and 'torsionally averaged' potentials (see equations (4.26) and (4.29)) compare? What is the temperature dependence of the rate coefficients?

Thermally averaged rate coefficients are related to the cross-sections by:

$$q_{j\to i}(T) = \left(\frac{8kT}{\pi m}\right)^{\frac{1}{2}} \int_0^\infty Q_{j\to i}(x_j kT) x_j e^{-x_j} dx_j, \tag{5.1}$$

where $x_j = E_j/kT$; E_j is the collision energy, relative to the initial state j of the $j \to i$ transition, $Q_{j\to i}(E_j)$ is the energy dependent cross section, T is the kinetic temperature, and m is the reduced mass of the CH_3OH-He pair. Equation (5.1) was evaluated for all transitions which involve de-excitation of the methanol; rate coefficients for excitation were obtained from detailed balance,

$$q_{j\to i}(T) = \omega_i q_{i\to j}(T) exp[-(E_j - E_i)/kT], \tag{5.2}$$

where $\omega = (2J + 1)$ is a statistical weight.

The integral in equation (5.1) was evaluated by means of a trapezoidal rule on a fine grid of $0 \leq x \leq 10$, the integrand at the quadrature points being generated by cubic spline interpolation of the cross sections deriving from the scattering calculations. The upper limit to the collision energy determines the highest temperature at which the rate coefficients can be reliably calculated; this temperature is, as a rule of thumb, 10 times smaller than the highest collision energy, expressed in Kelvin, to ensure convergence of the integral in equation (5.1.) The conversion of energies in cm^{-1} to temperatures in Kelvin follows the approximate rule 200 cm^{-1} = 288 K.

In view of the large size of the matrix of rate coefficients at a given temperature, we shall not attempt to discuss individual transitions. Instead, and with a view to establishing collisional propensity rules, we present the results in the form of scatter plots, as functions of $|\Delta K| = |K_j - K_i|$ and $|\Delta J| = |J_j - J_i|$.

5.3.2 Temperature dependence of rate coefficients

First, we present the high-temperature (200 K) results, obtained with the extended energy grid (with a fine spacing at low energies.) These results are compared with

those of Lees and Haque [1], their experiments having been performed at a similar temperature (294 K.)

Though we possess the results on a more complete grid, allowing a more or less direct comparison with Lees and Haque [1], this extended grid was a late development of our calculations, the bulk of our rate coefficients being obtained on a grid that was coarser at low energies and did not extend to such energies, allowing reliable rate coefficients up to 20 K only. It is found, however, that the results do not significantly vary with temperature, and that using a grid that is fine at low energies to calculate rate coefficients up to 20 K does not significantly affect the results. Therefore, it is unnecessary, and time-consuming, to run calculations to compare different potentials, basis sets and states of torsional excitation with the large number of energies contained in the extended grid.

The smaller grid, described in section 5.2, allows rate coefficients to be obtained at a maximum temperature of 20 K (this limit ensures convergence of the integral (5.1) at the high-energy tail of the Maxwellian distribution.) However, the experiments of Lees and Haque (1974) were performed at room temperature, and astrophysical applications may require considerably higher temperatures than 20 K; possibly in the region of 200 K. Therefore, though the $J = 9$ basis set is somewhat inadequate for this purpose, we decided to run higher energy calculations with a view to reaching 200 K despite their provisional nature, since provisional results are preferable to no results in this experimentally important high temperature regime. Therefore, the CS calculations were repeated for high collision energies, using the MP2 potential with the $J = 9$ (i.e. intermediate barrier) basis, in order to obtain an extensive grid with which to calculate rate coefficients at much higher temperatures without a corresponding extension of the basis. The rate coefficients were obtained from the cross-sections as detailed in section 5.3.1. With the grid used to obtain results at lower temperatures, extending in energy only up to 300 cm^{-1}, only rate coefficients at a temperatures up to $\approx$ 20 K will be converged. Yet, with an energy grid extending to 1300 cm^{-1}, it is possible to obtain rate coefficients at $T = 200$ K, which is closer to the temperature range of the experimental rate coefficients obtained by Lees and Haque [1]. Also, such an extension of the col-

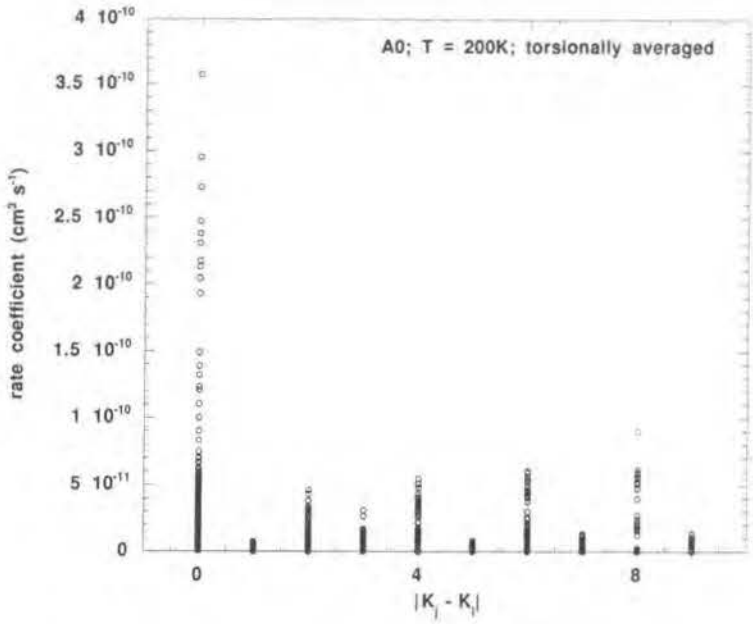

Figure 5.3: Rate coefficients for A-type methanol in ground torsional state, at kinetic temperature T=200 K. The coefficients are plotted as a function of $|\Delta K| = |K_j - K_i|$.

lision energy range allows rate-coefficients for higher collision energies to converge to reliable values, and it also increases the robustness of our determination of the rate coefficients when higher energy levels are involved. For instance, in the case of an open channel at the high J/K end of the basis, this channel may remain closed until considerable collision energies are reached, therefore significantly reducing the number of $\sigma(E)$ data points available for interpolation and integration. The rate coefficients for such transitions may therefore be unreliable.

In order to facilitate the extension of the rate coefficient calculations from 20 K to 200 K, which is nearer to the temperature regime of the experiments by Lees and Haque,(i.e. room temperature) the grid of energies was extended from 300 cm^{-1} to 1300 cm^{-1}, and it is apparent that the 'propensity rules' experimentally obtained by Lees and Haque are consistent with this analysis at a similar temperature. In fact, on the basis of the two temperatures at which rate coefficients were calculated (20 K and 200 K), the qualitative behaviour (i.e. the ΔK and ΔJ propensities) of the rate coefficients would seem to be independent of temperature. See Figures 5.3 and 5.4 for the ground-state A and E-type results at 200 K, and Figures 5.5 and 5.6 (upper panel) for the corresponding results at 20 K.

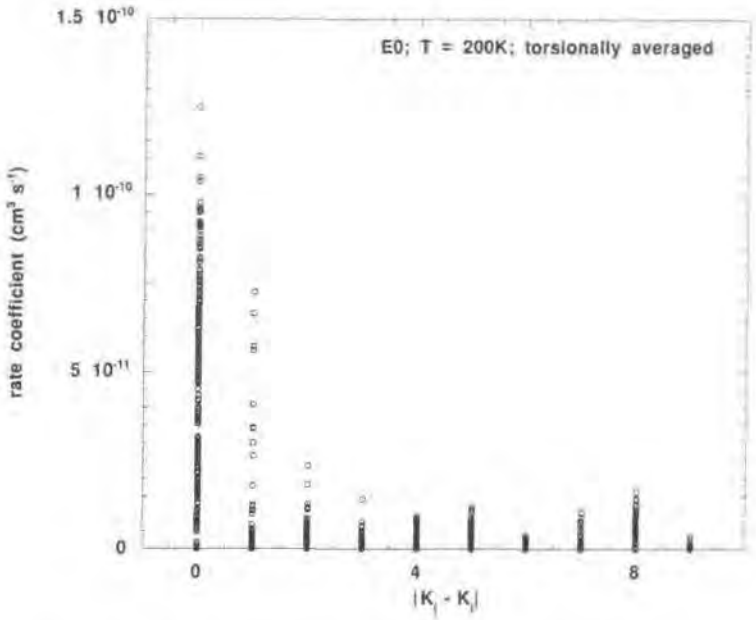

Figure 5.4: Rate coefficients for E-type methanol in ground torsional state, at kinetic temperature T=200 K. The coefficients are plotted as a function of $|\Delta K| = |K_j - K_i|$.

As can be seen from Figures 5.4 and 5.6, the $\Delta K = 0$ and $\Delta K = 1$ propensities for $E0$ obtained at 20 K may be confidently expected, on the basis of the 200 K results, to persist into the room-temperature regime at which the microwave double-resonance experiments of Lees and Haque were performed. However, the $A0$ exhibits a propensity for $\Delta K = 0$ only (a $|\Delta K| = 1$ propensity is not present for $A0$ (see Figure 5.3.))

5.3.3 Comparison of rate coefficients obtained using 'staggered' and 'torsionally averaged' potentials

First we compare the rate coefficents obtained with the 'staggered' and 'torsionally averaged' potentials (see equations (4.26) and (4.29)). In Figure 5.5 are plotted, for A-type, the rate coefficients (in $\mathrm{cm^3 s^{-1}}$) at $T = 20$K, as functions of $|\Delta K|$; results are plotted for both downwards and upwards inelastic transitions. The upper panel shows the rate coefficients obtained with the 'torsionally averaged' potential, the lower panel with the 'staggered conformation' potential. The corresponding plots

for E-type are shown in Figure 5.6.

From their microwave double resonance measurements on E-type methanol in helium, Lees and Haque (1974) [1] deduced a propensity for $\Delta K = 0$, 1 transitions, with $\Delta K = 0$ being about 4 times more probable than $\Delta K = 1$. Our results (Figure 5.6) may be seen to exhibit similar propensities, which are more pronounced when the torsionally averaged potential is used. We interpret this difference (between results obtained using V^{stg} and V^{tor}) as arising from the reduced rigidity of the molecule when released from the constraint of maintaining a fixed rotation angle, γ. This observation applies particularly to transitions ΔK =even, for which there is an increase of almost a factor of 2 in the rate coefficients when the staggered potential V^{stg} is replaced by the torsionally averaged potential V^{tor}.

The ideal treatment of the potential would consider each torsional state separately, giving a different set of potential expansion coefficients for each torsional quantum number. However, such a treatment would involve the calculation of cross-sections for torsional excitation, which is considerably more difficult than calculations in which the torsional state is fixed. As it stands, the V^{tor} torsionally averaged potential is much more realistic than the staggered V^{stg} potential.

Therefore, it may be concluded that the propensity rules established by Lees and Haque for E-type are sensitive to torsion occurring within methanol, and the rates of excitation/de-excitation of ΔK =even transitions are particularly affected by the presence of torsion. Results for A-type methanol (Figure 5.5) show a similar trend, although the collisional propensities are less pronounced than for E-type.

In Figures 5.7 and 5.8 are presented the corresponding scatter plots as functions of $|\Delta J| = |J_j - J_i|$, for A-type and E-type respectively. In this case, the electric dipole selection rules ($\Delta J = 0$, 1) are not well simulated by the theoretical data. Rather, we find that transitions with $|\Delta J| = 1$ are preferred, relative to those with $\Delta J = 0$; this propensity is more pronounced when the torsionally averaged potential is employed. On the other hand, for $|\Delta J| > 1$, the rate coefficients are approximately proportional to $1/|\Delta J|$, as predicted by Lees and Haque (1974) from the analysis of their experiments.

The origin of the discrepancy for transitions involving $\Delta J = 0$ becomes clearer

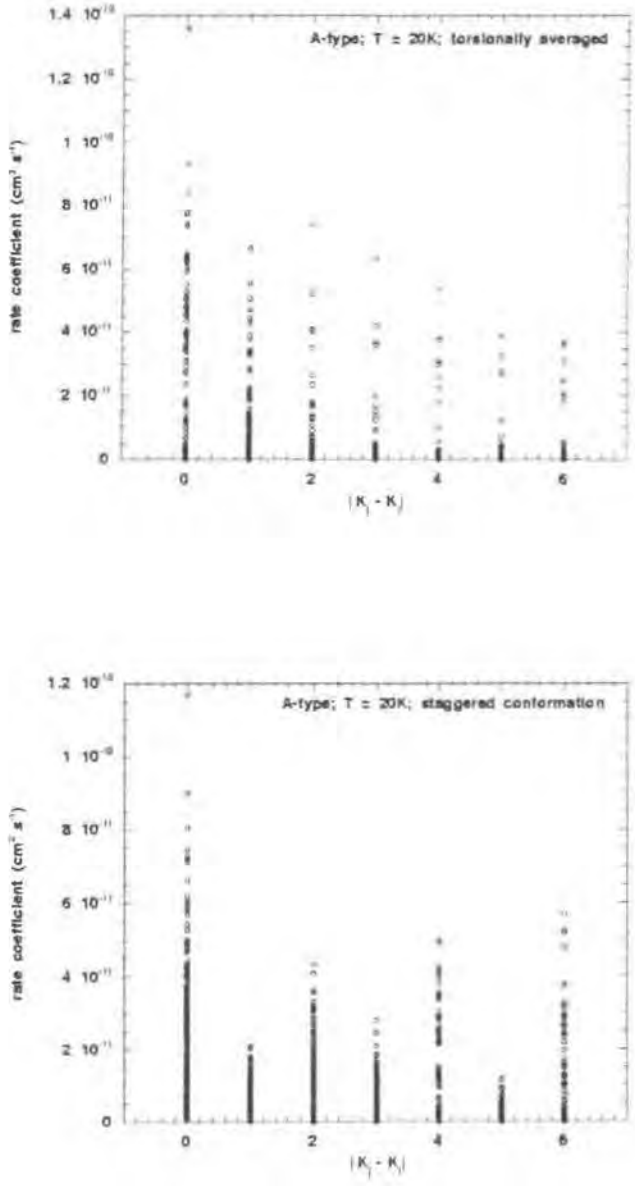

Figure 5.5: Rate coefficients at $T = 20$ K for inelastic transitions in A-type methanol, induced in collisions with helium, as functions of $|\Delta K|$ in the transition. The results in the upper panel were obtained using the interaction potential defined in Equation (29), Chapter 4, in the lower panel using the potential in Equation (26), Chapter 4.

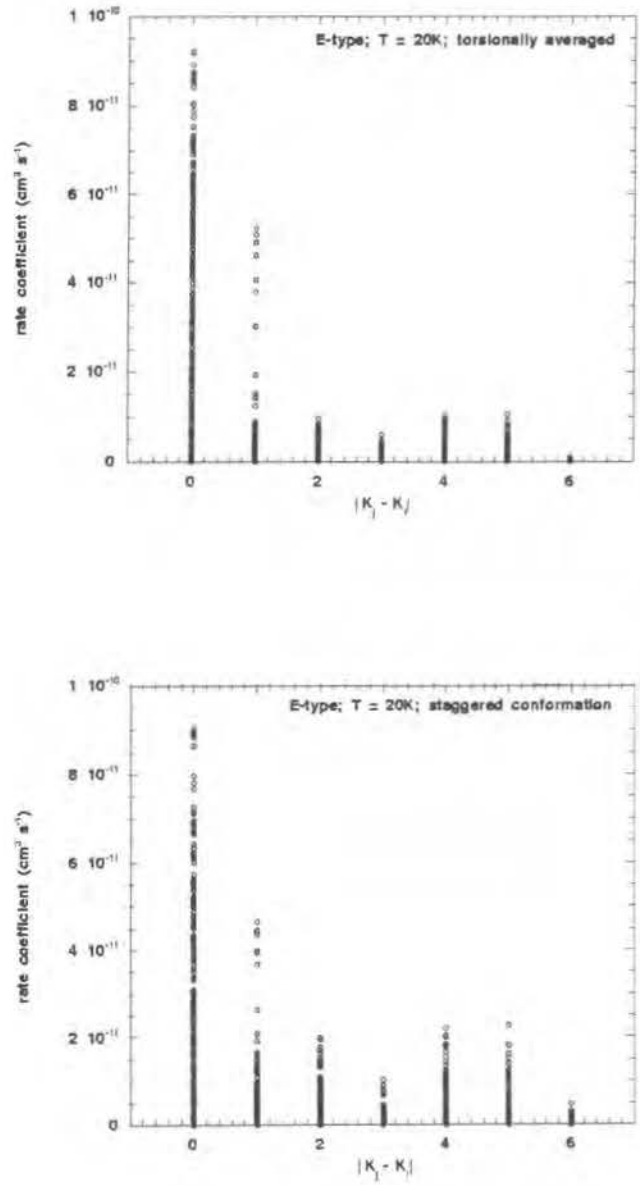

Figure 5.6: Rate coefficients at $T = 20$ K for inelastic transitions in A-type methanol, induced in collisions with helium, as functions of $|\Delta K|$ in the transition. The results in the upper panel were obtained using the torsionally averaged interaction potential defined in Equation (29) in Chapter 4, in the lower panel using the 'staggered conformation' potential V^{stg} in Equation (26). Chapter 4.

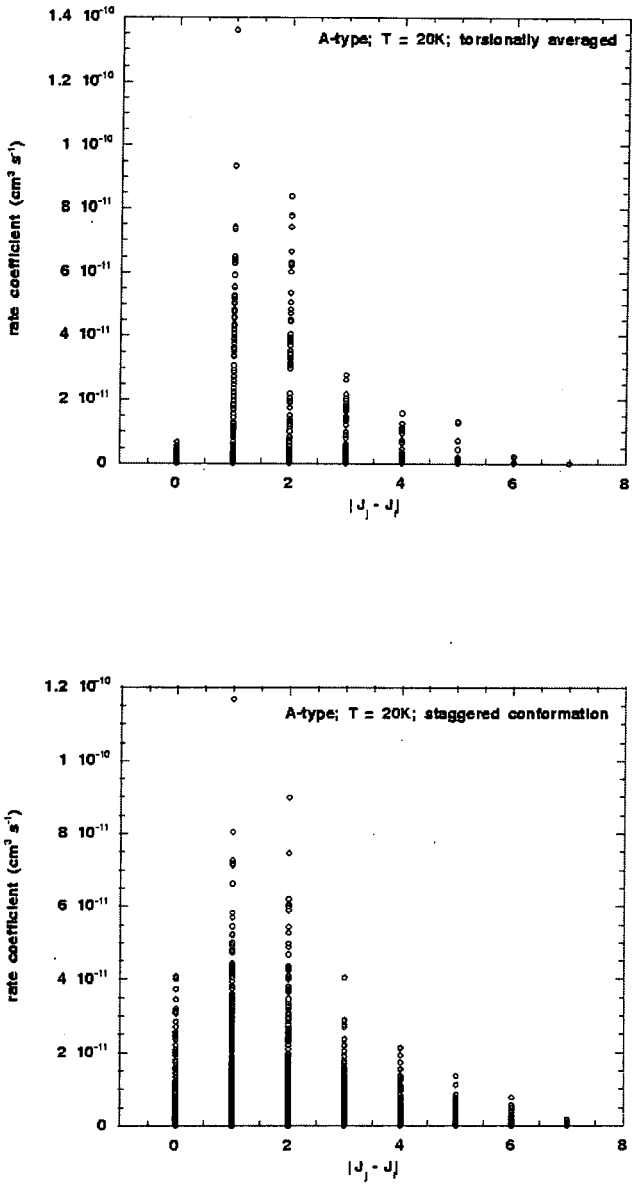

Figure 5.7: Rate coefficients at $T = 20$ K for inelastic transitions in A-type methanol, induced in collisions with helium, as functions of $|\Delta J|$ in the transition. The results in the upper panel were obtained using the interaction potential defined in Equation (29), Chapter 4, in the lower panel using the potential in Equation (26), Chapter 4.

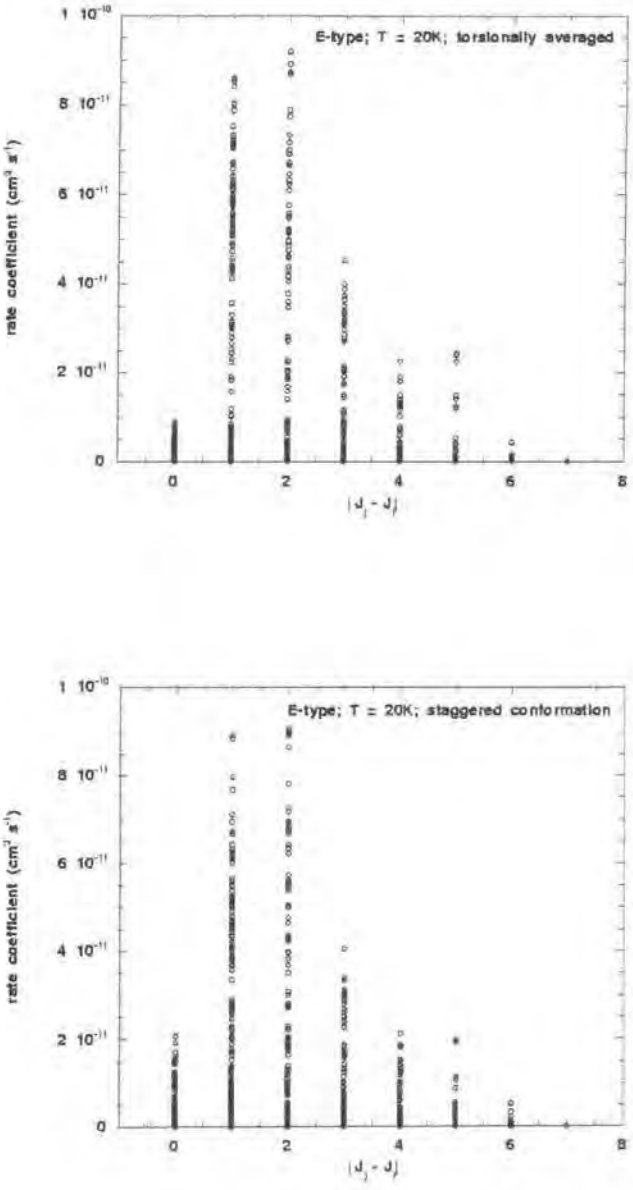

Figure 5.8: Rate coefficients at $T = 20$ K for inelastic transitions in E-type methanol, induced in collisions with helium, as functions of $|\Delta J|$ in the transition. The results in the upper panel were obtained using the torsionally averaged interaction potential defined in Equation (29) in Chapter 4, in the lower panel using the 'staggered conformation' potential V^{stg} in Equation (26. Chapter 4.

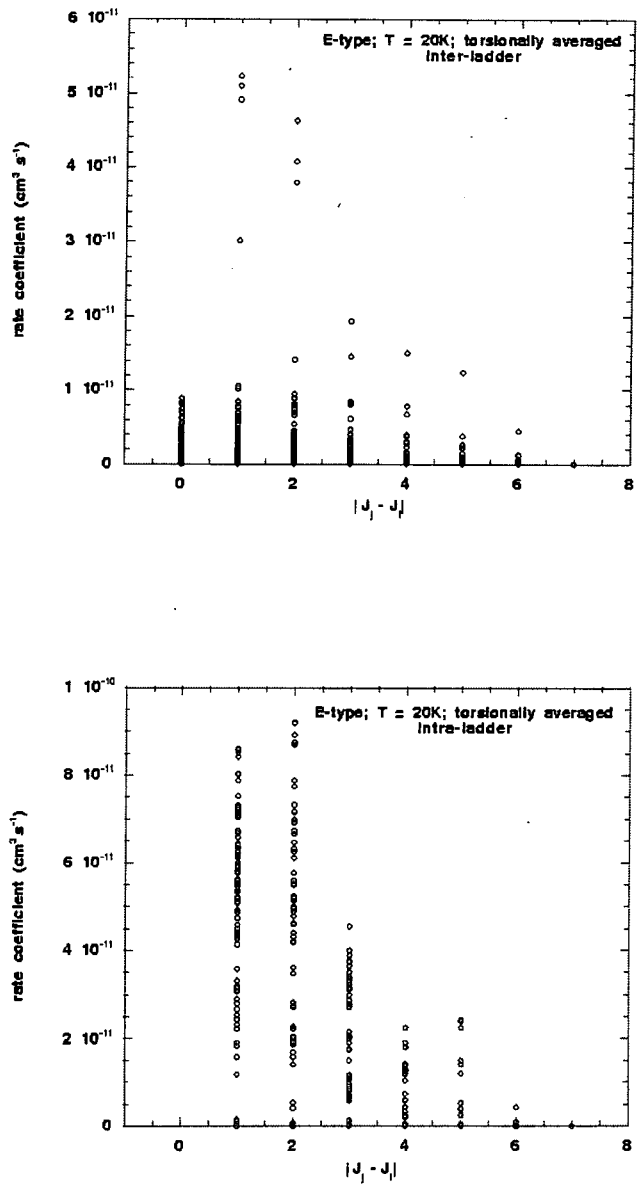

Figure 5.9: Rate coefficients at $T = 20$ K for inelastic transitions in E-type methanol, induced in collisions with helium, as functions of $|\Delta J|$ in the transition. The results in the upper panel refer to *inter-ladder* transitions ($\Delta K > 0$) and in the lower panel to intra-ladder transitions ($\Delta K = 0$). The interaction potential defined by Equation (29), Chapter 4, was used.

when results are plotted separately for intra- and inter-K ladder transitions (see Figure 5.9). As we are considering inelastic transitions, $\Delta J = 0$ implies that $|\Delta K| > 0$, and therefore a transition to a different state in the K ladder. The upper panel of Fig. (5.9) shows that, with few exceptions, inter-ladder transitions in which $\Delta J = 0$ and $|\Delta J| = 1$ have comparable probabilities. On the other hand, intra-ladder ($\Delta K = 0$) transitions, which exclude the possibility of $\Delta J = 0$, have probabilities which tend to be larger than the probabilities of inter-ladder ($\Delta K \neq 0$) transitions. Thus, it is the absence of $\Delta J = 0$ from intra-ladder transitions which leads to the apparent discrepancy with the conclusions of Lees and Haque (1974). These authors were concerned with specific pump and signal transitions, whereas the analysis here is more statistical in nature. A further difference, which may be significant, is that their measurements were performed at room temperature ($T =$ 294 K), which is much higher than the temperatures which we considered initially. Later, we extended T to 200 K.

5.3.4 Comparison of rate coefficients for 'high barrier' and 'intermediate barrier' basis

Increasing the basis set from $0 \leq J \leq 7$ to $0 \leq J \leq 9$ ('high barrier' and 'intermediate barrier' respectively) reduces the scatter in the $A0$ rate coefficients, making the collisional propensities clearer. See Figures 5.5 and 5.10 (upper panel) for the results with the smaller and larger basis sets. For E-type, however, the plot of rate coefficients remains essentially unchanged, with a clear propensity for $\Delta K = 0$ and $|\Delta K = 1|$ in both cases (see Figures 5.6 and 5.11 (upper panel).)

Using the 'intermediate barrier' treatment (see Figure 5.6) to calculate cross-sections and rate coefficients for the torsional ground states $A0$ and $E0$ causes ΔK =even transitions to be favoured for $A0$, whereas in the 'high barrier' approximation there is no clear propensity exhibited by $A0$. Conversely, the behaviour of $E0$ is relatively unaffected by the extension of the basis set.

We may conclude that E-type methanol, at least in its torsional ground state, would seem to be significantly less sensitive to changes in the basis set and the

torsional barrier height as regards its collisional propensities. In contrast, the ΔK =even 'propensity' for $A0$ noted above *is* sensitive to the height of the torsional barrier and the size of the basis set used.

5.3.5 Comparison of ground and first torsionally excited states

Rate coefficients were obtained from the cross-sections for transitions within the first torsionally excited states, $A1$ and $E1$. When one compares the rate coefficient plot for the torsional ground state of A-type methanol with the corresponding plot for the first torsionally excited state (the comparison is plotted in Figure 5.10), one finds that for $A0$ there is a favouring of ΔK =even transitions, and $|\Delta K|$ = even transitions are also favoured in collisions of Helium with A-type methanol in its first torsionally excited state ($A1$.)

The same comparison for $E0$ and $E1$ (Figure 5.11) reveals that the propensity for $\Delta K = 0$ and $\Delta K = 1$ in the case of $E0$ also applies to $E1$.

5.4 Investigation of Resonance Structures at Low Energies

It is known that resonances occur in the regime of low collision energy (i.e. close to the threshold of a transition.) That is, a large change in cross-section occurs over a small energy range. These resonances can be broad and high, and may therefore have an effect upon the calculation of the rate coefficients, in which one integrates the cross-sections, convolved with a Maxwellian distribution function, over a grid of energies.

In general, such resonances are due to the incoming species being temporarily bound, for a lifetime τ in the potential, the width of the resonance, centred on the

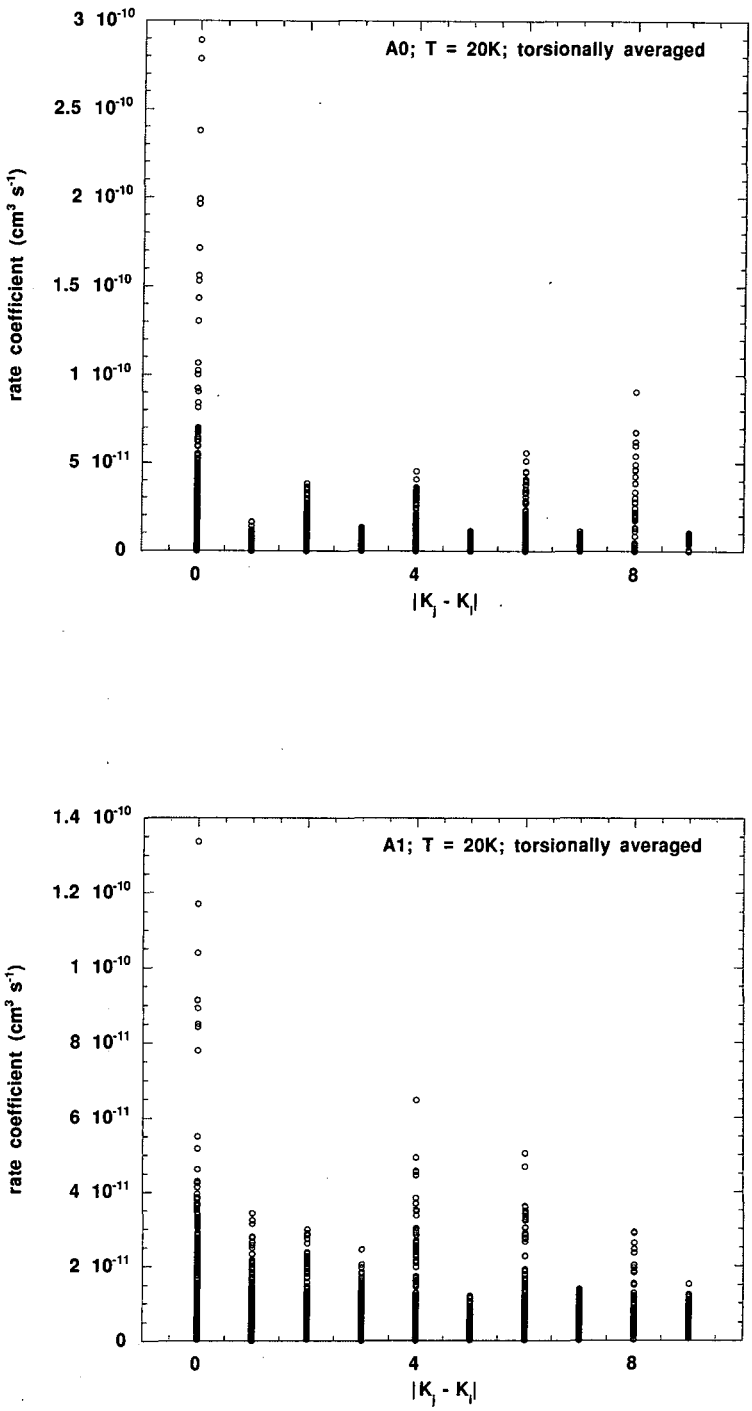

Figure 5.10: Rate coefficients as a function of $|\Delta K| = |K_j - K_i|$ for ground and first excited torsional states, $\nu_t = 0$ and $\nu_t = 1$ for A-type methanol. Only the de-excitation rate coefficients are plotted. Kinetic temperature: T=20 K.

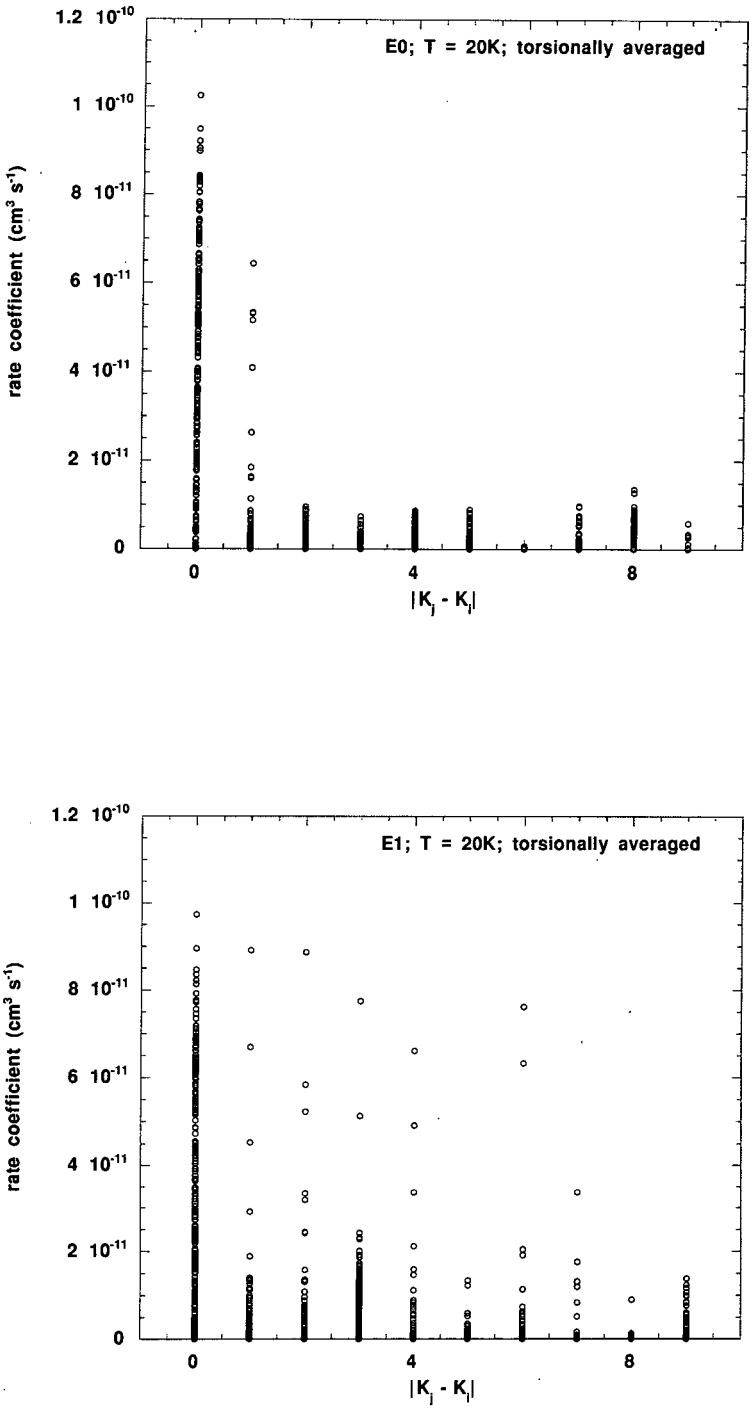

Figure 5.11: Rate coefficients as a function of $|\Delta K| = |K_j - K_i|$ for ground and first excited torsional states, $\nu_t = 0$ and $\nu_t = 1$ for E-type methanol. Only the de-excitation rate coefficients are plotted. Kinetic temperature: T=20 K.

resonance energy E_r, being approximately equal to:

$$\Gamma = \frac{\hbar}{\tau} \tag{5.3}$$

Narrow resonances occur when, for instance, the projectile becomes bound in a strongly attractive potential well, resulting in a long capture, during which the projectile may 'orbit' the centre of the potential. These so-called 'shape resonances' are typically caused by the projectile becoming briefly bound between the *repulsive* tail of a centrifugal barrier and the top of the barrier itself. Centrifugal barriers in potentials are usually low, and therefore an incoming particle can quickly tunnel through to the region nearer the centre of the potential. The bound state is therefore only a metastable state, since it has associated with it a small lifetime τ.

When such temporary captures occur, there is a phase shift through an odd multiple of $\pi/2$ as the collision energy is increased through $E_r - \Gamma/2, E_r$, and $E_r + \Gamma/2$. This phase shift is associated with the logarithmic derivative of the radial part of the wavefunction *within* the classical turning point of the potential well, which varies rapidly over a small energy interval when a metastable 'level' is encountered.

Metastable scattering states within potential wells can be neatly visualised on a complex plane of scattering energies. Imaginary energies in the outgoing solution cause the scattered wave to decay exponentially, and this is equivalent to an energy at which the incoming wave is 'captured' by the potential. On the complex plane, these metastable states E_r correspond to points on the *real* line at which poles on the complex plane are near the real line.

The shape of a resonance is given approximately by the Breit-Wigner Formula [37] in the ideal limit of a narrow resonance in a 'hard-sphere' potential:

$$\sigma(E) = \frac{4\pi(2l+1)}{k^2} \frac{\Gamma^2/4}{(E-E_r)^2 + \Gamma^2/4} \tag{5.4}$$

For most of our calculations, the smaller grid is used (see section 5.2), which is, at low energies, sparse relative to a grid sufficient to resolve all resonance peaks

which are present at low energies. Therefore, if we calculate rate coefficients at a low temperature (e.g. of the order of 10 K), the values obtained may misrepresent the true values which would be obtained on a very fine grid.

Clearly, any resonances occurring will have a non-zero effect on the final rate coefficients, but it is necessary to determine how important this effect is. That is, one must determine the height and width of these resonances (small, sharp resonances will have a small effect on the integral), and one must also investigate how well our existing grid 'traces' the variation of the cross-sections on a corresponding fine grid at low energies.

For these low-energy resonance search calculations, we modified the MOLSCAT integrator in order to obtain closer convergence such that the fine structure of the resonances is resolved to a greater accuracy. In the previously used input deck for MOLSCAT, the hybrid log-derivative/Airy propagator (INTFLG=8) was instructed to end its integration at a distance of 12 bohr. However, for the construction of a σ(E) graph at low energies on a fine grid, the range of integration was increased. As the collision energy is ,in this regime, much less than the depth of the potential well, and is comparable to the height of the centrifugal potential, the effective potential seen by the colliding species has more detail. The range of integration was therefore moved towards the origin from 4 a_0 to 2 a_0, and extended out from 12 a_0 to 20 a_0 as a precaution.

The result of running MOLSCAT on a grid from 1 cm^{-1} to 20 cm^{-1} in steps of 0.25 cm^{-1} was that it became apparent that a grid-step of 0.5 cm^{-1} is quite sufficient to resolve any resonances in reasonable detail. Plotting the grid-points already present in our cross-section data on the same graphs as these fine-grid resonance structures, we are able to see that the points of the coarser grid at 1 cm^{-1}, 5 cm^{-1}, 10 cm^{-1}, 15 cm^{-1} and 20 cm^{-1}, while they do not completely resolve the resonance peaks, at least represent an average of the cross-sections over these peaks, by alternately over-estimating and underestimating the 'true' curve. Examples are presented in Figures 5.12-16.

The resonance peaks found were all broad resonances, with a width at half-maximum of approximately 2 cm^{-1}, and a typical height of 40 cm^{-1}. As regards

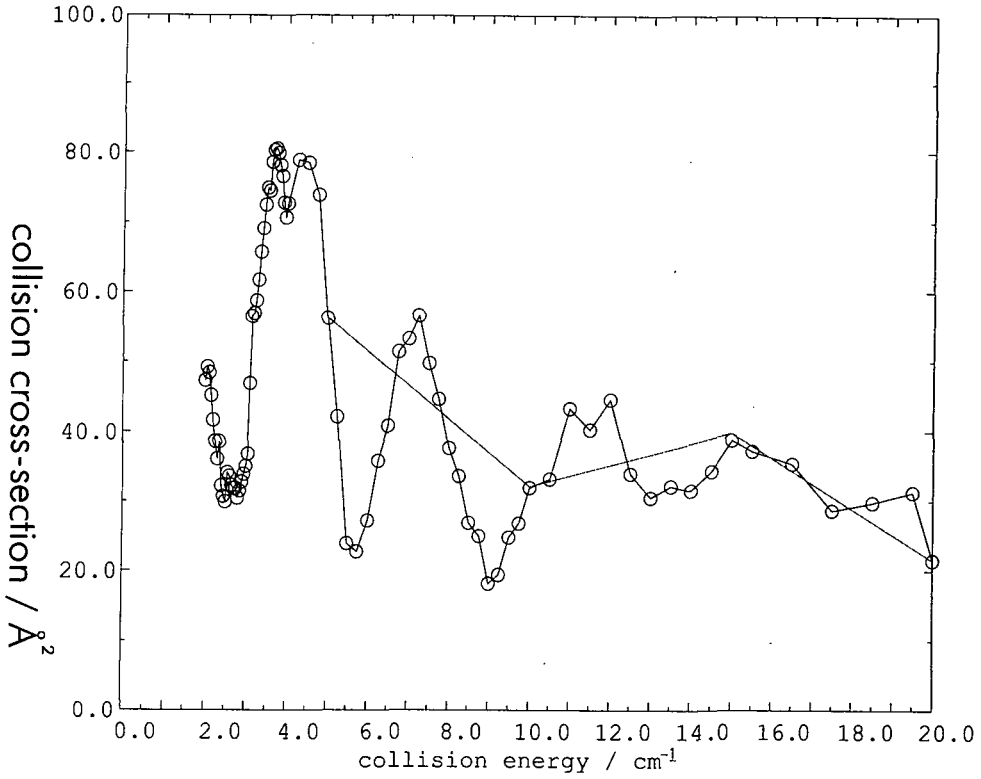

Figure 5.12: Resonance structure at low collision energies, for $1_0 \rightarrow 0_0$ transition in A-type methanol, plotted on the finer grid. Superimposed are the data points in the coarser grid.

the position of these peaks, no appreciable resonances are observed above 15 cm^{-1}. This consideration makes 20 K (or thereabouts) the minimum kinetic temperature at which rate coefficients can be extracted from our data on the coarser grid. If one attempts to evaluate rate coefficients at lower temperatures, the resonances will no longer occupy the low-energy tail of the Maxwellian distribution over which integration is performed.

Appending the fine grid data referred to above (for the range 1 cm^{-1} to 20 cm^{-1} to the existing cross-section results allows us to more accurately calculate the rate coefficients at low kinetic temperatures. We verified, however, that the qualitative behaviour of the rate coefficients, in terms of the favouring of certain ΔK transitions, remains *unchanged* at low energies.

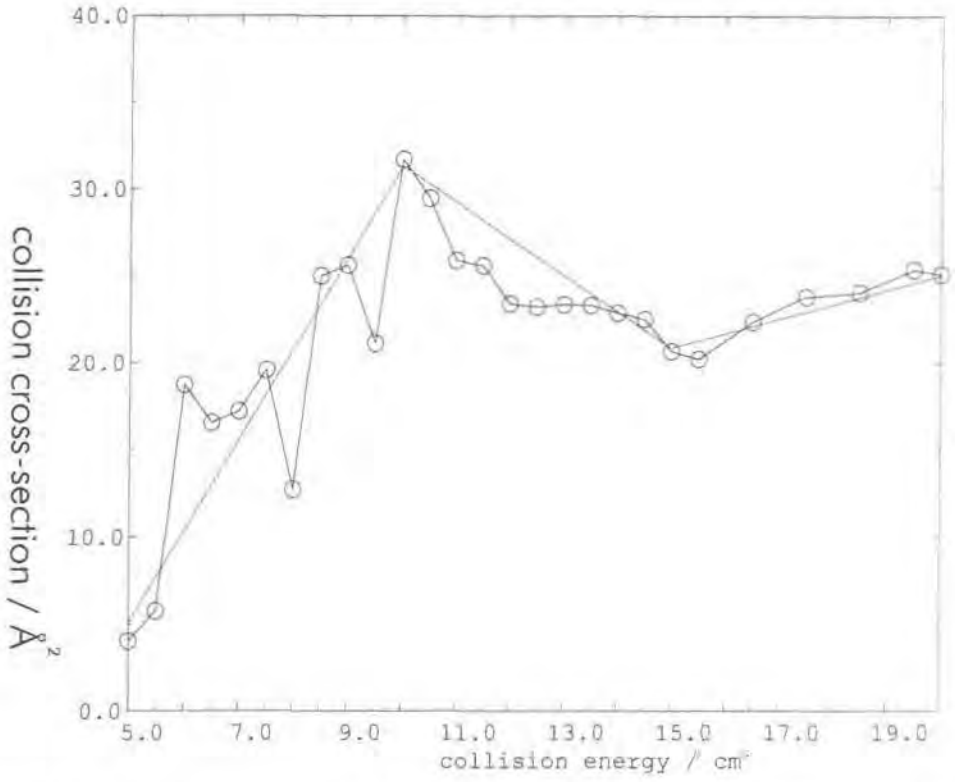

Figure 5.13: Resonance structure at low collision energies, for $2_0 \rightarrow 0_0$ transition in A-type methanol, plotted on the finer grid. Superimposed are the data points in the coarser grid.

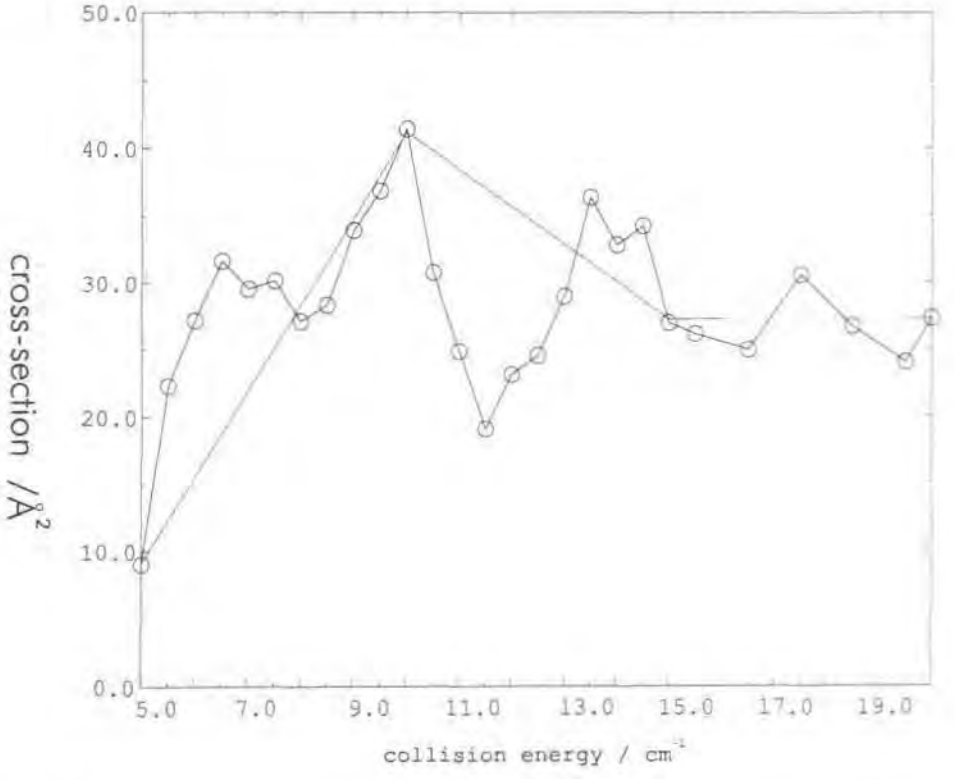

Figure 5.14: Resonance structure at low collision energies, for $2_0 \rightarrow 1_0$ transition in A-type methanol, plotted on the finer grid. Superimposed are the data points in the coarser grid.

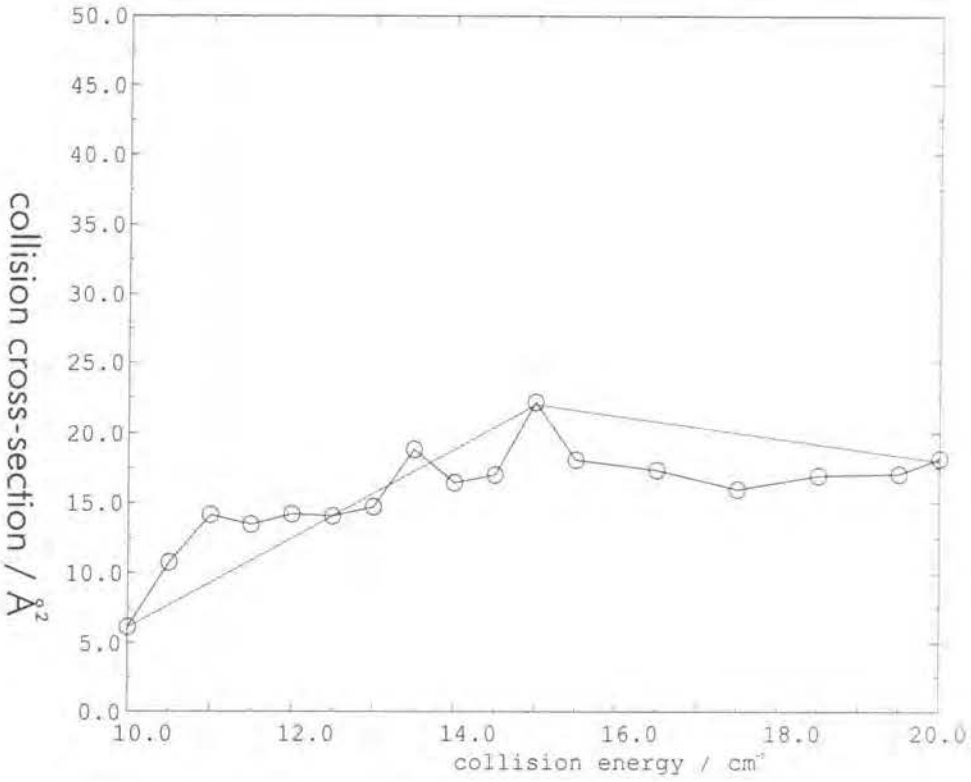

Figure 5.15: Resonance structure at low collision energies, for $3_0 \rightarrow 1_0$ transition in A-type methanol, plotted on the finer grid. Superimposed are the data points in the coarser grid.

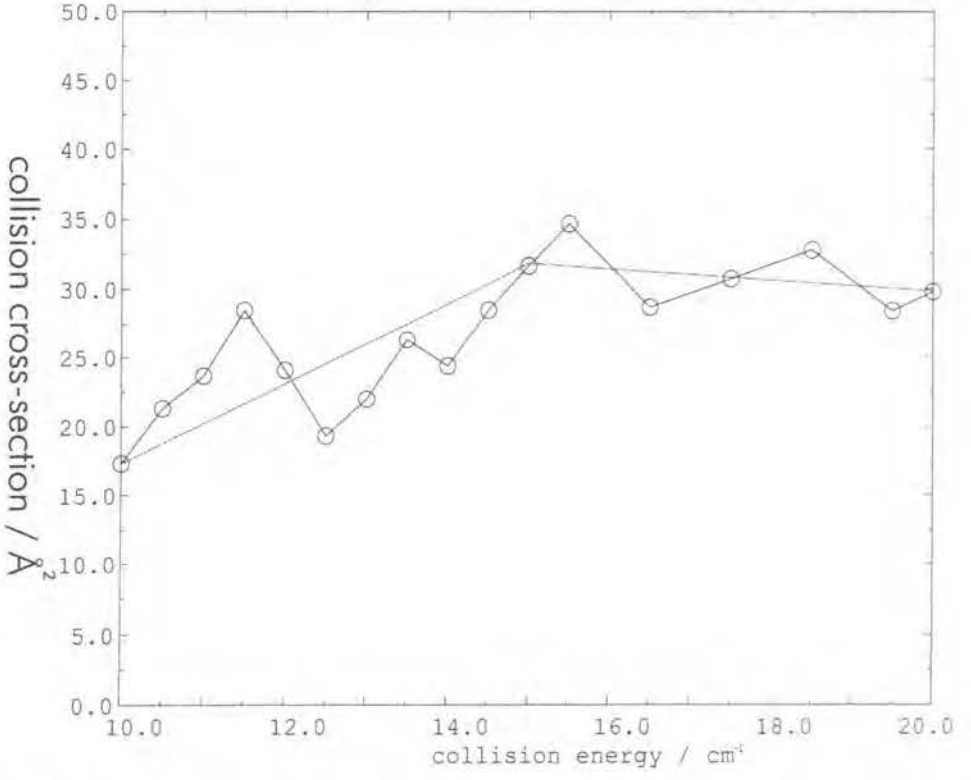

Figure 5.16: Resonance structure at low collision energies, for $3_0 \rightarrow 2_0$ transition in A-type methanol, plotted on the finer grid. Superimposed are the data points in the coarser grid.

Chapter 6

Astrophysical Results

In this chapter we make use of the collisional rate coefficients we have obtained, in the astrophysical context presented in section 1.1 of the Introduction, the underlying idea being to use these rate coefficients to provided an indirect means of determining the physical conditions within molecular clouds. Rate coefficients have been obtained for collisional processes occurring at temperatures between 20 K and 200 K, with 20 K being a typical kinetic temperature of gas within cold, dark nebulae. In these cold clouds, collisional processes are the dominant factor in determining emission and absorption spectra.

Embedded within molecular clouds, which consist mainly of molecular hydrogen, one may find regions of neutral atomic hydrogen (HI) and ionized atomic hydrogen (HII). The protostar within a HII region heats and ionizes a portion of the surrounding molecular cloud. Areas of cool, neutral atomic hydrogen (HI) are in the early stages of gravitational collapse leading to the development of a protostellar object, the gas kinetic temperature within these areas being, typically, of the order of 100 K. In HII regions (such as the Orion Nebula), where the gas is ionized by UV light from a central young star (O or B type), the gas kinetic temperature is commonly of the order of 10^4 K.

Dust within molecular clouds absorbs UV radiation and re-radiates it at far-infrared and sub-millimetre wavelengths, the typical dust colour temperature being around 20 K. The infra-red emission from dust has been shown to be instrumental [38] in pumping methanol masers. However, in cold, dark molecular clouds, where

there is no central star to irradiate the dust, collisional processes and the cosmic microwave background radiation are the main causes of molecular transitions within the cloud, and no methanol masers are excited. Indeed, anti-inversion (the opposite of masing action) has been observed towards dark clouds, the 12.18 GHz ($J_K = 2_0 \rightarrow 3_{-1}$) methanol line being observed in absorption against the cosmic microwave background.

Methanol occurs outside HII and HI regions, since the ionising conditions within HII regions are too inhospitable, and HI regions are too cold and sparsely occupied for molecules to form. Although methanol is restricted mainly to the molecular clouds surrounding these interesting regions, methanol is often observed at the interface or boundary between HI or HII regions and molecular clouds. Methanol betrays its presence within such boundaries in many ways: as masers spots near HII/cloud borders, and as emissions from outflows and accretion shocks. It has been estimated, for instance (see [2]) that the kinetic temperature of gas inside an accretion shock region within one example of a circumstellar disk is approximately 30 K, compared to a typical gas kinetic temperature within cold, dense clouds of 10 K. The physical conditions within all these boundary regions, however, remain uncertain. Methanol, by its presence in many different boundary regions, is thought to trace circumstellar disks (by means of maser spots), outflows of material perpendicular to circumstellar disks, and accretion shocks due to infall of matter within these disks.

6.1 Level populations

In a general gas cloud, there are both internal and external radiation fields affecting conditions within the cloud, in addition to molecular collisions. The total radiation field consists, in general, of several components, including internal emission from dust heated by the UV light of nearby stars, light emitted by methanol during collisional processes, and the cosmic microwave background radiation, which has a 2.73 K isotropic black-body spectrum.

To simulate the conditions within a cold molecular cloud irradiated by the cosmic microwave background (2.73 K), we calculated the distribution of level populations resulting from CH_3OH-He collisional processes together with spontaneous and induced absorption/emission. In the absence of a young star, the radiation density pervading the cloud becomes that of an isotropic black-body radiator at the temperature of 2.73 K. Therefore, combining collisional processes with the action of a radiation field upon the methanol and helium system, we can simulate the manner in which the rotational energy levels of methanol will be populated by these effects. One solves the equilibrium equations for the methanol/helium and radiation field system, which yields the relative level populations. The only extra data required, apart from rate coefficients, are the relevant Einstein 'A' coefficients for spontaneous decay from each level. The equilibrium equations for the collision of methanol/helium in the presence of a radiation field are:

$$\frac{dn_i}{dt} = \sum_{j \neq i}[A_{ji} + B_{ji}\rho(\nu_{ij}) + n_{He}k_{ji}]n_j - [\sum_{j \neq i}A_{ij} + B_{ij}\rho(\nu_{ij}) + n_{He}k_{ij}]n_i, \quad (6.1)$$

where B_{ji} is the Einstein 'B' Coefficient for emission induced by the radiation field, A_{ji} is the Einstein 'A' Coefficient for spontaneous emission, and n_i and n_j are the populations of the lower and higher levels in a transition. $\rho(\nu_{ij})$ is the radiation density for a transition $i \rightarrow j$. n_{He} is the helium number density, and k_{ij} are the rate coefficients for collisional excitation, in cm^3s^{-1}. Assuming that equilibrium has been reached in the gas cloud, we can equate $\frac{dn_i}{dt}$ to zero. One of the aims of performing such level population calculations is to establish whether so-called 'anti-inversion' occurs amongst any of the methanol levels–that is, whether the population of the anti-inverted level is depressed relative to the expected population of that level assuming only thermal excitation is responsible for the distribution of level populations. More generally, we wish to determine the sensitivity of selected line ratios to the physical parameters of the model, notably the gas density.

6.2 Absorption in the 12.18 GHz transition of E-type methanol

We have calculated the steady-state level populations of methanol, using a program which was kindly supplied to us by Malcolm Walmsley. The energy levels and Einstein A-coefficients are generated within the program, following Pickett et al (1981) [39]. We found that the transition probabilities differed by no more than 4 percent from the results tabulated by Lees (1973) [40] and Pei et al (1988) [26], for E- and A-type, respectively. Using models including the 100 lowest levels, up to $(J,\ k)=(9,\ 9)$, of A-type and E-type methanol, the equations of statistical equilibrium were solved under the assumption of a Large Velocity Gradient (LVG.) The 100 level models of A and E-type methanol used in the statistical equilibrium calculations provided complete coverage of the all the available rotational states up to 358 cm^{-1} for E-type and 352 cm^{-1} for A-type, which is more than sufficient for the calculation of rate coefficients at 20 K. The empirically estimated collisional rate coefficients obtained by Lees and Haque (1974) [1], which were originally incorporated in the program, were replaced by our own theoretical rate coefficients.

The transfer equation which describes the passage of radiation through the gas of the cloud is coupled to the equations of statistical equilibrium which describe the state of the material at each point in the cloud. The coupling arises because the radiation field of the methanol molecule induces transitions between the various levels of other methanol molecules. These levels can then re-emit the radiation, perhaps at different wavelengths or in different directions. In the case of a small velocity gradient, the radiation has a long range due to the small probability of interaction with material. Large portions of the cloud are therefore coupled, and a simultaneous determination of all the relevant physical quantities at all depths is necessary. One can reduce the set of coupled integro-differential equations to the equivalent set of difference equations using quadrature, and then solve this system using a Newton-Raphson iteration scheme. The complete system is a block tridiagonal matrix and is solved using Gauss-Seidel iteration with over-relaxation. The

size of the block matrices is equal to the number of depth points. The calculation time increases dramatically with the number of frequency points involved and, as with all iterative methods, a good starting solution is essential if the iteration is to succeed.

The LVG approximation is often used to simplify the radiative transfer problem. It is also referred to as the Sobolev approximation. The Sobolev approximation assumes that only material with a Doppler shift of $\Delta V = \frac{c\Delta\nu}{\nu_0}$ contributes to the emission at frequency $\Delta\nu$. In terms of the modelling of star formation regions, this means that no two points in a cloud emit at the same frequency, or in other words, re-absorption of radiation occurs only locally, thus decoupling the emission from all points in the cloud. In practice, this requires an infalling or expanding cloud so that all points in the cloud have a different velocity. Making this assumption greatly simplifies the problem since there is then no need to calculate in detail the effect of radiation being absorbed and re-emitted on its way out of the cloud. For a small, dense core, the velocity gradient is necessarily large, and so the LVG approximation is expected to apply.

Following Goldsmith and Arquilla (1985) [41], the cloud is assumed to possess a dense core, for which the velocity gradient is given by the empirical formula:

$$\frac{dv}{dr} = 0.036 n(H_2)^{0.5}, \tag{6.2}$$

in units of km s^{-1} pc^{-1}. Note that in a dense molecular cloud, $n(H_2)$ is at least of the order of 1×10^4 cm^{-3}, giving a minimum velocity gradient of 3.6 km s^{-1} pc^{-1}. A typical intestellar cloud is observed to have a velocity gradient of around 1 km s^{-1} pc^{-1}, so densities of $n(H_2) \geq 10^4$ cm^{-3} will give rise to 'large' velocity gradients (large relative to the typical velocity gradient.)

At low densities, the excitation temperature, which is defined through the Boltzmann relation between level populations,

$$\frac{n_j}{n_i} = \frac{\omega_j}{\omega_i} exp[-(E_j - E_i)/kT_{exc}], \tag{6.3}$$

tends towards the background radiation temperature (2.73 K), and at high densities to the kinetic temperature (10 K in the calculations reported in Figure 6.1.) The $J_K = 2_0 \rightarrow 3_{-1}$ transition of E-type methanol was observed in absorption against

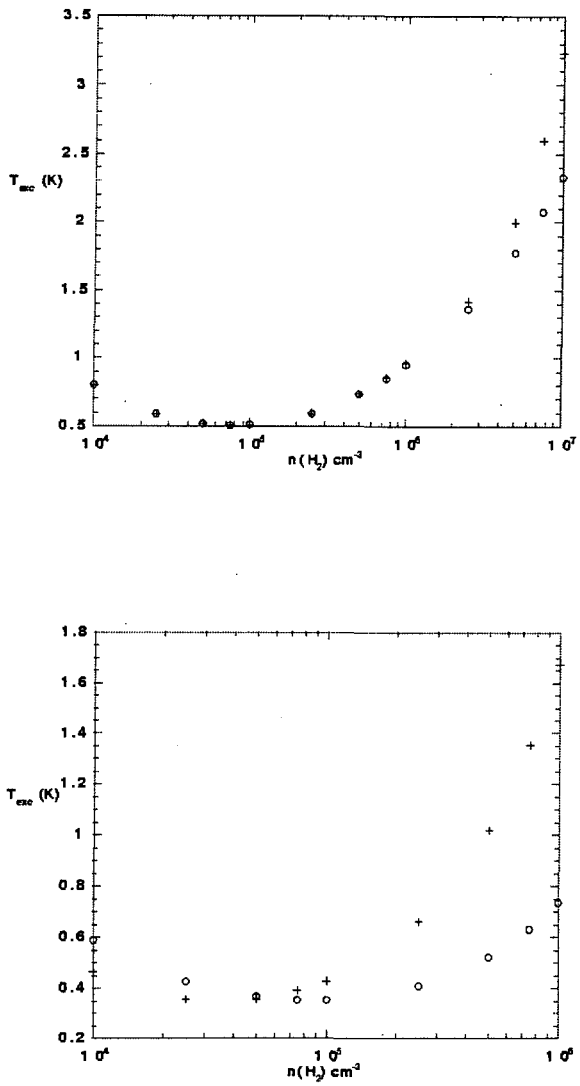

Figure 6.1: Excitation temperature of the 12.18 GHz transition of E-type methanol, as a function of the density of molecular hydrogen. Circles refer to a fractional E-type methanol abundance $n(CH_3OH)/n(H_2)=10^{-9}$ and crosses to $n(CH_3OH)/n(H_2)=10^{-8}$. The upper panel contains the present results, the lower panel the results of Walmsley et al. (1988). [38]

the 2.7 K cosmic background radiation by Walmsley et al. (1988) [38]. These authors modelled the radiative and collisional transfer of population between the levels of E-type methanol at low kinetic temperature (T = 10 K) and showed that 'anti-inversion' of population occurred through collisions in molecular gas of density $n(H_2) \approx 3 \times 10^4$ cm^{-3}. They used rate coefficients for collisional population transfer whose propensities (in terms of ΔK and ΔJ) derived from the experiments of Lees and Haque (1974) [1]; the rate coefficents were normalized to a value $q(T) = 1.3 \times 10^{-10} T^{\frac{1}{2}}$ cm^{3}s^{-1}. We recall that the calculations presented in Chapter 5 refer to collisions with He, rather than H_2, but He may be a reasonable surrogate for para-H_2 in its ground (J = 0) rotational state, which is expected to be the main modification in cold gas. In hotter gas, the ortho form of H_2 dominates over para-H_2. Using the method described above, we have recalculated the excitation temperature of the 12.18 GHz transition of E-type methanol, assuming that the rate coefficients for CH_3OH-H_2 collisions are the same as those which we computed for CH_3OH-He at T = 10 K. (Collisions with H_2 are more frequent, by a factor of approximately 1.4, owing to its lower reduced mass; but it is improbable that the rate coefficients simply scale accordingly.) We present the results in the form of graphs of excitation temperature versus density for a choice of kinetic temperature. The results are shown in Figure 6.1 for two values of the fractional abundance of E-type methanol, $n(CH_3OH)/n(H_2) = 10^{-8}$ and 10^{-9}. The calculations of Walmsley et al. (1988) [38] are also shown for comparison in the lower panel. This Figure shows that, at intermediate densities, T_{exc} falls well below 2.73 K, corresponding to 'anti-inversion' of the level populations and absorption at 12.18 GHz. The upper panel, which displays the present calculations, has been extended to $n(H_2) = 10^7$ cm^{-3} in order to show that the variation of the excitation temperature with the fractional abundance of methanol becomes qualitatively similar to that predicted by Walmsley et al. (1988) as the density increases. The similarity of the two sets of results is perhaps not surprising, in view of the generally good agreement which we obtained with the measurements of Lees and Haque (1974).

At the methanol densities considered ($n(CH_3OH)/n(H_2)=10^{-8}$), the optical depth is moderate. It is to be noted, however, that (see e.g Walmsley 1988 [38])

the results are not sensitive to the details of the velocity gradient and optical depth of the cloud. Our results, too, show this same behaviour.

6.3 Density-sensitive line ratios

Emission and absorption due to rotational transitions generally occur at microwave wavelengths. This limits the method of observation of methanol rotational lines to radio telescopes. The spectrum is very complex, and contains a large number of lines. Also, the spacing between the lines, and the line intensity, decrease with increasing J and k. Note that, in practice, no spectrograph has a sufficiently large bandwidth to instantaneously record line intensities over the entire microwave spectrum; typically, the pass-band of a receiver placed at one of the foci of a radio telescope is, at the most, 1 GHz. A real spectrum is shown in Figure 6.2, several identified transitions being marked.

Ground-based radio telescopes can only receive signals from astrophysical sources within certain windows of atmospheric transmission, as shown in Figure 6.3. The microwave band extends from 3 GHz (10 cm) to 300 GHz (0.1 cm), and, from Figure 6.3, we see that atmospheric absorption within this frequency range is quite complicated, with several windows of transmission. The dominant atmospheric absorbers at these frequencies are water and oxygen. The receiver bands in which observations of line intensity ratios could be carried out are restricted to these atmospheric windows. Also, in practice, only a small portion of each window is covered by the receivers available for a given radio telescope, making it possible to optimise the components of each receiver for a particular narrow range of frequencies. The receiver bands for radio telescopes at Granada, Mauna Kea and other locations in Europe and the U.S. collectively which can be used for observations of methanol line intensities are 13-50 GHz (2-1 cm), 85-115 GHz (0.4-0.3 cm), 120-170 GHz (0.3-0.2 cm), and 200-280 GHz (0.2-0.1 cm.)

Radiative transition probabilities for E-type methanol have been calculated by Lees (1973) [40], and, for A-type, by Pei et al (1988) [26]. The selection rules for

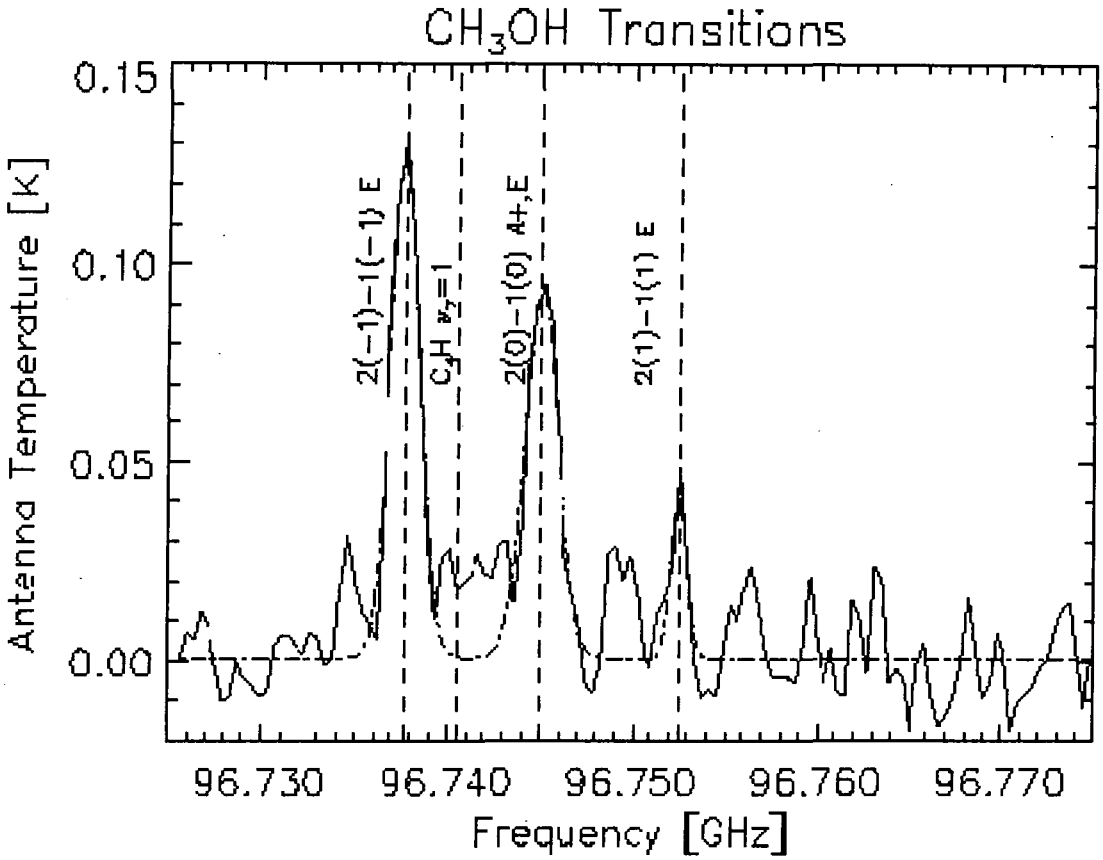

Figure 6.2: Observed methanol spectrum towards IRC 10216, obtained with BIMA radio telescope. Source: Ronak Shah, http://www.astro.uiuc.edu/ shah4/IRC10216/irc10216.html.

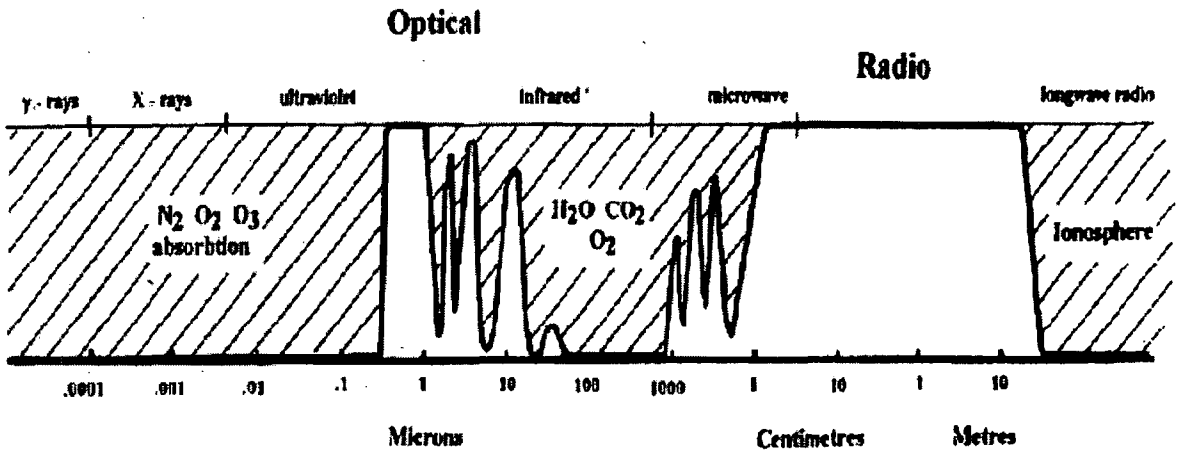

Figure 6.3: Atmospheric absorption bands. Source: Cambridge University Press, http://nedwww.ipac.caltech.edu/level5/Burke/Burke1_1.html.

electric dipole transitions are $|J - J'| = 0$ or 1, $|K - K'| = 0$ or 1; transitions with $|K - K'| > 1$ have much lower probabilities (Lees 1973 [40]). The A-coefficient is proportional to ν^3, where ν is the frequency of the transition, to the square modulus of the dipole moment matrix element D_{ji} and the torsional overlap integral:

$$A_{ji} \propto |D_{ji} < k_j\sigma|k_i\sigma > |^2 \nu_{ij}^3, \tag{6.4}$$

As noted above, the Einstein A-coefficients of transitions which are observable with the same instrument can differ by substantial factors. As a consequence, the 'critical density', at which the probability of collisional de-excitation and the radiative transition probability become equal, can vary considerably from one transition to another. The critical density is defined as

$$n_{crit} = A_{j\rightarrow i}/q_{j\rightarrow i}, \tag{6.5}$$

where $q_{j\rightarrow i}$ is the collisional de-excitation rate coefficient and $A_{j\rightarrow i}$ is the Einstein A-coefficient.

For both A- and E-type methanol, there are transitions which have similar frequencies (and which are, therefore, observable with the same instrument), whose probabilities differ by substantial factors. This fact can be exploited to determine the densities of interstellar molecular clouds from the relative intensities of

appropriate transitions of methanol. Certain transitions have small Einstein A-coefficients associated with them. As a result, the 'critical density' at which the collision rates become comparable with the radiative rates is displaced relative to the critical density of other transitions. Hence, when the ratio of the line intensities is taken, a pronounced variation with density is obtained. The requirement for a line ratio to be strongly 'density-tracing' is that one of the lines in the pair must be a transition with a small overlap, and it must be low in frequency (due to the ν^3 dependence of the A-coefficient)- preferably as close as possible to the low-frequency edge of a given observing band. The other line must be a 'large overlap' transition at the high frequency end of the chosen receiver band.

At low densities, the level populations thermalize at the temperature of the cosmic background radiation, and $T_{exc} = 2.73$ K. At high densities, $T_{exc} = T$, the kinetic temperature of the gas. The change from the low to the high temperature regime for a given transition occurs at the critical density. Thus, the relative intensities of transitions with differing critical densities can exhibit a pronounced density dependence. That is, the range of excitation temperatures between the 2.73 K cosmic background and thermalisation at 20 K corresponds to a different range of densities.

There are, however, considerations when choosing lines that are widely separated within each observing band. The beam size will be different for lines differing in wavelength, so the same observational configuration could not be used to observe both lines simultaneously.

Individual measurements of each line with a given instrument are problematic, since the pointing or focus may have changed between successive observations, thus changing the relative intensities. Thus, there are two conflicting considerations: separation in frequency increases the sensitivity of the relative intensities to the conditions within the cloud, but at the same time increases the observational uncertainties. Note that for close frequencies (which one may be forced to adopt), the overlap requirement becomes important.

In Figure 6.4, we plot the excitation temperatures of the transitions $(J, K) =$ (7,1) $\rightarrow$ (7,0) ($\nu = 166$ GHz) and (3,1) $\rightarrow$ (2,2) ($\nu = 120$ GHz) in E-type, computed

assuming a fractional abundance of methanol, relative to the perturber, of 10^{-8}, this being a typical value deduced on the basis of level population calculations using semi-empirical rate-coefficients. A kinetic temperature $T = 20$ K has been assumed. Note that, in Figure 6.4, there is a range of perturber densities for which the radiative and collision rates are of comparable magnitude, centred upon the 'critical density' at the point given by equation 6.5, lying between thermalisation at the kinetic temperature of 20 K (associated with collisions) and the cosmic microwave background (associated with radiative processes).

For the two transitions plotted (one being a 'small overlap transition', and the other being a 'usual overlap transition'), the two associated critical perturber densities are displaced by almost an order of magnitude. The two line intensities therefore have significantly different density dependencies. This difference in the behaviour of the excitation temperatures for the two lines plotted implies an equally large dependence of their relative line intensity on the density of the perturber. Such pairs of transitions, therefore, allow the determination of perturber densities in cold interstellar clouds, by the measurement of their relative line intensity. Because the variations of the line intensities mirror those of the excitation temperatures, we see that the relative line intensity can be used to deduce that the perturber density must be in the range $10^5 \leq n \leq 10^6$ cm^{-3}, for the two transitions shown. Of course, one must still assume a likely value for the (fixed) methanol/perturber density ratio.

Extensive observations of line intensity ratios are currently being planned by Peter Schilke at the Max Planck Institut für Radioastronomie, Bonn. If many lines are observed from a single source, it may be possible to infer the perturber density from different line ratios, thereby also establishing the self-consistency of the theoretical rate coefficients from which the values of the perturber density are inferred.

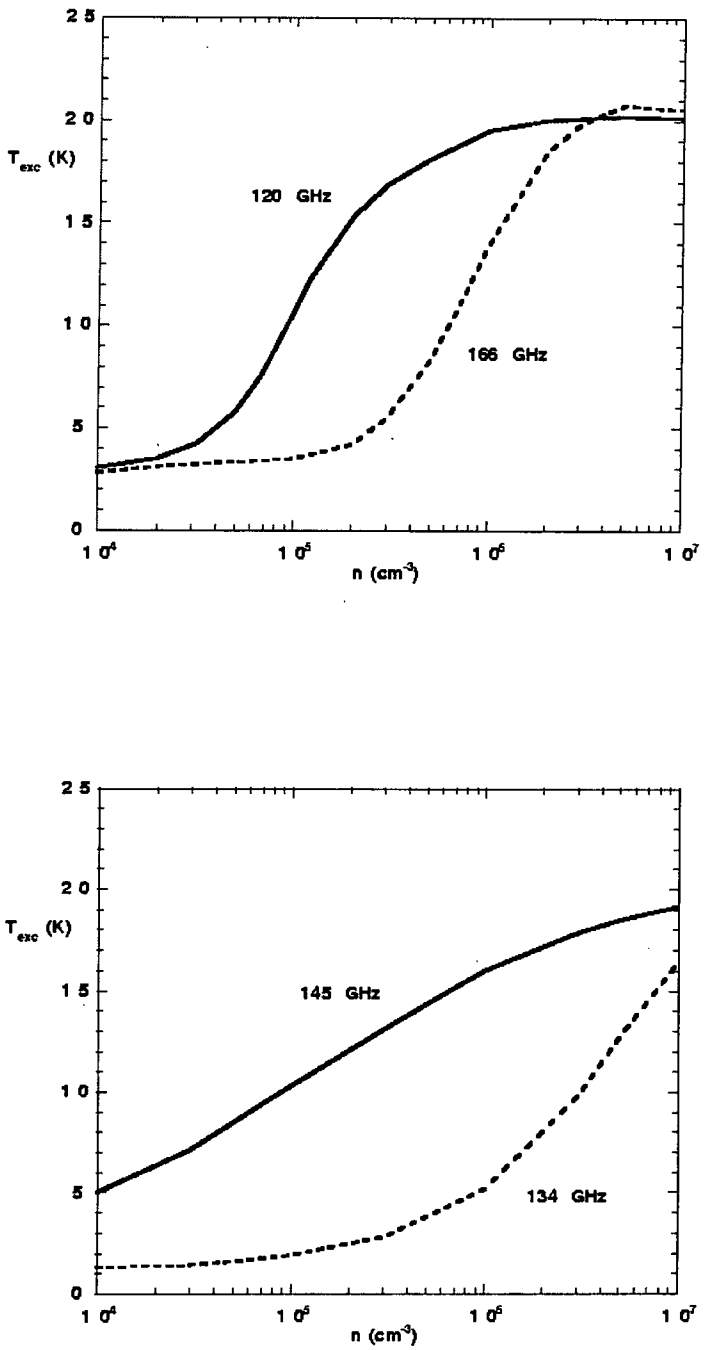

Figure 6.4: Excitation temperatures of the transitions $(J,K) = (7,1) \rightarrow (7,0)$ (ν = 166 GHz) and (3,1) $\rightarrow$ (2,2) (ν = 120 GHz), and (J,K)=(3,1) (ν = 145 GHz) together with $\rightarrow$ (2,2) (ν = 134 GHz) in E-type methanol, computed assuming a fractional abundance of methanol, relative to the perturber, of 10^{-8}. A kinetic temperature T = 20 K has been assumed.

Bibliography

[1] Lees R M and Haque S S. *Can. J. Phys.*, 52:2250, 1974.

[2] Goldsmith P F Velusamy T, Langer W D. *The Astrophysical Journal*, 565:L43-L46, 2002.

[3] Walmsley C M Reid M J Moscadelli L, Menten K M. *The Astrophysical Journal*, 564:813–826, 2002.

[4] Rodriguez L F Caselli P Bourke T L Garay G, Mardones D. *The Astrophysical Journal*, 567:980–998, 2002.

[5] Pina R K Phillips C J Telesco C M De Buizer J M, Walsh A J. *The Astrophysical Journal*, 564:327–332, 2002.

[6] Townes C H and Schawlow A L. *Microwave Spectroscopy.* McGraw-Hill Publishing Company, New York, 1955.

[7] Lin C C and Swalen J D. *Rev. Mod. Phys.*, 31:841, 1959.

[8] Lees R M and Baker J G. *J. Chem. Phys.*, 48:5299, 1968.

[9] Rodriguez-Fernandez N de Vicente P Martín-Pintado J, Gaume R A and Wilson T L. *The Physics and Chemistry of the Interstellar Medium, eds. Ossenkopf V, Stutzki J and Winnewisser G*, page 140. GCA-Verlag, Herdecke, 1999.

[10] Matthews H E Walmsley C M, Batrla W and Menten K M. *Astron. Astrophys.*, 197:271, 1988.

[11] Davis S L and Entley W R. *Chem. Phys.*, 162:285, 1992.

[12] Davis S L and Dennison E C. *J. Chem. Phys.*, 101:1293, 1994.

[13] Edmonds A R. *Angular Momentum in Quantum Mechanics.* Princeton University, Princeton, 1960.

[14] Papousek D Aliev M R. *Molecular Vibrational-Rotational Spectra : Studies in Physical and Theoretical Chemistry ; 17.* Elsevier Scientific Publishing Company, 1982.

[15] Landau L D Lifshitz E M. *Quantum Mechanics (Non-Relativistic Theory).* Butterworth-Heinemann, 1976.

[16] Bachiller R and Pérez Gutiérrez M. *Herbig-Haro Flows and the Birth of low Mass Stars, eds. Reipurth B and Bertout C.* Kluwer Academic Publishers, Dordrecht, 1997.

[17] Arthurs A M Dalgarno A. *Proc. R. Soc. Lond.*, A 256:540, 1960.

[18] Sheldon Green. *J. Chem. Phys.*, 64:3463–3467, 1976.

[19] Jacob M Wick G C. *Ann. Phys.*, 7:404, 1959.

[20] ed. Miller W H. *Dynamics of Molecular Collisions, Part A.* Plenum Press, New York, 1976.

[21] Pack R T and Hirschfelder J O. *J. Chem. Phys.*, 49:4009–4020, 1968.

[22] Biedenharn L C Louck J D. *Encyclopedia of Mathematics and its Applications: Angular Momentum in Quantum Mechanics.* Addison-Wesley, 1981.

[23] Gianturco F A. *Atomic and Molecular Collision Theory.* Plenum Press, New York, 1982.

[24] Entley W R Davis S L. *Chem. Phys.*, 162:285–292, 1992.

[25] Hutson J M and Green S. Molscat version 14, distributed by collaborative computational project 6. 1995.

[26] Zeng Q Pei C C and Gou Q Q. *Astron. Astrophys. Suppl.*, 76:35, 1988.

[27] Flower D R Pottage J T and Davis S L. *J. Phys. B: At. Mol. Opt. Phys.*, 34:3313–3330, 2001.

[28] Lester W A Jr. *Meth. Comput. Phys.*, 10:211, 1971.

[29] Secrest D. *Atom-Molecule Collision Theory: A Guide for the Experimentalist, edited by R. B. Bernstein.* Plenum Press, New York, 1979.

[30] Gordon R G. *J. Chem. Phys.*, 51:14, 1969.

[31] Johnson B R. *J. Comput. Phys.*, 13:445, 1973.

[32] Johnson B R. *Proceedings of the NRCC Workshop on Algorithms and Computer Codes in Atomic and Molecular Scattering Theory, ed. Thomas L D (Lawrence Berkeley Laboratory, CA Report LBL-9501)*, I,II:86–92,52, 1979.

[33] Manolopoulos D E. *J. Chem. Phys.*, 85:6425, 1986.

[34] Gordon R G. *Meth. Comput. Phys.*, 10:81, 1971.

[35] Alexander M H. *J. Chem. Phys.*, 81:4510, 1984.

[36] Alexander M H and Manolopoulos D E. *J. Chem. Phys.*, 86:2044, 1987.

[37] Drake G (ed.). *Atomic,Molecular and Optical Physics Handbook.* American Institute of Physics, Woodbury, New York, 1996.

[38] Matthews H E Walmsley C M, Batrla W and Menten K M. *Astron. Astrophys.*, 197:271, 1988.

[39] Brinza D E Pickett H M, Cohen E A and Schaefer M M. *J. Mol. Spectrosc.*, 89:542, 1981.

[40] Lees R M. *Astrophys. J.*, 184:763, 1973.

[41] P. F. Goldsmith and R. Arquilla. Rotation in dark clouds. In *Protostars and Planets II*, pages 137–149, 1985.

Appendix A

Assignment schemes for symmetry-adapted wavefunctions

Assignment schemes giving the correlation of even/odd K_a and K_b with $E^{\pm}, O^{\pm}$ under different conventions for the axes. Note that r and l refer to 'right' and 'left'-handed assignments with respect to the principal axis z:

I^r		
Submatrix	J even	J odd
E^+	ee	eo
E^-	eo	ee
O^+	oo	oe
O^-	oe	oo

II^r		
Submatrix	J even	J odd
E^+	ee	oo
E^-	oo	ee
O^+	oe	eo
O^-	eo	oe

III^r		
Submatrix	J even	J odd
E^+	ee	oe
E^-	oe	ee
O^+	eo	oo
O^-	oo	eo

I^l		
Submatrix	J even	J odd
E^+	ee	eo
E^-	eo	ee
O^+	oe	oo
O^-	oo	oe

II^l		
Submatrix	J even	J odd
E^+	ee	oo
E^-	oo	ee
O^+	eo	oe
O^-	oe	eo

III^l		
Submatrix	J even	J odd
E^+	ee	oe
E^-	oe	ee
O^+	oo	eo
O^-	eo	oo

Identification of the a, b and c axes with x, y and z:

	I^r	II^r	III^r	I^l	II^l	III^r
x	b	c	a	c	a	b
y	c	a	b	b	c	a
z	a	b	c	a	b	c

Appendix B

Collision calculations using SCF potential

SCF potential

As discussed in section 4.2.1, the Self-Consistent Field method (SCF) yields one possible model for the short-range part of the methanol/He interaction potential. The short-range part of the potential is added to the long-range part, given in Chapter 4, due to induction and dispersion. The SCF potential used in our initial calculations was supplied by Stephen L. Davis [24]. The complete set of expansion coefficients for this potential were supplied by Stephen L. Davis (private communication), these being used to generate the repulsive part of the total potential for subsequent use by the MOLSCAT code of Hutson and Green [25]. The potential data was supplied (see Appendix E) in the form of coefficients for the expansion of the potential in terms of spherical harmonics Y_{lm}, where:

$$Y_{lm}(\theta,\phi) = \sqrt{\frac{(2l+1)(l-m)!}{4\pi(l+m)!}} P_l^m(cos\theta) e^{im\phi} \tag{B.1}$$

$$Y_{l,-m} = (-1)^m Y_{lm}^*, (m \geq 0), \tag{B.2}$$

in which $P_l^m cos(\theta)$ are associated Legendre polynomials.

The expansion used was:

$$V(R,\theta,\phi) = \sum_{l \geq m \geq 0} v_{lm}[Y_{lm} + (-1)^m Y_{l,-m}]/[1+\delta_{0m}] \tag{B.3}$$

To ensure that the resulting potential is real, we split the summation in the expansion into $+m$ and $-m$ halves, then use the above relation between Y_{lm} and its complex conjugate (equation (B.2)) to ensure that the expansion coefficients adopt real values. We then introduce an overall factor of $\frac{1}{(1+\delta_{m0})}$ in order to counteract the double counting of $m = 0$ arising from the splitting of the summation. The result (B.3) is the expansion used in practice, and it has the advantage that the sum extends over positive l and positive m only.

Note that MOLSCAT assumes that the angle θ is measured from the z-axis, which is taken to be the symmetry axis of the top. The angle ϕ is measured from the x-z plane, which is taken to be the reflection plane. This means that it is essential for the system to be symmetric in this plane (which is commensurate with the requirement that the potential is self-conjugate except for a $(-1)^m$ factor.)

In the data supplied, expansion coefficients were available for a relatively small basis set of $l, m = 0, 0$ to $l, m = 6, 6$ for each of 5 radial points: $4a_o$, $5a_o$, $6a_o$, $7a_o$, $8a_o$,

and for various values of the internal rotation angular quantum number. The origin of the coordinate system is at the centre of mass of the methanol molecule, and the radial variable specifies the position of the colliding Helium atom relative to this.

With only five points set at intervals of 1 atomic unit (Bohr) available to define the repulsive part of the total potential for each symmetry type, it is apparent that we are dealing with a very coarse grid. Also, because the potential well of the isotropic (V_{00}) part is known to occur at $8.1a_0$, the given points do not extend well beyond the 'interesting' radial portion of the potential. Therefore, both interpolation and extrapolation of the potential data are necessary in order to make this potential useable.

However, when we come to combining the (short-range) repulsion and exclusively long-range attraction into a consistent total potential, there is a problem with continuing the functional form of the long-range attractive behaviour into the region where only the short-range part is valid. Hence we must somehow 'damp' the attractive part as we proceed towards the origin. This problem was overcome

by using the 'Tang-Toennies damping function' [24], which acts as a reducing exponential factor on both the induction and dispersion terms simultaneously, in the regions in which either part becomes inappropriate.

The Tang-Toennies damping function is based upon the expansion of e^x:

$$e^x = (1 + x + \frac{x^2}{2} + ...\frac{x^n}{n!}...) = \sum_{n=0}^{\infty} \frac{x^n}{n!}, \tag{B.4}$$

which for small x can be truncated to N terms, where N is the highest power on R in the radial dependence. The expression:

$$(1 - e^{-x}e^x) = 0 \forall x \tag{B.5}$$

can thus be altered to:

$$1 - [e^{-x} \times \sum_{n=0}^{N} \frac{x^n}{n!}] \quad \begin{array}{l} \rightarrow 0, x \rightarrow 0 \\ \rightarrow 1, x \rightarrow \infty, \end{array} \tag{B.6}$$

which has the required behaviour to damp the long-range potential in the region of small R.

As an approximation, the repulsive potential follows the empirical form:

$$V_{rep}(R, \theta, \phi) \approx Ae^{\beta(\theta,\phi)R}, \tag{B.7}$$

and we might expect any effect due to the proximity of the species to also fall off exponentially, with the same exponential factor. Apparently (according to Tang and Toennies), this assumption is correct. The full Tang-Toennies damping function is given by:

$$f_n(R, \theta, \phi) = 1 - e^{\beta(\theta,\phi)R} \sum_{n=0}^{N} \frac{(\beta(\theta, \phi)R)^n}{n!}. \tag{B.8}$$

Note that $\beta(\theta, \phi)$ also varies slightly with R. Therefore, since the damping function acts mainly on the short-range portion, the $\beta(\theta, \phi)$ for each (l, m) component was evaluated at $R = 4a_o$ (this being a convenient intermediate point not significantly affected by the interpolation and extrapolation.

The observed approximate radial dependence of the repulsive potential is very useful, but the log-derivative factor $\beta(\theta, \phi)$ is difficult to include in calculations

where the entire angular dependence of the potential is expressed *implicitly* in the form of the l, m components. I therefore assumed that $\beta(\theta, \phi)$ could be expressed as β_{lm}, that is, each component of the potential has associated with it a single β factor.

The same procedure was adopted for fitting the expansion coefficients as a function of radial distance – the explicit angle-dependent forms were not fitted directly; instead, the coefficients on each (l, m) component were subjected to a separate radial fitting. This procedure makes it easier to specify the potential in terms recognised by MOLSCAT.

The supplied data for the repulsive potential, mentioned earlier, include the internal rotation of the CH_3- group relative to OH-x. That is to say, the potential was presented as an expansion in products of spherical harmonics and eigenfunctions of the internal rotation angular momentum operator:

$$V(R, \theta, \phi, \gamma) = (2\pi)^{\frac{1}{2}} \times \sum_l \sum_m \sum_n v_{lm} Y_{lm}(\theta, \phi) e^{in\gamma}. \tag{B.9}$$

As an initial assumption, we neglected the internal rotation, which amounts to setting $\gamma = 0$, whilst, of course, still retaining the $(2\pi)^{\frac{1}{2}}$ factor, which belongs to the internal rotation term in the product. Therefore:

$$V(R, \theta, \phi) = (2\pi)^{\frac{1}{2}} \times \sum_{lm} v_{lm} Y_{lm}(\theta, \phi). \tag{B.10}$$

The expansion of the complete potential is therefore as follows (neglecting internal rotation):

$$V(R, \theta, \phi) = \sum_{l \geq m \geq n} [(2\pi)^{\frac{1}{2}} v_{lm} + f_n(R, \theta, \phi)(D^{ind}_{nlm} + D^{dis}_{nlm})] \times (Y_{lm}(\theta, \phi) + Y^*_{l,-m}(\theta, \phi)) R^{-n} / [1 + \delta_{0m}]$$

Fitting the SCF potential

Owing to the coarseness of the grid upon which the repulsive part of the potential is supplied, cubic spline interpolation was used to generate intermediate points, for use by the integration routine of MOLSCAT. Since, in the collision calculations we intend to perform, the S-matrix is propagated out into the asymptotic region to yield the final S-matrix, a fine grid is desirable. Therefore, spline interpolation

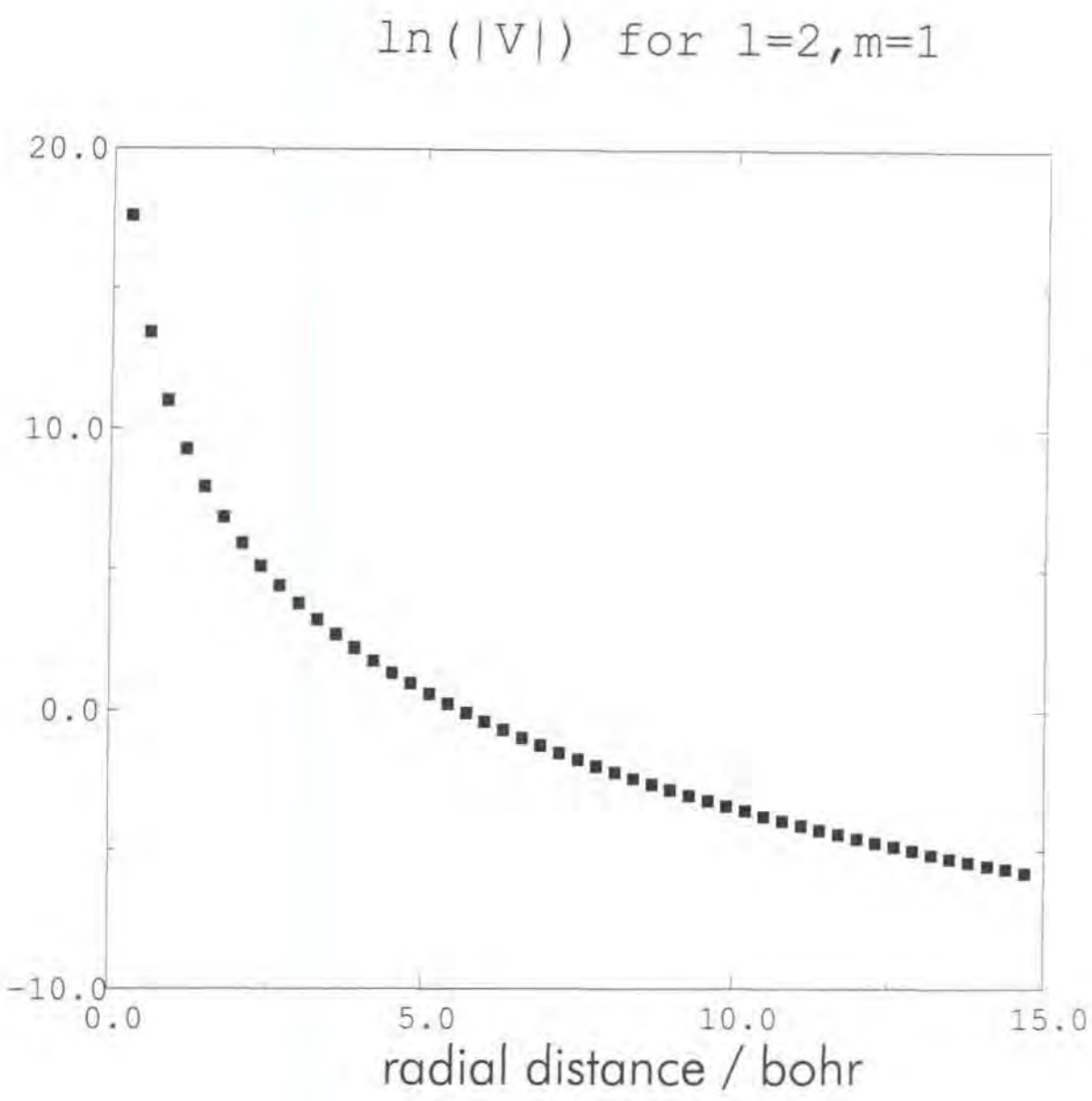

Figure B.1: Graph of radial dependence of $ln(|V|)$ for $l, m = 2, 1$, exhibiting the approximately linear portion between $R = 5a_0$ and $R = 15a_0$. Radial position R is marked on the horizontal axis in units of Bohr-radii a_0.

was used to define the potential (for MOLSCAT) on a reasonable grid of step-size $0.1a_o$.

The long-range (attractive) part of the potential is known, and can be extended to large distances (at which the exponentially decreasing repulsive part is negligible) on any required grid. Near the crucial potential well region of V_{00}, however, the attractive and repulsive parts are of comparable magnitude, so we clearly cannot neglect the repulsive part in this intermediate region, and yet the problem remains that the known data-points for the repulsive part end just before this region. Therefore, it is necessary to find a functional form for the repulsive part (considered separately) which can be used to extend the repulsive potential, after which this extended potential can be added to the attractive part. One way of doing this is to note that when we plot a graph of R versus the log of the absolute magnitude of the repulsive potential, for any given component, we obtain an approximate straight line in the region $R \geq 5a_o$. An example of such behaviour is shown in Figure B.1. This suggests, as mentioned earlier, that an approximation is:

$$V_{rep}(R, \theta, \phi) \approx Ae^{-\beta(\theta,\phi)R}, \tag{B.11}$$

so the approach initially used was to perform a least-squares fit to this form, but, because this extrapolation isn't guaranteed to match up with the last specified point of the repulsive potential, small discontinuities are produced, and it is conceivable that scattering off these discontinuities will take place.

The second problem with this simple extrapolation is that sign-changes occur on the coefficients in the known region. This, of course, does not mean that the resulting repulsive potential becomes attractive; it merely means that the necessary combination of spherical harmonics requires certain coefficients to be negative when the potential is expanded in terms of these, and the sign will not be apparent when the explicit angle-dependence of the total potential is re-assembled. These sign-changes on the coefficients cannot be represented in a fit to the form $ln|V_{lm}|$, since removing the absolute magnitude would cause the log of a negative number to be taken. Quite often, there is a sign-change at the last point ($R = 8a_o$), and this clearly affects the extrapolation. Therefore, the approach finally adopted was that

of fitting v_{lm} to the form:

$$v_{lm}(R) = (aR^4 + bR^3 + cR^2 + dR + e)e^{-\beta_{lm}R}, \tag{B.12}$$

where the general trend of a decreasing exponential is modified by a varying 'amplitude' factor in the form of a fourth-order polynomial. The polynomial part introduces the 'wiggles' caused by the sign-changes referred to above.

However, any such fit of $ln|v_{lm}|$ to a polynomial would be a good approximation in the known region, but the boundary condition of $v_{lm} \to 0$ as $R \to \infty$ is not guaranteed by this method of fitting. Therefore, with this approach, it would be necessary to arbitrarily curtail the extrapolation to remove the badly-behaved portion. The fit adopted finally was an 'exact' fit, in the sense that it was not a least-squares fit, being exact at the known data points, and it was obtained by direct solution of the simultaneous equations:

$$v_{lm}(R_1) = [aR_1{}^4 + bR_1{}^3 + cR_1{}^2 + dR_1 + e]e^{-\beta_{lm}R_1}, \tag{B.13}$$

$$v_{lm}(R_2) = [aR_2{}^4 + bR_2{}^3 + cR_2{}^2 + dR_2 + e]e^{-\beta_{lm}R_2}, \tag{B.14}$$

$$v_{lm}(R_3) = [aR_3{}^4 + bR_3{}^3 + cR_3{}^2 + dR_3 + e]e^{-\beta_{lm}R_3}, \tag{B.15}$$

$$v_{lm}(R_4) = [aR_4{}^4 + bR_4{}^3 + cR_4{}^2 + dR_4 + e]e^{-\beta_{lm}R_4}, \tag{B.16}$$

$$v_{lm}(R_5) = [aR_5{}^4 + bR_5{}^3 + cR_5{}^2 + dR_5 + e]e^{-\beta_{lm}R_5}, \tag{B.17}$$

that is, one equation for each of the five data points R_1, R_2, R_3, R_4, R_5 for a single v_{lm}, the solution of which passes exactly through each known point, thus avoiding discontinuities. The radial logarithmic derivative β_{lm} was evaluated at the last known data point, except where a sign-change occurs in this region.

Preliminary Results (SCF potential)

Cross-sections:

The MOLSCAT molecular scattering code of Green and Hutson, along with a specialised routine to facilitate the entering of a potential expanded in spherical harmonics, was used to obtain the collision cross-sections resulting from the fitted

l	K_a	K_b	Davis	fit 2	fit1
2	0	0	16.168	18.839	16.013
1	0	0	13.129	17.322	14.454
3	0	0	6.674	6.870	6.798
5	0	0	6.643	6.827	6.523
4	0	0	6.309	7.087	6.110
7	0	0	4.231	5.866	-
6	0	0	3.672	4.194	3.400
8	0	0	1.696	1.979	-
4	2	0	0.458	0.410	0.656
3	2	0	0.387	0.610	0.360
6	2	0	0.373	0.443	0.347
8	2	0	0.344	0.361	-
9	2	0	0.282	0.282	-
7	2	0	0.220	0.378	-
8	1	1	0.214	0.192	-
5	1	1	0.212	0.182	0.120
3	1	1	0.205	0.136	0.210
6	1	1	0.205	0.181	0.206
4	1	1	0.200	0.202	0.115

Table B.1: Comparison of IOS Q-factors

potential. The basis set was generated from the three rotational constants A, B and C. That is, the rigid rotor asymmetric top Hamiltonian was used to generate the energy eigenvalues. Note that, for methanol treated as a rigid rotor, there is no torsion, and hence no distinction between A- and E-type torsional symmetry species.

The first calculations done (Table 1) were IOS calculations, with both the crude initial fitting and the non-discontinuous fitting. The results at a collision energy of 500 cm^{-1} were compared with known IOS results published by Davis [44] for the same system at the same energy.

The level of agreement is reasonable for the improved fit– 30 percent error in the small-numbered l, m cross-sections, deteriorating to 60 percent error in the 'tail' of the basis set. The results in Table 1 are given in the form of a comparison of generalised IOS cross-sections (Q-factors). The quadrature adopted to obtain these values matches that used by Davis- i.e. a Gauss/Mehler quadrature on a grid of 24/6 for the θ and ϕ coordinates in the Q-factor integrals.

The closeness of the fit in the IOS regime (considering that there is some arbitrariness in the extrapolation of the potential into the asymptotic region, and that completely independent codes were used) suggests that we are justified in using our potential to perform different calculations (CS and CC) which are valid at lower energies than the IOS approximation.It is only by entering the lower energy regime accessible to CS and CC calculations that, for instance, accurate modelling of pumping mechanisms in emissions from interstellar gas-clouds becomes possible.

We take our justification for extending our calculations with this potential to lower energy (with CS and CC) from its agreement with existing results in the IOS regime of higher energy.

When we run CS and CC calculations using this potential, we notice two things:

a). The 'propensity rules' of predominance of Δ K=0 transitions, etc...,which are known to be obeyed for methanol/He at the energies (e.g. 500 cm^{-1}) at which the IOS approximation is valid, are seen to continue into the CS and CC regimes.This is encouraging, since the theory of interstellar methanol masers assumes the validity of these propensity rules at lower temperatures.

b). The CS and CC cross-sections are very close, suggesting that (at least for methanol/He) the CS approximation is sufficient for good accuracy at low temperatures (the full coupled-channel calculation being essentially exact.)

A comparison of CS and CC cross-sections is given for an energy of 100 cm^{-1} in Table B.1.

Coupled States calculations, with an asymmetric top basis up to $J = 12$, were performed at various collision energies, with the intention of drawing graphs of cross-section versus energy for some low-order transitions.The results clearly show resonance structures, where a large change in σ occurs for a small change in collision

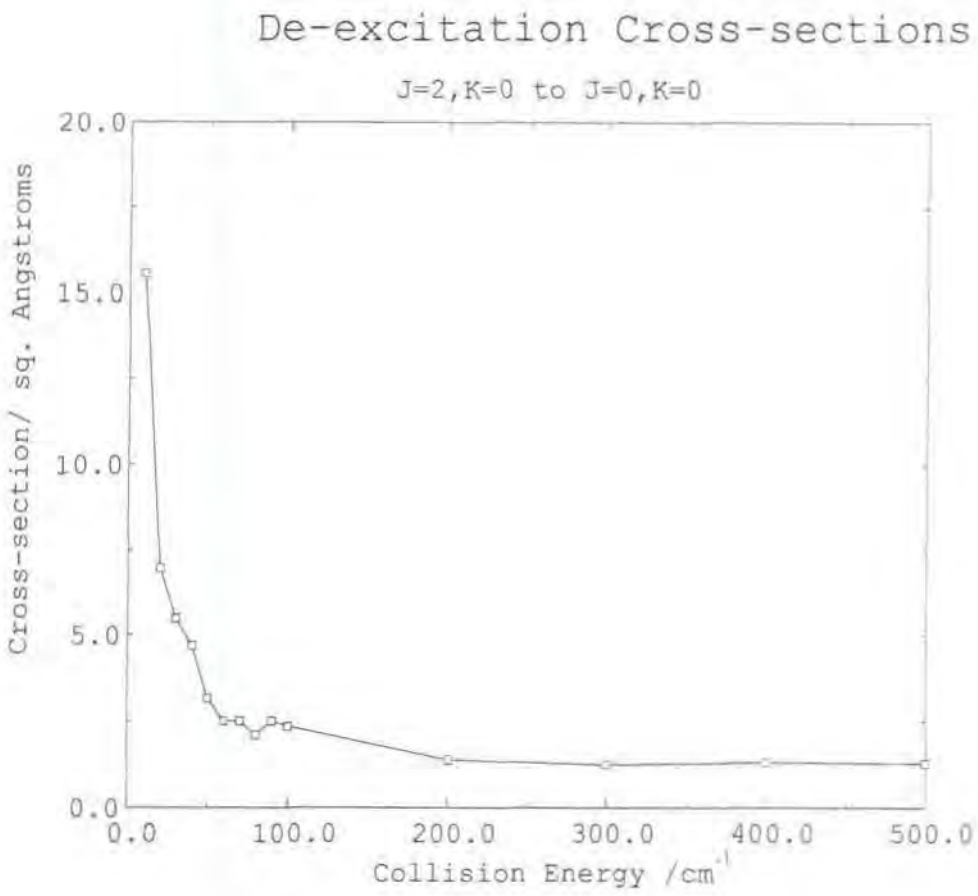

Figure B.2: Energy dependence of CS cross-sections obtained with SCF potential. $J = 2,\ K = 0 \rightarrow J = 0,\ K = 0$ is shown as a solid line.

energy.

Rate Coefficients

The experimentally useful product of cross-section calculations is the rate coefficient for a particular transition. These are averages of the inelastic cross-sections over the Boltzmann distribution:

$$k_{ij}(T_k) = \left(\frac{8}{\pi\mu(k_B T_k)^3}\right)^{\frac{1}{2}} \int_0^\infty E\sigma_{ji}(E) e^{-E/k_B T_k} dE$$

where $E = E_{TOT} - E_i$ is the energy change in a transition from state i.

To perform this integration, all the calculated cross-sections for several energies were read into a matrix, and because we are limited in the number of collision calculations we can reasonably run at any one time, we perform a cubic spline interpolation of each separate σ/E graph that is integrated to yield the rate coef-

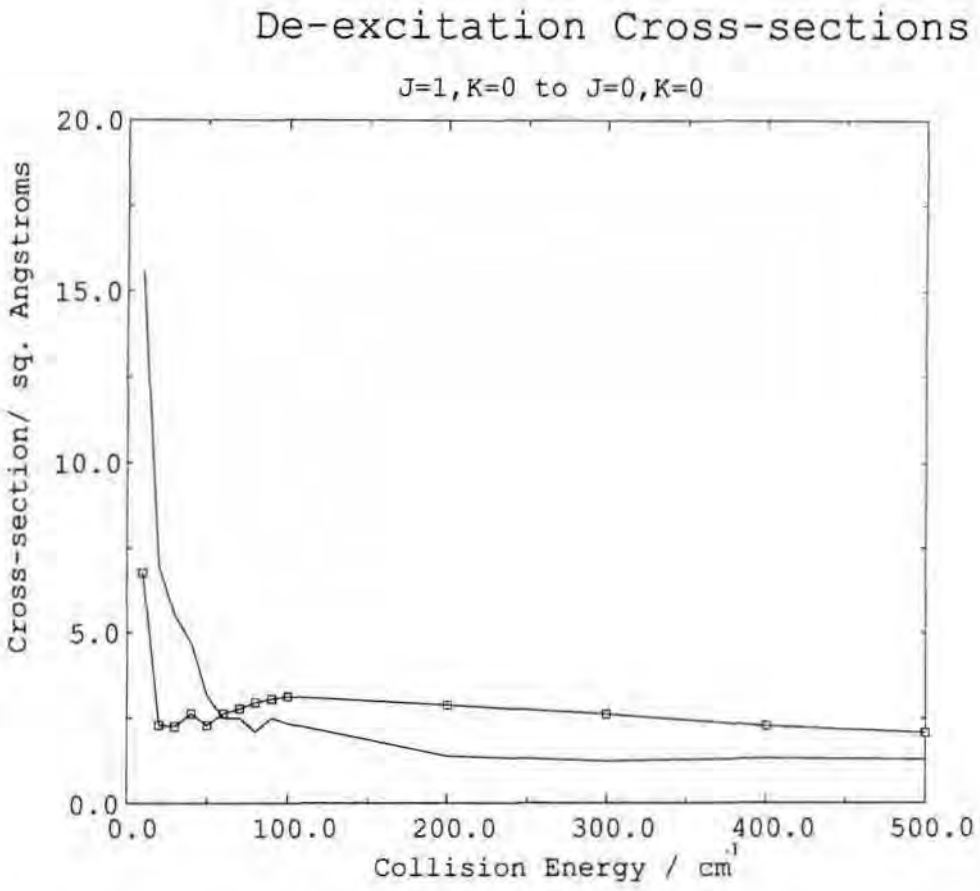

Figure B.3: Energy dependence of CS cross-sections obtained with SCF potential. $J = 2,\ K = 0 \rightarrow J = 0,\ K = 0$ is shown as a solid line, and $J = 1,\ K = 0 \rightarrow J = 0,\ K = 0$ is shown as a solid line with boxes marking each data-point.

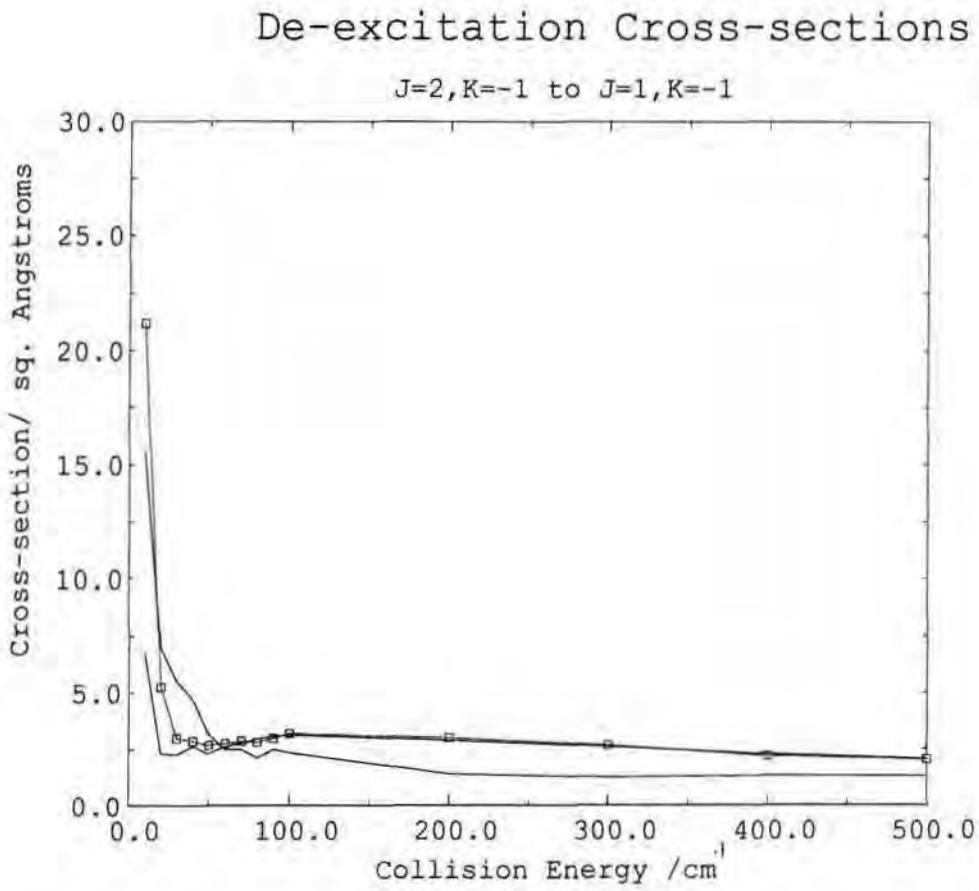

Figure B.4: Energy dependence of CS cross-sections obtained with SCF potential. $J = 2$, $K = 0 \rightarrow J = 0$, $K = 0$ and $J = 1$, $K = 0 \rightarrow J = 0$, $K = 0$ are shown as solid lines, and $J = 2$, $K = -1 \rightarrow J = 1$, $K = -1$ is shown as a solid line with boxes marking each data-point.

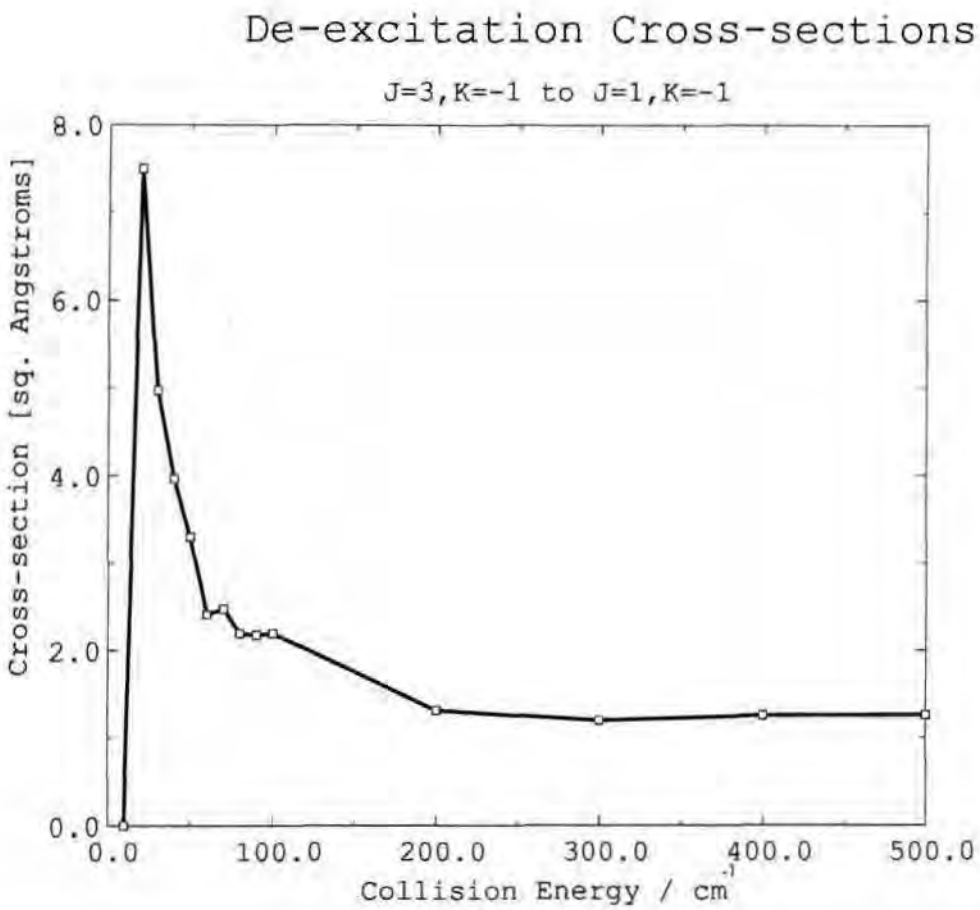

Figure B.5: Energy dependence of CS cross-sections obtained with SCF potential

ficient for each separate transition. The trapezoidal rule was used, with a step size equal to $0.1k_BT$.

After the trial with the less satisfactory SCF potential, the MP2 Potential (supplied by Stephen L. Davis in electronic form) was introduced (see section 3.1.2). This new potential is, as with the SCF potential, defined on a radial grid and expressed in terms of its expansion in normalised spherical harmonics, but the radial grid is finer, and it extends out to a more satisfactory distance beyond the region of the V_{00} potential well (at $\approx 8a_0$), and this solved the extrapolation problem which afflicted the SCF potential. More specifically, the radial grid points supplied were:

R (a_0):	4.0	5.0	6.0	6.5	7.0	7.5	8.0	8.5	9	10	12

The outermost radial point (from the origin of He/CH_3OH separation), being at $R = 12$, can almost be considered as being within the asymptotic region in which the S- matrix is defined, since this point is far removed from the V_{00} potential well, and the potential wells constitute much of the detail of the v_{lm} potential. Likewise, the l, m indices in the supplied v_{lm} coefficients extended from $l = 0, m = 0$ to $l = 15, m = 15$ for all R. The data set contained different coefficients for the cases of $E0$, $A0$, $E1$, $A1$, $A2$, 'staggered' and 'free'. This is in contrast to the SCF grid, which used $0 \leq l, m \leq 6$ and contained only 5 radial points:

R (a_0):	4.0	5.0	6.0	7.0	8.0

The fact that the complete v_{lmn} expansion is given for $A0$, $A1$, $A2$, $E0$, and $E1$ allows us to introduce a different potential specific to each of the different torsionally excited states as well as the torsional ground states. All the MP2 and SCF expansion coefficients used are given in Appendix E.

Appendix C

Energy level lists

In the following tables we give our calculated A and E-type methanol energy levels for the ground and first torsionally excited states, together with the spectroscopic values. For the method of calculation, see Chapter 4. All energies are given in cm^{-1}.

J	k	theory	experiment
0	0	0.0000	0.0000
1	0	1.6000	1.6135
1	1	11.072	11.705
1	-1	11.102	11.733
2	0	4.7999	4.8405
2	1	14.242	14.904
2	-1	14.332	14.904
2	2	26.132	31.049
2	-2	26.132	31.049
3	0	9.5994	9.6806
3	1	18.997	19.703
3	-1	19.177	19.870
3	2	30.932	35.890
3	-2	30.933	35.890
3	3	53.146	44.293
3	-3	53.146	44.293
4	0	15.998	16.133
4	1	25.337	26.101
4	-1	25.637	26.379
4	2	37.332	42.345
4	-2	37.334	42.344
4	3	59.546	50.746
4	-3	59.546	50.746
4	4	87.747	71.975
4	-4	87.747	71.975
5	0	23.996	24.199
5	1	33.261	34.516
5	-1	33.711	34.098
5	2	45.332	50.411
5	-2	45.336	50.414
5	3	67.547	58.814
5	-3	67.547	58.814
5	4	95.748	80.041
5	-4	95.748	80.041
5	5	113.94	120.04
5	-5	113.94	120.04
6	0	33.591	33.876
6	1	42.770	43.694
6	-1	43.400	43.694
6	2	54.931	44.278
6	-2	54.940	44.278
6	3	77.147	68.493
6	-3	77.148	68.493
6	4	105.35	89.720
6	-4	105.35	89.720
6	5	123.54	129.72
6	-5	123.54	129.72
6	6	162.57	168.51
6	-6	162.57	168.51
7	0	44.784	45.164
7	1	53.863	54.888
7	-1	54.703	54.888
7	2	66.130	71.382
7	-2	66.146	71.382
7	3	77.919	79.785
7	-3	77.919	79.785
7	4	100.12	101.01
7	-4	100.12	101.01
7	5	106.24	141.01
7	-5	106.24	141.01
7	6	144.26	179.80
7	-6	144.26	179.80
7	7	189.21	
7	-7	189.21	

Table C.1: A0 energy levels calculated in high barrier approximation compared with experimental values. Units: cm^{-1}.

theory	observed	J	k
294.4184	294.4620	0	0
227.5522	227.5470	1	-1
227.5822	227.5430	1	1
296.0184	296.0710	1	0
230.7222	230.7690	2	-1
230.8121	230.7590	2	1
212.8527	212.2870	2	-2
212.8527	212.2870	2	2
299.2184	299.2910	2	0
235.4771	235.6010	3	-1
235.6571	235.5820	3	1
217.6526	217.1150	3	-2
217.6527	217.1150	3	2
284.9887	284.8810	3	-3
284.9887	284.8810	3	3
304.0186	304.1200	3	0
241.8169	242.0440	4	-1
242.1169	242.0120	4	1
224.0522	223.5520	4	-2
224.0527	223.5520	4	2
291.3889	291.3170	4	-3
291.3889	291.3170	4	3
351.3172	350.1910	4	-4
351.3172	350.1910	4	4
310.4189	310.5580	4	0
249.7414	250.0980	5	-1
250.1914	250.0500	5	1
232.0514	231.5970	5	-2
232.0525	231.5970	5	2
299.3889	299.3630	5	-3
299.3889	299.3630	5	3
359.3174	358.2350	5	-4
359.3174	358.2350	5	4
318.4195	318.6060	5	0
316.8521	316.1310	5	-5
316.8521	316.1310	5	5
259.2505	259.7620	6	-1
259.8805	259.6940	6	1
241.6501	241.2510	6	-2
241.6523	241.2510	6	2
308.9882	309.0170	6	-3
308.9882	309.0170	6	3
368.9189	367.8900	6	-4
368.9189	367.8900	6	4
328.0206	328.2630	6	0
326.4536	325.7820	6	-5
326.4536	325.7820	6	5
357.4807	358.9310	6	-6
357.4807	358.9310	6	6
270.3441	271.0350	7	-1
271.1841	270.9450	7	1
252.8478	252.5130	7	-2
252.8518	252.5130	7	2
320.1866	320.2800	7	-3
320.1866	320.2800	7	3
380.1227	379.1540	7	-4
380.1227	379.1540	7	4
339.2223	339.5290	7	0
337.6564	337.0410	7	-5
337.6564	337.0410	7	5
368.6774	370.1880	7	-6
368.6774	370.1880	7	6
480.7188	482.5030	7	-7
480.7188	482.5030	7	7
283.0219	283.9180	8	-1
284.1018	283.9180	8	1
265.6444	265.3840	8	-2
265.6510	265.3820	8	2
332.9838	333.1510	8	-3
332.9839	333.1510	8	3
392.9297	392.0280	8	-4
392.9297	392.0280	8	4
352.0249	352.4040	8	0
350.4610	349.9080	8	-5
350.4610	349.9080	8	5
381.4711	383.0500	8	-6
381.4711	383.0500	8	6
493.5191	495.3680	8	-7
493.5191	495.3680	8	7
531.2872	531.6650	8	-8
531.2872	531.6650	8	8
297.2838	298.4100	9	-1
298.6336	298.2650	9	1
280.0395	279.8620	9	-2
280.0432	280.9470	9	2
347.3794	347.6310	9	-3
347.3796	347.6310	9	3
407.3407	406.5120	9	-4
407.3407	406.5120	9	4
366.4287	366.8870	9	0
364.8679	364.3820	9	-5
364.8679	364.3820	9	5
395.8608	397.5170	9	-6
395.8608	397.5170	9	6
507.9187	509.8400	9	-7
507.9187	509.8400	9	7
545.6877	546.1160	9	-8
545.6877	546.1160	9	8
540.3170		9	-9
540.3170		9	9

Table C.2: A1 energy levels: calculated values (revised method) compared with experimental values. Units: cm^{-1}.

theory	observed	J	k
353.523	352.894	0	0
355.123	354.502	1	0
475.996	476.044	1	-1
475.966	476.037	1	1
358.323	357.717	2	0
479.226	479.264	2	-1
479.136	479.246	2	1
614.653	613.679	2	-2
614.653	613.679	2	2
363.123	362.539	3	0
466.188	466.522	3	-3
466.188	466.522	3	3
483.892	484.095	3	-1
484.072	484.059	3	1
619.453	618.498	3	-2
619.453	618.498	3	2
369.523	368.969	4	0
443.047	442.909	4	-4
443.047	442.909	4	4
472.588	472.952	4	-3
472.588	472.952	4	3
490.532	490.536	4	-1
490.232	490.476	4	1
625.853	624.923	4	-2
625.853	624.923	4	2
377.523	377.006	5	0
451.047	450.946	5	-4
451.047	450.946	5	4
480.586	480.988	5	-3
480.586	480.988	5	3
498.608	498.587	5	-1
498.158	498.496	5	1
628.852	628.948	5	-5
628.852	628.948	5	5
633.853	632.954	5	-2
633.853	632.954	5	2
387.122	386.650	6	0
460.647	460.589	6	-4
460.647	460.589	6	4
490.184	490.631	6	-3
490.184	490.631	6	3
507.671	508.248	6	-1
508.301	508.121	6	1
638.452	638.586	6	-5
638.452	638.586	6	5
643.454	642.590	6	-2
643.453	642.590	6	2
698.482	698.324	6	-6
698.482	698.324	6	6
398.322	397.900	7	0
471.846	471.839	7	-4
471.846	471.839	7	4
501.380	501.880	7	-3
501.379	501.880	7	3
518.770	519.518	7	-1
519.610	519.349	7	1
599.718	599.037	7	-7
599.718	599.037	7	7
649.652	649.831	7	-5
649.652	649.831	7	5
654.655	653.832	7	-2
654.653	653.832	7	2
709.682	709.565	7	-6
709.682	709.565	7	6
411.121	410.757	8	0
484.645	484.696	8	-4
484.645	484.696	8	4
514.173	514.736	8	-3
514.172	514.736	8	3
531.535	532.398	8	-1
532.456	532.180	8	1
612.517	611.888	8	-7
612.517	611.888	8	7
662.454	662.681	8	-5
662.454	662.681	8	5
667.456	666.680	8	-2
667.454	666.680	8	2
685.286	685.440	8	-8
685.286	685.440	8	8
722.483	722.410	8	-6
722.483	722.410	8	6
425.520	425.221	9	0
499.044	499.159	9	-4
499.044	499.159	9	4
528.564	529.198	9	-3
528.562	529.198	9	3
545.731	546.887	9	-1
547.079	546.614	9	1
626.913	626.344	9	-7
626.913	626.344	9	7
740.318		9	-9
740.318		9	9
676.857	677.136	9	-5
676.857	677.136	9	5
681.858	681.132	9	-2
681.855	681.132	9	2
699.685	699.896	9	-8
699.685	699.896	9	8
736.885	736.860	9	-6
736.885	736.860	9	6

Table C.3: A2 energy levels: calculated values (revised method) compared with experimental values. Units: cm^{-1}.

J	k	theory	experiment
0	0	3.8000	3.6230
1	-1	0.4273	0.0000
1	0	5.4000	5.2460
1	1	10.467	10.751
2	-1	3.5498	3.2270
2	0	8.4069	8.4730
2	1	13.558	13.978
2	-2	14.629	14.811
2	2	17.229	17.351
3	-1	8.3489	8.0670
3	0	13.206	13.313
3	1	18.359	18.820
3	-2	19.430	19.652
3	2	22.030	22.192
3	-3	37.216	37.352
3	3	47.816	47.783
4	-1	14.747	14.519
4	0	19.603	19.755
4	1	24.761	25.275
4	-2	25.831	26.106
4	2	28.431	28.647
4	-3	43.617	43.806
4	3	54.216	54.237
4	-4	69.317	71.748
4	4	69.317	71.748
5	-1	22.742	22.584
5	0	27.596	27.827
5	1	32.765	33.343
5	-2	33.833	34.175
5	2	36.432	36.716
5	-3	51.618	51.873
5	3	62.217	62.305
5	-4	77.318	79.814
5	4	77.318	79.814
5	-5	85.433	82.978
5	5	85.434	82.978
6	-1	32.335	32.259
6	0	37.186	37.498
6	1	42.372	43.025
6	-2	43.436	43.859
6	2	46.035	46.399
6	-3	61.219	61.553
6	3	71.817	71.985
6	-4	86.916	84.229
6	4	86.916	84.229
6	-5	93.066	92.655
6	5	93.066	92.655
6	-6	95.034	92.681
6	6	95.035	92.681
7	-1	43.522	43.546
7	0	48.369	48.777
7	1	53.583	54.319
7	-2	54.642	55.157
7	2	57.239	57.698
7	-3	72.421	72.847
7	3	83.016	83.278
7	-4	98.111	100.75
7	4	98.112	100.75
7	-5	104.27	103.94
7	5	104.27	103.94
7	-6	106.24	103.97
7	6	106.24	103.97
7	-7	149.21	
7	7	149.21	

Table C.4: E0 energy levels calculated in high barrier approximation compared with experimental values. Units: cm^{-1}.

theory	observed	J	k
208.0139	208.0820	0	0
368.6014	368.6920	1	0
287.0573	287.9300	1	-1
203.0573	203.3640	1	1
212.8076	212.9100	2	0
290.2574	291.1490	2	-1
206.2573	206.5830	2	1
212.6217	212.2870	2	-2
281.8313	281.8310	2	2
217.5997	217.7310	3	0
295.0575	295.9780	3	-1
211.0572	211.4110	3	1
262.4294	262.1940	3	-2
286.6314	286.6580	3	2
233.0858	233.0260	3	-3
298.8860	298.8350	3	3
223.9993	224.1750	4	0
301.4578	302.4150	4	-1
217.4569	217.8480	4	1
268.8295	268.6310	4	-2
293.0318	293.0950	4	2
239.4857	239.4620	4	-3
305.2861	305.2710	4	3
297.3574	296.8940	4	-4
267.6669	267.7500	4	4
231.9983	232.2210	5	0
309.4537	310.4620	5	-1
321.4662	321.3750	5	1
276.8295	276.6760	5	-2
301.0329	301.1410	5	2
247.4852	247.5070	5	-3
313.2803	313.3160	5	3
305.3580	304.9390	5	-4
275.6662	275.7940	5	4
402.4331	402.4860	5	-5
323.5341	321.3750	5	5
241.5965	241.8750	6	0
319.0598	320.1180	6	-1
235.0552	235.5480	6	1
286.4293	286.3290	6	-2
310.6351	310.7960	6	2
257.0844	257.1600	6	-3
322.8866	322.9680	6	3
314.9590	314.5930	6	-4
285.2646	285.4470	6	4
412.0333	412.1400	6	-5
473.1333	473.1810	6	5
375.7041	375.7040	6	-6
375.7042	375.7040	6	6
252.7937	253.1380	7	0
330.2619	331.3830	7	-1
246.2535	246.8100	7	1
297.6288	297.5900	7	-2
321.8386	322.0590	7	2
268.2829	268.4220	7	-3
334.0870	334.2660	7	3
326.1606	325.8550	7	-4
296.4617	296.7070	7	4
423.2350	423.4030	7	-5
344.3340	342.2930	7	5
400.0388	399.8260	7	-6
386.9048	386.9620	7	6
407.4086		7	-7
407.7075		7	7
265.5896	266.0080	8	0
343.0650	344.2560	8	-1
259.0509	259.6810	8	1
310.4278	310.4590	8	-2
334.6442	334.9310	8	2
281.0806	281.2910	8	-3
346.8877	347.0900	8	3
338.9630	338.7270	8	-4
309.2570	309.5760	8	4
436.0388	436.2740	8	-5
357.1352	355.1680	8	5
399.7051	399.8260	8	-6
399.7058		8	6
420.5043		8	-7
420.2079		8	7
573.0688		8	-8
573.0688		8	8
279.9836	280.4860	9	0
357.4695	358.7380	9	-1
273.4472	274.1590	9	1
323.6501	324.9350	9	-2
349.0523	349.4120	9	2
295.4772	295.7680	9	-3
361.2886	361.5590	9	3
353.3662	353.2060	9	-4
324.8263	324.0510	9	4
450.4455	450.7550	9	-5
371.5372	369.6520	9	5
414.1060	414.2980	9	-6
414.1073		9	6
434.6066		9	-7
434.8982		9	7
587.4692		9	-8
587.4692		9	8
641.4434		9	-9
641.4434		9	9

Table C.5: E1 energy levels: calculated values (revised method) compared with experimental values. Units: cm^{-1}.

Appendix D

D_{lmn} coefficients for induction and dispersion

Multipole moments: D_{lmn} coefficients for induction and dispersion [11].

$$D^{ind}_{600} = -\sqrt{4\pi}(\mu_z^2 + \mu_x^2)\alpha, \tag{D.1}$$

$$D^{ind}_{620} = -\sqrt{\frac{1}{5}\pi}(2\mu_z^2 - \mu_x^2)\alpha, \tag{D.2}$$

$$D^{ind}_{621} = -\sqrt{\frac{6}{5}\pi}\mu_z\mu_x\alpha, \tag{D.3}$$

$$D^{ind}_{622} = -\sqrt{\frac{3}{10}\pi}\mu_x^2\alpha, \tag{D.4}$$

$$D^{ind}_{710} = -\frac{18}{15}\sqrt{\frac{4}{3}\pi}(\mu_z Q_{zz} + \mu_x Q_{xz})\alpha, \tag{D.5}$$

$$D^{ind}_{711} = -\frac{9}{5}\sqrt{\frac{8}{3}\pi}(\mu_z Q_{xz} + \mu_x Q_{xx})\alpha, \tag{D.6}$$

$$D^{ind}_{730} = -\frac{4}{5}\sqrt{\frac{4}{7}\pi}(2\mu_z Q_{xz} - 3\mu_z Q_{zz})\alpha, \tag{D.7}$$

$$D^{ind}_{731} = -\frac{2}{5}\sqrt{\frac{4}{21}\pi}(8\mu_z Q_{xz} + 5\mu_z Q_{zz} - 2\mu_x Q_{xx})\alpha, \tag{D.8}$$

$$D^{ind}_{732} = -2\sqrt{\frac{8}{105}\pi}(\mu_z Q_{xz} + 2\mu_z Q_{xx} + 2\mu x Q_{xz})\alpha, \tag{D.9}$$

$$D^{ind}_{733} = 2\sqrt{\frac{4}{35}\pi}\mu_z(2Q_{xx} + Q_{zz})\alpha, \tag{D.10}$$

$$D^{dis}_{600} = -\frac{U_1 U_2}{U_1 + U_2} 3\sqrt{\pi}\bar{\alpha}\alpha, \tag{D.11}$$

$$D^{dis}_{620} = (\frac{1}{6}\sqrt{\frac{1}{5}})(2\alpha_{zz} - \alpha_{xx} - \alpha_{yy})D^{dis}_{600}/\bar{\alpha}, \tag{D.12}$$

$$D^{dis}_{621} = -\sqrt{\frac{1}{30}}\alpha_{xz}D^{dis}_{600}/\bar{\alpha}, \tag{D.13}$$

$$D^{dis}_{622} = \frac{1}{4}\sqrt{\frac{2}{15}}(\alpha_{xx} - \alpha_{yy})D^{dis}_{600}/\bar{\alpha}, \tag{D.14}$$

$$D^{dis}_{710} = \frac{6}{5}\sqrt{\frac{1}{3}}(A_{xxz} + A_{yyz} + A_{zzz})D^{dis}_{600}/\bar{\alpha}, \tag{D.15}$$

$$D^{dis}_{711} = -\frac{3}{5}\sqrt{\frac{2}{3}}(A_{xxx} + A_{yxy} + A_{zxz})D^{dis}_{600}/\bar{\alpha}, \tag{D.16}$$

$$D^{dis}_{730} = \frac{4}{15}\sqrt{\frac{1}{7}}[3A_{xxz} - 2(A_{xxz} + A_{yyz})]D^{dis}_{600}/\bar{\alpha}, \tag{D.17}$$

$$D^{dis}_{731} = \frac{2}{15}\sqrt{\frac{1}{21}}(2A_{xxx} - 5A_{xzz} + 2A_{yyx} - 8A_{zxz})D^{dis}_{600}/\bar{\alpha}, \tag{D.18}$$

$$D^{dis}_{732} = \frac{2}{3}\sqrt{\frac{2}{105}}[A_{zzz} - 2(A_{yyz} - A_{xxz} - A_{zxx})]D^{dis}_{600}/\bar{\alpha}, \tag{D.19}$$

$$D^{dis}_{731} = \frac{2}{3}\sqrt{\frac{1}{35}}[2(A_{yxy} - A_{xxx}) - A_{xzz}]D^{dis}_{600}/\bar{\alpha}, \tag{D.20}$$

In equations (D.1)-(D.20) μ_i, Q_{ij}, α_{ij}, and A_{ijk} are the components of the methanol's dipole moment, quadrupole moment, dipole polarizability, and dipole-quadrupole polarizability, respectively. The mean polarizability $\bar{\alpha}$ of methanol is defined as $\frac{1}{3}(\alpha_{xx} + \alpha_{yy} + \alpha_{zz}.)$ The dipole polarizability of He is denoted by α. U_1 and U_2 are mean excitation energies for CH_3OH and He, sometimes taken as the ionization energies.

Appendix E

SCF and MP2 Short-Range Potentials

The following tables give a selection from the full data sets of SCF and MP2 short-range potential expansion coefficients. The full set is available from Stephen L. Davis. Given here are the coefficients for the innermost and outermost radial points (R=4 a_0 and R= 12 a_0), plus a point near the potential well of the $l = 0$, $m = 0$ isotropic component (R=8.5 a_0.)

Table E.1: SCF (minus induction): v_{lmn} in cm $^{-1}$

l	m	n	R=4 au	R=5 au	R=6 au	R=7 au	R=8 au
0	0	-6	3.531	0.0716	0.0002	0.0028	0.0001
0	0	-3	2.6895	2.1032	0.3647	0.0439	0.0084
0	0	0	142850.0696	24114.4748	3646.829	495.1495	61.6275
0	0	3	2.6895	2.1032	0.3647	0.0439	0.0084
0	0	6	3.531	0.0716	0.0002	0.0028	0.0001
1	0	-6	-4.0312	-0.047	-0.0021	-0.0046	-0.0002
1	0	-3	-2.3787	-1.7879	-0.2881	-0.0317	-0.0067
1	0	0	-76760.9284	-15673.0892	-2598.0486	-382.8585	-52.5839
1	0	3	-2.3787	-1.7879	-0.2881	-0.0317	-0.0067
1	0	6	-4.0312	-0.047	-0.0021	-0.0046	-0.0002
1	1	-6	83.7973	27.9411	6.7265	1.3531	0.2449
1	1	-3	-270.1588	-70.9879	-17.7385	-3.6661	-0.6289
1	1	0	-5582.4793	-967.448	-146.2922	-17.9992	-1.9699
1	1	3	75.9307	27.8094	7.5194	1.6087	0.2889
1	1	6	-68.3536	-24.9656	-5.4065	-1.0107	-0.1865
2	0	-6	1.4291	-0.0218	0.0051	0.0039	0.0002
2	0	-3	-1.089	-0.218	-0.0773	-0.0145	-0.0026
2	0	0	92464.5594	14605.8805	2068.2853	263.6911	30.5157
2	0	3	-1.089	-0.218	-0.0773	-0.0145	-0.0026
2	0	6	1.4291	-0.0218	0.0051	0.0039	0.0002
2	1	-6	-56.8176	-21.6778	-6.3625	-1.3519	-0.2291
2	1	-3	226.5834	56.709	17.252	3.7447	0.5979
2	1	0	-2581.8306	-179.2411	18.6705	11.7841	2.8066
2	1	3	-32.8327	-18.4395	-6.914	-1.5934	-0.2664
2	1	6	49.4734	21.3518	5.2283	1.0101	0.1756
2	2	-6	-121.7548	-20.3774	-0.0902	0.5308	0.1114
2	2	-3	-73.4051	-51.3279	-17.096	-3.9434	-0.75
2	2	0	2551.8905	327.475	34.245	1.8736	-0.1013
2	2	3	-15.4802	2.6619	1.8224	0.5154	0.1097
2	2	6	121.3226	22.3321	1.2774	-0.1966	-0.0434
3	0	-6	1.9451	0.0537	-0.0089	-0.0011	-0.0002
3	0	-3	2.9532	1.3896	0.2493	0.0329	0.0069
3	0	0	8392.9988	1706.1713	322.6537	57.1984	9.5753
3	0	3	2.9532	1.3896	0.2493	0.0329	0.0069
3	0	6	1.9451	0.0537	-0.0089	-0.0011	-0.0002

3	1	-6	-32.5583	-3.6929	0.9777	0.2908	0.0212
3	1	-3	19.4353	6.0548	-3.4884	-0.9763	-0.0757
3	1	0	-5081.094	-741.827	-99.1396	-10.039	-0.5786
3	1	3	-66.055	-9.4484	0.6822	0.3149	0.0173
3	1	6	20.3844	-0.3122	-1.0005	-0.2177	-0.0186
3	2	-6	156.7084	18.3445	-1.4545	-0.9774	-0.2074
3	2	-3	147.2109	96.0438	26.8368	5.9976	1.1834
3	2	0	4033.9011	542.8359	67.3599	6.7305	0.6404
3	2	3	-0.5646	-11.283	-3.6474	-0.8971	-0.1927
3	2	6	-170.0653	-25.2839	-0.7942	0.4178	0.0919
3	3	-6	13.3894	4.7826	0.3644	-0.0105	0.0018
3	3	-3	15275.7825	2861.1256	478.6002	72.2105	10.0419
3	3	0	-1307.3833	-192.5684	-27.2124	-2.5994	-0.076
3	3	3	22.5227	0.3105	0.4546	0.1438	0.0145
3	3	6	-14.3581	0.0326	-0.0942	-0.0456	-0.0031
4	0	-6	-3.8682	-0.0294	0.0139	-0.0015	0.0001
4	0	-3	-0.5596	-1.0268	-0.1499	-0.0159	-0.003
4	0	0	-25682.3702	-5161.4057	-929.8575	-144.0316	-19.316
4	0	3	-0.5596	-1.0268	-0.1499	-0.0159	-0.003
4	0	6	-3.8682	-0.0294	0.0139	-0.0015	0.0001
4	1	-6	73.2819	17.5615	2.9473	0.557	0.131
4	1	-3	-163.8346	-41.6217	-6.9757	-1.3196	-0.3138
4	1	0	-2076.7111	-276.4125	-30.5777	-3.6545	-0.63
4	1	3	95.1934	22.029	3.6527	0.6914	0.1613
4	1	6	-54.7135	-12.8751	-2.1924	-0.4162	-0.0975
4	2	-6	-120.7897	-5.9477	2.7852	1.0353	0.215
4	2	-3	-72.9046	-75.7862	-21.7834	-5.0217	-1.0248
4	2	0	3919.8956	452.2464	45.4134	2.1924	-0.3086
4	2	3	15.7593	13.8916	3.8681	0.9007	0.1895
4	2	6	141.1963	14.1612	-0.5096	-0.496	-0.105
4	3	-6	-20.4623	-6.5432	-0.4482	0.0307	0.0003
4	3	-3	-23691.5136	-4252.593	-694.1223	-103.3359	-14.142
4	3	0	-2164.0816	-305.9168	-42.0338	-3.9986	-0.1546
4	3	3	-34.5936	-0.4289	-0.6189	-0.1973	-0.0189
4	3	6	21.5815	-0.3565	0.0734	0.0554	0.0026
4	4	-6	-182.3777	-18.9074	-5.8433	-1.4207	-0.2178
4	4	-3	-586.2589	-119.89	-23.1251	-4.0155	-0.6437
4	4	0	429.8494	58.1964	9.1212	0.92	0.0444
4	4	3	-23.5236	-8.0691	-1.7547	-0.3305	-0.0629
4	4	6	141.025	4.62	2.2348	0.6786	0.0794
5	0	-6	3.2238	-0.033	-0.0153	0.0018	0.0003
5	0	-3	-2.0428	0.0716	-0.0023	-0.0063	-0.0018
5	0	0	23254.5271	3845.1579	619.7391	92.9856	12.3531
5	0	3	-2.0428	0.0716	-0.0023	-0.0063	-0.0018
5	0	6	3.2238	-0.033	-0.0153	0.0018	0.0003
5	1	-6	-55.809	-15.4052	-3.03	-0.5981	-0.1224
5	1	-3	149.3748	37.7076	7.6389	1.5413	0.3021
5	1	0	659.3003	181.5201	39.7037	6.4854	0.9536
5	1	3	-57.4206	-17.0174	-3.5156	-0.7218	-0.1469
5	1	6	43.101	12.5399	2.3659	0.4476	0.0924

5	2	-6	69.2907	-1.815	-2.3341	-0.6127	-0.1184
5	2	-3	-186.3214	4.5142	6.7422	1.9546	0.4194
5	2	0	2617.9649	311.0209	37.211	3.8253	0.2878
5	2	3	-0.5459	-6.741	-2.1695	-0.5006	-0.0975
5	2	6	-74.7721	-2.0584	1.1192	0.3277	0.0637
5	3	-6	18.7472	5.0566	0.2839	-0.0447	-0.0037
5	3	-3	22763.9266	3762.7365	596.0016	87.8774	11.7024
5	3	0	-2169.7534	-270.5224	-35.9797	-3.5384	-0.1579
5	3	3	32.3123	0.1663	0.4859	0.1598	0.0139
5	3	6	-19.2859	0.5263	0.0011	-0.0325	0
5	4	-6	305.583	26.3944	7.2462	1.744	0.243
5	4	-3	924.0995	177.8482	31.6479	5.2072	0.789
5	4	0	676.4791	69.5452	8.161	0.2007	-0.145
5	4	3	35.4588	11.4299	2.2091	0.3785	0.0688
5	4	6	-245.9455	-6.3625	-2.8113	-0.9092	-0.0953
5	5	-6	-2.8195	3.2662	0.2591	-0.0564	-0.0097
5	5	-3	-48.3066	4.3294	-0.4232	-0.3257	-0.0303
5	5	0	-151.0813	-18.2189	-2.4846	-0.1391	0.0111
5	5	3	47.5323	18.775	2.2489	0.1571	0.0331
5	5	6	-14.4084	-6.349	-0.5908	-0.0057	-0.0065
6	0	-6	-0.8931	0.0234	0.007	-0.0009	-0.0005
6	0	-3	2.0265	0.4526	0.0785	0.0145	0.0026
6	0	0	-14515.3948	-2209.9893	-329.1291	-45.9701	-5.652
6	0	3	2.0265	0.4526	0.0785	0.0145	0.0026
6	0	6	-0.8931	0.0234	0.007	-0.0009	-0.0005
6	1	-6	37.2564	9.8695	1.622	0.2858	0.0526
6	1	-3	-111.6369	-24.7241	-4.2815	-0.7917	-0.1342
6	1	0	-240.7281	-70.3322	-8.1425	-1.6129	-0.4018
6	1	3	29.4992	10.1035	1.8123	0.3376	0.0617
6	1	6	-28.1592	-8.1938	-1.2949	-0.2137	-0.0403
6	2	-6	-8.2164	5.6623	1.2094	0.1639	0.0256
6	2	-3	341.3829	37.9042	3.7162	0.3415	0.0371
6	2	0	1167.0799	121.2874	10.1487	0.5856	-0.0336
6	2	3	-11.0118	0.6224	0.4744	0.1067	0.0151
6	2	6	0.5071	-5.4172	-0.9698	-0.1126	-0.0182
6	3	-6	-11.222	-2.6837	-0.0701	0.0387	0.0042
6	3	-3	-15595.4214	-2290.2215	-346.6219	-50.6367	-6.5066
6	3	0	-1480.688	-150.8406	-18.7505	-2.0602	-0.1365
6	3	3	-21.8084	-0.0513	-0.2581	-0.0894	-0.0073
6	3	6	10.7654	-0.3933	-0.0504	0.0054	-0.0015
6	4	-6	-320.2165	-18.66	-4.7606	-1.2155	-0.1431
6	4	-3	-909.7533	-152.1912	-25.0362	-3.9177	-0.5523
6	4	0	841.8554	90.1265	12.2752	1.2061	0.0514
6	4	3	-30.1347	-8.3762	-1.4849	-0.2353	-0.0395
6	4	6	275.1997	4.5444	1.881	0.7136	0.0627
6	5	-6	-21.0615	-8.5959	-0.364	0.1556	0.029
6	5	-3	71.1533	-8.4998	0.7954	0.5467	0.056
6	5	0	-291.0498	-25.1799	-3.5206	-0.2769	0.0094
6	5	3	-81.6016	-30.1246	-3.4761	-0.2196	-0.0464
6	5	6	26.4149	9.8299	0.8438	-0.0045	0.0071
6	6	-6	997.9118	128.8499	20.0376	3.1104	0.3784
6	6	-3	7.5337	-0.2096	0.1811	0.0682	0.0086
6	6	0	57.9668	4.6063	0.7653	0.0638	0
6	6	3	-6.5648	-0.3152	-0.2231	-0.0636	-0.0083
6	6	6	115.8271	30.4039	3.3384	0.2072	0.0407

Table E.2: MP2 short-range potential coefficients, v_{lmn}: R=4 au. Units: cm^{-1}

l	m	E0	A0	E1	A1	A2	stg	free
0	0	53342.84	53341.42	53326.59	53333.62	53322.17	53440.27	53330.71
1	0	-29341.84	-29342.26	-29346.77	-29345.31	-29347.13	-29443.29	-29345.35
1	1	-2027.28	-2027.09	-2025.13	-2026.12	-2024.47	-2032.25	-2025.66
2	0	35465.06	35466.99	35487.39	35478.79	35491.92	35488.20	35481.46
2	1	-771.69	-774.84	-807.89	-792.84	-816.85	-748.81	-798.56
2	2	791.38	797.76	864.71	834.89	881.91	742.70	845.65
3	0	2846.38	2846.21	2844.39	2844.82	2844.49	2908.43	2845.01
3	1	-1873.85	-1868.29	-1810.09	-1836.51	-1794.43	-1907.99	-1826.55
3	2	1396.45	1389.77	1319.69	1350.91	1301.67	1455.88	1339.64
3	3	3017.68	2610.36	-1662.43	251.76	-2776.06	5372.80	-448.46
4	0	-9780.21	-9780.69	-9785.59	-9782.88	-9787.60	-9891.69	-9784.32
4	1	-760.85	-763.86	-795.34	-780.88	-804.07	-745.05	-786.49
4	2	1266.37	1264.72	1247.45	1255.34	1242.73	1253.28	1252.32
4	3	-6185.07	-5541.62	1208.10	-1816.23	2968.02	-9943.73	-709.48
4	4	15.00	29.42	181.84	118.54	214.35	-73.95	137.33
5	0	8634.47	8634.67	8636.71	8635.41	8637.80	8730.01	8636.22
5	1	78.79	78.82	78.94	78.45	79.61	83.47	79.01
5	2	986.73	994.66	1077.77	1040.42	1099.61	954.55	1054.19
5	3	4633.51	4017.95	-2439.06	454.14	-4122.69	8277.43	-604.63
5	4	430.93	406.35	147.01	256.13	89.65	580.17	222.41
5	5	-55.88	-55.11	-43.91	-34.82	-61.44	-84.75	-50.52
6	0	-5615.16	-5615.72	-5621.53	-5618.45	-5623.75	-5645.20	-5620.00
6	1	-285.68	-284.57	-272.80	-277.70	-270.27	-298.11	-276.23
6	2	534.69	524.04	412.41	462.57	383.09	595.80	444.09
6	3	-4086.64	-3657.29	846.53	-1171.62	2021.05	-6646.98	-432.96
6	4	19.18	42.84	292.62	187.96	347.23	-125.49	219.89
6	5	-78.58	-79.17	-91.00	-110.94	-57.51	-31.42	-81.51
6	6	88.25	78.36	-67.27	-190.02	167.12	457.66	19.73
7	0	848.81	849.03	851.24	849.93	852.27	811.18	850.68
7	1	186.12	185.05	173.72	178.29	171.49	197.08	177.06
7	2	163.99	173.11	268.75	225.77	293.88	101.03	241.61
7	3	1581.96	1364.03	-922.03	102.50	-1518.43	2857.97	-272.62
7	4	313.49	296.23	113.87	189.84	74.63	419.41	167.07
7	5	-90.72	-89.47	-69.89	-49.46	-107.09	-148.15	-82.54
7	6	-92.73	-74.34	199.22	438.74	-254.01	-800.62	33.62
7	7	-11.98	-11.82	-9.45	-7.66	-12.97	-17.88	-10.82
8	0	753.99	753.81	751.96	752.94	751.25	828.50	752.44
8	1	21.51	21.96	26.79	25.04	27.44	17.12	25.31
8	2	109.37	103.70	44.23	71.12	28.37	155.76	61.07
8	3	-730.74	-668.59	-16.68	-309.07	153.72	-1020.06	-201.82
8	4	40.98	49.95	144.94	105.92	164.58	-13.72	117.10
8	5	-57.28	-58.46	-76.29	-92.89	-45.31	-8.45	-65.25
8	6	199.30	175.62	-176.37	-483.90	405.82	1109.17	36.54
8	7	-17.63	-17.73	-19.97	-24.36	-12.75	-7.68	-18.03
8	8	0.72	1.31	7.46	4.92	8.76	-2.88	5.66
9	0	-831.50	-831.44	-830.78	-831.08	-830.60	-892.50	-830.96
9	1	-38.50	-38.34	-36.77	-37.92	-35.72	-40.35	-37.11
9	2	-10.63	-8.40	14.96	4.25	21.40	-32.90	8.38
9	3	-299.44	-282.80	-108.22	-186.21	-63.05	-524.98	-157.88
9	4	104.51	102.33	79.14	87.92	75.44	116.73	86.12
9	5	-55.41	-54.53	-42.09	-33.29	-59.67	-84.91	-49.11
9	6	-132.02	-108.21	246.23	557.50	-342.36	-1050.72	31.44
9	7	-21.13	-20.85	-16.34	-11.46	-25.16	-34.66	-19.30
9	8	19.12	18.03	6.50	11.37	3.94	25.73	9.85
9	9	18.66	16.10	-10.74	1.28	-17.73	33.15	-3.11

10	0	250.69	250.68	250.51	250.44	250.69	269.79	250.60
10	1	70.61	70.24	66.45	68.47	64.99	74.75	67.45
10	2	0.48	0.46	0.33	0.68	-0.13	2.52	0.30
10	3	96.46	71.67	-188.39	-72.04	-255.94	367.97	-114.46
10	4	81.05	79.24	60.37	69.28	54.78	93.60	65.62
10	5	-37.97	-38.29	-42.26	-43.03	-39.61	-31.86	-40.51
10	6	161.71	141.83	-154.16	-414.07	337.32	928.91	25.20
10	7	-14.78	-15.07	-19.69	-24.58	-10.82	-1.17	-16.69
10	8	0.49	1.72	14.66	9.23	17.51	-7.02	10.90
10	9	-43.23	-38.78	7.93	-13.00	20.11	-68.83	-5.34
10	10	0.41	0.42	0.50	0.47	0.53	0.36	0.48
11	0	242.75	242.74	242.69	242.90	242.40	258.24	242.66
11	1	-40.48	-40.23	-37.72	-39.08	-36.74	-43.26	-38.38
11	2	8.22	7.34	-1.96	1.97	-4.04	16.52	0.74
11	3	-80.49	-80.95	-85.80	-83.51	-87.22	-159.02	-84.45
11	4	21.95	24.80	54.65	41.24	62.49	3.14	46.18
11	5	-33.65	-33.80	-36.96	-42.30	-27.99	-21.29	-34.42
11	6	-66.80	-54.00	136.70	304.37	-180.25	-561.41	21.09
11	7	-15.91	-15.61	-11.22	-7.49	-18.32	-27.34	-13.85
11	8	20.70	19.46	6.31	11.83	3.42	28.35	10.14
11	9	40.02	34.69	-21.30	3.79	-35.89	71.23	-5.39
11	10	0.83	0.81	0.69	0.74	0.66	0.90	0.72
11	11	-0.05	-0.05	-0.05	-0.05	-0.05	-0.05	-0.05
12	0	-345.41	-345.40	-345.30	-345.55	-344.98	-369.68	-345.28
12	1	8.10	8.06	7.70	7.97	7.46	8.49	7.78
12	2	-6.58	-5.66	4.03	-0.08	6.22	-15.96	1.22
12	3	-297.42	-270.83	8.11	-116.95	80.95	-421.98	-71.12
12	4	50.77	48.63	26.16	36.17	20.38	64.95	32.56
12	5	-30.27	-29.85	-22.94	-14.86	-37.32	-51.53	-27.61
12	6	54.49	49.13	-30.73	-100.89	101.91	261.52	17.66
12	7	-10.75	-10.95	-13.80	-16.02	-9.48	-3.67	-12.14
12	8	-0.16	0.91	12.20	7.48	14.66	-6.73	8.91
12	9	-54.04	-48.33	11.66	-15.22	27.29	-88.01	-5.39
12	10	1.00	1.01	1.12	1.07	1.15	0.93	1.09
12	11	-0.01	-0.01	-0.01	-0.01	-0.01	-0.01	-0.01
12	12	0.00	0.00	0.00	0.00	0.00	0.00	0.00
13	0	203.02	203.01	202.94	203.11	202.72	216.74	202.93
13	1	14.11	14.02	13.01	13.41	12.81	15.22	13.30
13	2	4.91	4.35	-1.62	0.89	-2.94	10.27	0.12
13	3	256.65	219.55	-169.58	4.83	-271.12	468.98	-59.04
13	4	18.17	19.07	28.53	24.26	31.04	11.95	25.85
13	5	-19.23	-19.68	-26.80	-34.69	-12.61	2.09	-22.09
13	6	13.65	13.70	14.40	14.94	13.35	11.97	13.99
13	7	-11.43	-11.34	-10.08	-9.51	-11.40	-13.92	-10.71
13	8	15.02	14.19	5.40	9.07	3.49	20.12	7.96
13	9	41.99	36.51	-20.88	4.84	-35.84	74.98	-4.57
13	10	1.32	1.31	1.21	1.26	1.19	1.41	1.24
13	11	-0.09	-0.09	-0.09	-0.09	-0.09	-0.09	-0.09
13	12	0.00	0.00	0.00	0.00	0.00	0.00	0.00
13	13	-0.02	-0.02	-0.02	-0.02	-0.02	-0.02	-0.02

14	0	5.92	5.92	5.93	5.83	6.09	5.54	5.96
14	1	-16.67	-16.56	-15.44	-15.93	-15.17	-17.86	-15.76
14	2	-1.85	-1.72	-0.31	-0.80	-0.14	-2.57	-0.74
14	3	-329.58	-296.50	50.47	-105.04	141.00	-519.46	-48.09
14	4	19.70	19.75	20.27	20.10	20.30	19.85	20.10
14	5	-21.47	-21.14	-15.76	-9.58	-26.79	-38.00	-19.37
14	6	-4.66	-2.36	31.95	62.22	-25.23	-93.90	11.12
14	7	-9.00	-9.00	-8.80	-8.18	-9.78	-10.19	-9.03
14	8	2.28	2.84	8.74	6.30	9.99	-1.12	7.02
14	9	-45.44	-40.63	9.92	-12.73	23.10	-74.64	-4.44
14	10	1.17	1.17	1.23	1.20	1.24	1.10	1.21
14	11	-0.01	-0.01	-0.01	-0.01	-0.02	-0.01	-0.01
14	12	0.00	0.00	0.00	0.00	0.00	0.00	0.00
14	13	0.00	0.00	0.00	0.00	0.00	0.00	0.00
14	14	0.08	0.08	0.10	0.09	0.10	0.07	0.09
15	0	-98.48	-98.47	-98.41	-98.39	-98.47	-104.12	-98.44
15	1	8.54	8.50	8.01	8.21	7.91	9.07	8.15
15	2	-2.32	-2.14	-0.26	-1.19	0.37	-4.32	-0.77
15	3	144.23	122.68	-103.29	-2.01	-162.26	257.88	-39.10
15	4	19.19	18.74	14.04	16.03	12.99	21.64	15.41
15	5	-14.87	-15.07	-18.40	-22.61	-11.01	-3.85	-16.07
15	6	25.28	22.97	-11.54	-41.96	45.93	115.00	9.40
15	7	-7.42	-7.47	-8.42	-9.72	-6.17	-4.22	-7.74
15	8	8.82	8.48	4.87	6.34	4.14	10.86	5.93
15	9	29.31	25.42	-15.44	2.87	-26.10	52.73	-3.84
15	10	1.33	1.33	1.30	1.31	1.29	1.37	1.31
15	11	-0.09	-0.09	-0.09	-0.09	-0.09	-0.09	-0.09
15	12	0.00	0.00	0.00	0.00	0.00	0.00	0.00
15	13	-0.04	-0.04	-0.04	-0.04	-0.04	-0.04	-0.04
15	14	0.15	0.15	0.12	0.13	0.11	0.17	0.13
15	15	1.56	1.35	-0.93	0.09	-1.52	2.78	-0.28

Table E.3: MP2 short-range potential coefficients, v_{lmn}: R=8.5 au. Units: cm^{-1}

l	m	E0	A0	E1	A1	A2	stg	free
0	0	-33.272	-33.273	-33.282	-33.289	-33.270	-33.229	-33.277
1	0	1.839	1.841	1.865	1.869	1.850	1.766	1.855
1	1	0.583	0.591	0.678	0.635	0.706	0.553	0.654
2	0	-2.898	-2.898	-2.903	-2.916	-2.882	-2.830	-2.898
2	1	0.937	0.923	0.774	0.848	0.724	0.985	0.814
2	2	-1.046	-1.046	-1.041	-1.045	-1.037	-1.041	-1.042
3	0	0.597	0.599	0.613	0.618	0.601	0.539	0.606
3	1	0.022	0.030	0.108	0.063	0.142	0.023	0.088
3	2	-0.418	-0.422	-0.458	-0.438	-0.472	-0.416	-0.448
3	3	0.412	0.399	0.255	0.319	0.219	0.493	0.296
4	0	-2.364	-2.366	-2.392	-2.386	-2.390	-2.314	-2.383
4	1	0.141	0.142	0.163	0.164	0.153	0.085	0.155
4	2	-0.765	-0.764	-0.757	-0.766	-0.748	-0.743	-0.758
4	3	-0.466	-0.390	0.406	0.049	0.613	-0.891	0.180
4	4	-0.101	-0.098	-0.063	-0.064	-0.075	-0.141	-0.076
5	0	1.624	1.625	1.640	1.631	1.646	1.607	1.636
5	1	0.166	0.161	0.100	0.118	0.098	0.236	0.120
5	2	0.031	0.033	0.054	0.052	0.048	-0.017	0.046
5	3	0.819	0.735	-0.147	0.246	-0.375	1.298	0.104
5	4	0.002	-0.005	-0.083	-0.066	-0.078	0.064	-0.057
5	5	0.007	0.008	0.012	0.012	0.012	0.003	0.011
6	0	-0.875	-0.875	-0.879	-0.871	-0.890	-0.879	-0.880
6	1	-0.087	-0.084	-0.041	-0.053	-0.040	-0.137	-0.055
6	2	-0.094	-0.097	-0.130	-0.124	-0.127	-0.036	-0.119
6	3	-0.453	-0.398	0.185	-0.071	0.330	-0.791	0.018
6	4	-0.066	-0.061	-0.008	-0.020	-0.012	-0.104	-0.026
6	5	0.008	0.008	0.007	0.006	0.009	0.011	0.008
6	6	0.004	0.003	-0.010	-0.018	0.006	0.031	-0.003
7	0	0.188	0.188	0.184	0.177	0.197	0.212	0.188
7	1	0.036	0.034	0.018	0.021	0.020	0.052	0.024
7	2	-0.049	-0.046	-0.019	-0.023	-0.024	-0.100	-0.029
7	3	0.239	0.212	-0.067	0.051	-0.129	0.427	0.014
7	4	0.006	0.004	-0.018	-0.013	-0.018	0.009	-0.011
7	5	0.003	0.004	0.007	0.005	0.007	0.005	0.006
7	6	-0.012	-0.011	0.008	0.024	-0.022	-0.059	-0.003
7	7	0.002	0.002	0.003	0.003	0.003	0.001	0.003
8	0	0.006	0.006	0.013	0.019	0.002	-0.022	0.009
8	1	-0.018	-0.019	-0.022	-0.020	-0.024	-0.012	-0.021
8	2	0.011	0.009	-0.007	-0.006	-0.002	0.043	-0.001
8	3	-0.082	-0.071	0.040	-0.001	0.056	-0.190	0.006
8	4	0.005	0.005	0.001	0.002	0.002	0.031	0.003
8	5	-0.002	-0.002	0.000	0.001	-0.003	-0.011	-0.001
8	6	0.009	0.008	-0.012	-0.027	0.018	0.057	-0.001
8	7	0.002	0.002	0.002	0.002	0.002	0.003	0.002
8	8	-0.005	-0.005	-0.004	-0.004	-0.004	-0.007	-0.004
9	0	-0.028	-0.028	-0.034	-0.037	-0.028	-0.007	-0.031
9	1	-0.009	-0.008	0.006	0.001	0.007	-0.033	0.001
9	2	-0.028	-0.028	-0.022	-0.021	-0.026	-0.041	-0.024
9	3	0.043	0.039	-0.010	0.003	-0.009	0.122	0.006
9	4	-0.020	-0.019	-0.003	-0.006	-0.004	-0.063	-0.008
9	5	0.009	0.008	0.002	0.001	0.005	0.030	0.004
9	6	-0.009	-0.008	0.007	0.017	-0.014	-0.046	-0.001
9	7	0.001	0.001	0.002	0.002	0.002	0.000	0.001
9	8	0.000	0.000	-0.005	-0.004	-0.004	0.003	-0.003
9	9	0.002	0.002	0.003	0.003	0.004	0.001	0.003

10	0	-0.015	-0.014	-0.011	-0.011	-0.012	-0.026	-0.012
10	1	0.008	0.006	-0.007	-0.003	-0.007	0.031	-0.003
10	2	0.011	0.011	0.014	0.012	0.016	0.002	0.014
10	3	-0.021	-0.017	0.034	0.019	0.036	-0.094	0.017
10	4	0.025	0.023	0.001	0.006	0.003	0.073	0.008
10	5	-0.014	-0.013	-0.001	-0.001	-0.005	-0.046	-0.006
10	6	0.008	0.008	-0.003	-0.009	0.009	0.036	0.002
10	7	0.001	0.001	0.000	0.001	0.000	0.001	0.000
10	8	-0.005	-0.005	-0.001	-0.002	-0.002	-0.008	-0.002
10	9	-0.002	-0.002	0.003	0.001	0.005	-0.005	0.002
10	10	-0.001	-0.001	-0.001	-0.001	-0.001	-0.001	-0.001
11	0	0.009	0.008	0.007	0.009	0.005	0.011	0.007
11	1	-0.003	-0.003	0.005	0.003	0.005	-0.018	0.003
11	2	-0.004	-0.005	-0.012	-0.010	-0.012	0.013	-0.010
11	3	0.035	0.029	-0.031	-0.009	-0.039	0.106	-0.013
11	4	-0.026	-0.024	-0.005	-0.009	-0.007	-0.069	-0.011
11	5	0.019	0.018	0.002	0.003	0.007	0.059	0.008
11	6	-0.009	-0.008	0.001	0.003	-0.006	-0.032	-0.003
11	7	0.001	0.001	0.001	0.000	0.001	0.003	0.001
11	8	0.001	0.001	-0.002	-0.002	-0.002	0.003	-0.001
11	9	0.007	0.007	0.000	0.003	-0.002	0.011	0.002
11	10	-0.001	-0.001	-0.001	-0.001	-0.001	-0.001	-0.001
11	11	0.000	0.000	0.000	0.000	0.000	0.000	0.000
12	0	-0.001	-0.001	-0.001	-0.003	0.003	-0.002	0.000
12	1	-0.001	-0.001	-0.003	-0.002	-0.003	0.003	-0.002
12	2	0.004	0.004	0.011	0.009	0.011	-0.015	0.009
12	3	-0.023	-0.017	0.044	0.019	0.056	-0.083	0.026
12	4	0.022	0.020	0.007	0.010	0.009	0.050	0.012
12	5	-0.020	-0.019	-0.003	-0.004	-0.008	-0.061	-0.009
12	6	0.011	0.010	0.000	0.000	0.005	0.035	0.004
12	7	-0.001	-0.001	0.000	0.000	-0.001	-0.006	0.000
12	8	-0.002	-0.002	0.000	-0.001	-0.001	-0.004	-0.001
12	9	-0.005	-0.004	0.003	0.000	0.005	-0.009	0.001
12	10	-0.001	-0.001	-0.001	-0.001	-0.001	-0.001	-0.001
12	11	0.000	0.000	0.000	0.000	0.000	0.000	0.000
12	12	0.000	0.000	0.000	0.000	0.000	0.000	0.000
13	0	0.006	0.006	0.005	0.007	0.003	0.007	0.005
13	1	0.003	0.003	0.002	0.002	0.002	0.005	0.002
13	2	-0.003	-0.003	-0.008	-0.007	-0.008	0.009	-0.007
13	3	0.025	0.020	-0.036	-0.012	-0.049	0.080	-0.020
13	4	-0.017	-0.017	-0.010	-0.011	-0.011	-0.032	-0.012
13	5	0.021	0.020	0.006	0.006	0.010	0.055	0.011
13	6	-0.011	-0.010	0.000	0.000	-0.004	-0.037	-0.004
13	7	0.003	0.003	0.000	0.000	0.001	0.010	0.001
13	8	0.000	0.000	-0.001	-0.001	-0.001	0.001	-0.001
13	9	0.006	0.006	-0.001	0.002	-0.003	0.010	0.001
13	10	0.000	0.000	0.000	0.000	0.000	0.000	0.000
13	11	0.000	0.000	0.000	0.000	0.000	0.000	0.000
13	12	0.000	0.000	0.000	0.000	0.000	0.000	0.000
13	13	0.000	0.000	0.000	0.000	0.000	0.000	0.000

14	0	-0.002	-0.002	0.000	-0.001	0.000	-0.005	-0.001
14	1	-0.004	-0.004	-0.002	-0.002	-0.002	-0.008	-0.002
14	2	0.005	0.005	0.008	0.007	0.008	-0.001	0.007
14	3	-0.018	-0.013	0.038	0.016	0.050	-0.065	0.023
14	4	0.014	0.014	0.012	0.011	0.013	0.017	0.012
14	5	-0.018	-0.017	-0.006	-0.006	-0.010	-0.045	-0.011
14	6	0.009	0.008	-0.002	-0.001	0.001	0.035	0.002
14	7	-0.004	-0.003	0.000	0.000	-0.001	-0.013	-0.001
14	8	-0.001	-0.001	0.000	0.000	0.000	0.000	0.000
14	9	-0.004	-0.004	0.002	0.000	0.004	-0.007	0.001
14	10	-0.001	-0.001	-0.001	-0.001	-0.001	-0.001	-0.001
14	11	0.000	0.000	0.000	0.000	0.000	0.000	0.000
14	12	0.000	0.000	0.000	0.000	0.000	0.000	0.000
14	13	0.000	0.000	0.000	0.000	0.000	0.000	0.000
14	14	0.000	0.000	0.000	0.000	0.000	0.000	0.000
15	0	-0.008	-0.008	-0.009	-0.009	-0.009	-0.004	-0.009
15	1	0.003	0.003	0.002	0.002	0.002	0.005	0.002
15	2	-0.006	-0.006	-0.006	-0.006	-0.007	-0.004	-0.006
15	3	0.018	0.014	-0.028	-0.011	-0.037	0.060	-0.016
15	4	-0.011	-0.011	-0.011	-0.011	-0.012	-0.010	-0.011
15	5	0.017	0.016	0.009	0.008	0.012	0.035	0.012
15	6	-0.006	-0.005	0.003	0.002	0.001	-0.029	0.000
15	7	0.004	0.004	0.001	0.001	0.002	0.014	0.002
15	8	-0.001	-0.001	0.000	0.000	0.000	-0.002	-0.001
15	9	0.004	0.004	-0.001	0.001	-0.002	0.007	0.001
15	10	0.000	0.000	0.000	0.000	0.000	0.000	0.000
15	11	0.000	0.000	0.000	0.000	0.000	0.000	0.000
15	12	0.000	0.000	0.000	0.000	0.000	0.000	0.000
15	13	0.000	0.000	0.000	0.000	0.000	0.000	0.000
15	14	0.000	0.000	0.000	0.000	0.000	0.000	0.000
15	15	0.000	0.000	0.000	0.000	0.001	0.000	0.000

Table E.4: MP2 short-range potential coefficients, v_{lmn}: R=12 au. Units: cm^{-1}

l	m	E0	A0	E1	A1	A2	stg	free
0	0	-4.700	-4.700	-4.701	-4.700	-4.702	-4.700	-4.701
1	0	0.678	0.678	0.679	0.679	0.679	0.678	0.679
1	1	0.076	0.076	0.075	0.075	0.075	0.077	0.075
2	0	-0.488	-0.488	-0.488	-0.488	-0.488	-0.489	-0.488
2	1	-0.002	-0.002	-0.001	-0.002	-0.001	-0.003	-0.002
2	2	-0.067	-0.067	-0.071	-0.069	-0.073	-0.065	-0.070
3	0	-0.052	-0.052	-0.052	-0.052	-0.052	-0.052	-0.052
3	1	0.004	0.004	0.003	0.003	0.002	0.004	0.003
3	2	-0.041	-0.041	-0.039	-0.040	-0.039	-0.043	-0.040
3	3	-0.021	-0.016	0.038	0.014	0.052	-0.049	0.023
4	0	0.069	0.069	0.069	0.069	0.069	0.069	0.069
4	1	-0.003	-0.003	-0.003	-0.003	-0.003	-0.003	-0.003
4	2	-0.014	-0.014	-0.014	-0.014	-0.014	-0.014	-0.014
4	3	0.045	0.041	0.002	0.020	-0.008	0.065	0.013
4	4	-0.002	-0.002	-0.004	-0.003	-0.005	-0.002	-0.004
5	0	-0.013	-0.013	-0.013	-0.013	-0.013	-0.013	-0.013
5	1	-0.003	-0.003	-0.003	-0.003	-0.003	-0.003	-0.003
5	2	-0.003	-0.003	-0.004	-0.003	-0.004	-0.003	-0.003
5	3	-0.008	-0.007	0.009	0.002	0.014	-0.017	0.005
5	4	-0.003	-0.003	-0.002	-0.003	-0.002	-0.004	-0.003
5	5	0.000	0.000	0.000	0.000	0.001	0.000	0.000
6	0	0.001	0.001	0.001	0.001	0.001	0.001	0.001
6	1	0.000	0.000	0.000	0.000	0.000	0.000	0.000
6	2	-0.001	-0.001	-0.001	-0.001	-0.001	-0.001	-0.001
6	3	0.005	0.005	0.000	0.002	-0.002	0.008	0.001
6	4	0.000	0.000	-0.001	0.000	-0.001	-0.001	-0.001
6	5	0.000	0.000	0.000	0.000	0.000	0.000	0.000
6	6	0.000	0.000	0.000	0.001	0.000	-0.001	0.000
7	0	0.003	0.003	0.003	0.003	0.003	0.002	0.003
7	1	0.001	0.001	0.001	0.001	0.001	0.001	0.001
7	2	0.000	0.000	-0.001	0.000	-0.001	-0.001	0.000
7	3	-0.001	0.000	0.000	0.000	0.001	-0.001	0.000
7	4	-0.001	-0.001	0.000	0.000	0.000	0.000	0.000
7	5	0.000	0.000	0.000	0.000	0.000	0.000	0.000
7	6	0.000	0.000	0.000	0.000	0.000	0.000	0.000
7	7	0.000	0.000	0.000	0.000	0.000	0.000	0.000
8	0	0.001	0.001	0.001	0.001	0.001	0.001	0.001
8	1	0.000	0.000	0.000	0.000	0.000	0.000	0.000
8	2	-0.001	-0.001	-0.001	-0.001	-0.001	-0.001	-0.001
8	3	0.000	0.000	0.000	0.000	0.000	0.000	0.000
8	4	0.001	0.001	0.000	0.001	0.000	0.000	0.000
8	5	0.000	0.000	0.000	0.000	0.000	0.000	0.000
8	6	0.000	0.000	0.000	0.000	0.000	0.000	0.000
8	7	0.000	0.000	0.000	0.000	0.000	0.000	0.000
8	8	0.000	0.000	0.000	0.000	0.000	0.000	0.000
9	0	0.000	0.000	0.000	0.000	0.000	0.000	0.000
9	1	0.000	0.000	0.000	0.000	0.000	0.000	0.000
9	2	0.000	0.000	0.000	0.000	0.000	0.000	0.000
9	3	0.000	0.000	0.000	0.000	0.001	0.000	0.000
9	4	0.000	0.000	0.000	0.000	0.000	0.000	0.000
9	5	0.000	0.000	0.000	0.000	0.000	0.000	0.000
9	6	0.000	0.000	0.000	0.000	0.000	0.000	0.000
9	7	0.000	0.000	0.000	0.000	0.000	0.000	0.000
9	8	0.000	0.000	0.000	0.000	0.000	0.000	0.000
9	9	0.000	0.000	0.000	0.000	0.001	-0.001	0.000

10	0	0.000	0.000	0.000	0.000	0.000	0.000	0.000
10	1	0.000	0.000	0.000	0.000	0.000	0.000	0.000
10	2	0.000	0.000	0.000	0.000	0.000	0.000	0.000
10	3	0.001	0.001	0.000	0.001	0.000	0.001	0.000
10	4	0.001	0.001	0.000	0.001	0.000	0.000	0.000
10	5	0.000	0.000	0.000	0.000	0.000	0.000	0.000
10	6	0.000	0.000	0.000	0.000	0.000	0.000	0.000
10	7	0.000	0.000	0.000	0.000	0.000	0.000	0.000
10	8	0.000	0.000	0.000	0.000	0.000	0.000	0.000
10	9	0.000	0.000	0.000	0.000	0.000	0.001	0.000
10	10	0.000	0.000	0.000	0.000	0.000	0.000	0.000
11	0	0.000	0.000	0.000	0.000	0.000	0.000	0.000
11	1	0.000	0.000	0.000	0.000	0.000	0.000	0.000
11	2	0.000	0.000	0.000	0.000	0.000	0.000	0.000
11	3	0.000	0.000	0.000	0.000	0.001	0.000	0.000
11	4	0.000	0.000	0.000	0.000	0.000	0.000	0.000
11	5	0.000	0.000	0.000	0.000	0.000	0.000	0.000
11	6	0.000	0.000	0.000	0.000	0.000	0.000	0.000
11	7	0.000	0.000	0.000	0.000	0.000	0.000	0.000
11	8	0.000	0.000	0.000	0.000	0.000	0.000	0.000
11	9	0.000	0.000	0.000	0.000	0.000	0.000	0.000
11	10	0.000	0.000	0.000	0.000	0.000	0.000	0.000
11	11	0.000	0.000	0.000	0.000	0.000	0.000	0.000
12	0	0.000	0.000	0.000	0.000	0.000	0.000	0.000
12	1	0.000	0.000	0.000	0.000	0.000	0.000	0.000
12	2	0.000	0.000	0.000	0.000	0.000	0.000	0.000
12	3	0.001	0.001	0.000	0.000	0.000	0.001	0.000
12	4	0.000	0.000	0.000	0.000	0.000	0.000	0.000
12	5	0.000	0.000	0.000	0.000	0.000	0.000	0.000
12	6	0.000	0.000	0.000	0.000	0.000	0.000	0.000
12	7	0.000	0.000	0.000	0.000	0.000	0.000	0.000
12	8	0.000	0.000	0.000	0.000	0.000	0.000	0.000
12	9	0.000	0.000	0.000	0.000	0.000	0.000	0.000
12	10	0.000	0.000	0.000	0.000	0.000	0.000	0.000
12	11	0.000	0.000	0.000	0.000	0.000	0.000	0.000
12	12	0.000	0.000	0.000	0.000	0.000	0.000	0.000
13	0	0.000	0.000	0.000	0.000	0.000	0.000	0.000
13	1	0.000	0.000	0.000	0.000	0.000	0.000	0.000
13	2	0.000	0.000	0.000	0.000	0.000	0.000	0.000
13	3	0.000	0.000	0.000	0.000	0.000	-0.001	0.000
13	4	0.000	0.000	0.000	0.000	0.000	0.000	0.000
13	5	0.000	0.000	0.000	0.000	0.000	0.000	0.000
13	6	0.000	0.000	0.000	0.000	0.000	0.000	0.000
13	7	0.000	0.000	0.000	0.000	0.000	0.000	0.000
13	8	0.000	0.000	0.000	0.000	0.000	0.000	0.000
13	9	0.000	0.000	0.000	0.000	0.000	0.000	0.000
13	10	0.000	0.000	0.000	0.000	0.000	0.000	0.000
13	11	0.000	0.000	0.000	0.000	0.000	0.000	0.000
13	12	0.000	0.000	0.000	0.000	0.000	0.000	0.000
13	13	0.000	0.000	0.000	0.000	0.000	0.000	0.000

14	0	0.000	0.000	0.000	0.000	0.000	0.000	0.000
14	1	0.000	0.000	0.000	0.000	0.000	0.000	0.000
14	2	0.000	0.000	0.000	0.000	0.000	0.000	0.000
14	3	0.001	0.001	0.000	0.000	0.000	0.001	0.000
14	4	0.000	0.000	0.000	0.000	0.000	0.000	0.000
14	5	0.000	0.000	0.000	0.000	0.000	0.000	0.000
14	6	0.000	0.000	0.000	0.000	0.000	0.000	0.000
14	7	0.000	0.000	0.000	0.000	0.000	0.000	0.000
14	8	0.000	0.000	0.000	0.000	0.000	0.000	0.000
14	9	0.000	0.000	0.000	0.000	0.000	0.000	0.000
14	10	0.000	0.000	0.000	0.000	0.000	0.000	0.000
14	11	0.000	0.000	0.000	0.000	0.000	0.000	0.000
14	12	0.000	0.000	0.000	0.000	0.000	0.000	0.000
14	13	0.000	0.000	0.000	0.000	0.000	0.000	0.000
14	14	0.000	0.000	0.000	0.000	0.000	0.000	0.000
15	0	0.000	0.000	0.000	0.000	0.000	0.000	0.000
15	1	0.000	0.000	0.000	0.000	0.000	0.000	0.000
15	2	0.000	0.000	0.000	0.000	0.000	0.000	0.000
15	3	0.000	0.000	0.000	0.000	0.000	0.000	0.000
15	4	0.000	0.000	0.000	0.000	0.000	0.000	0.000
15	5	0.000	0.000	0.000	0.000	0.000	0.000	0.000
15	6	0.000	0.000	0.000	0.000	0.000	0.000	0.000
15	7	0.000	0.000	0.000	0.000	0.000	0.000	0.000
15	8	0.000	0.000	0.000	0.000	0.000	0.000	0.000
15	9	0.000	0.000	0.000	0.000	0.000	0.000	0.000
15	10	0.000	0.000	0.000	0.000	0.000	0.000	0.000
15	11	0.000	0.000	0.000	0.000	0.000	0.000	0.000
15	12	0.000	0.000	0.000	0.000	0.000	0.000	0.000
15	13	0.000	0.000	0.000	0.000	0.000	0.000	0.000
15	14	0.000	0.000	0.000	0.000	0.000	0.000	0.000
15	15	0.000	0.000	0.000	0.000	0.000	0.000	0.000